BSPE98973-10000-1

해양 내부파의 생성기작 및 전파특성 연구

(Study on internal wave generation and propagation in the ocean)

기본연구사업 (Lab창의과제)

한국해양과학기술원

제 출 문

한국해양과학기술원장 귀하

본 보고서를 “해양 내부파의 생성기작 및 전파특성 연구”과제의 최종보고서로 제출합니다.

2014. 4.

총괄연구책임자 : 박 재 훈

참여연구원: 강석구 박영규 전찬형
이희열 임형규 안혜림

보고서 초록

<table>
<tr><td>과제고유
번호</td><td colspan="2"></td><td>해당단계
연구기간</td><td>2013년 5월1일
~2014년 4월 30일</td><td>단계 구분</td><td>1단계/1단계</td></tr>
<tr><td rowspan="2">연구사업명</td><td>중사업명</td><td colspan="5"></td></tr>
<tr><td>세부사업명</td><td colspan="5"></td></tr>
<tr><td rowspan="2">연구과제명</td><td>대과제명</td><td colspan="5"></td></tr>
<tr><td>세부과제명</td><td colspan="5">해양 내부파의 생성기작 및 전파특성 연구</td></tr>
<tr><td rowspan="2">연구책임자</td><td rowspan="2">박재훈</td><td>해당단계
참여연구원수</td><td>총 : 7 명
내부: 3 명
외부: 4 명</td><td>해당단계
연구비</td><td>정부: 85,000천원
기업: 천원
계 : 85,000천원</td></tr>
<tr><td>총 연구기간
참여연구원수</td><td>총 : 7 명
내부: 3 명
외부: 4 명</td><td>총
연구비</td><td>정부: 85,000천원
기업: 천원
계 : 85,000천원</td></tr>
<tr><td>연구기관명
소속부서명</td><td colspan="2">한국해양과학기술원 해양순환기후연구부</td><td>참여기업명</td><td colspan="2"></td></tr>
<tr><td>국제공동연구</td><td></td><td></td><td></td><td></td><td></td></tr>
<tr><td>위탁연구</td><td></td><td></td><td></td><td></td><td></td></tr>
<tr><td colspan="4">요약(연구결과를 중심으로 개조식 500자 이내)</td><td>보고서
면수</td><td></td></tr>
<tr><td colspan="7">－PIES관측 자료를 이용한 남중국해 비선형 내부파 전파 특성 분석
: 자료동화된 수치모델 결과를 통해 겨울철에 쿠로시오 해류가 남중국해로 관입하는 현상이 존재함을 보임
: 쿠로시오가 관입하는 시기에 생성되어 전파된 비선형 내부파의 생성 에너지와 관입과의 관계는 뚜렷한 관계를 보이지는 않음
: 쿠로시오 관입에 의해 비선형 내부파의 전파는 쿠로시오 관입에 의해 많은 영향을 받으며 해석모델을 통해 예측한 비선형 내부파의 전파특성과 관측된 전파특성이 잘 일치함을 밝힘
: 이전에 관측된 비선형 내부파의 계절적 변동성의 원인이 쿠로시오의 관입에 의한 것이었음을 본 연구를 통해 보임
: 쿠로시오 관입에 의해 비선형 내부파의 전파는 쿠로시오 관입에 의해 많은 영향을 받음을 밝힘
: 남중국해에 존재하는 강한 비선형 내부조석파의 전파특성이 루손해협 및 남중국해 내부에 존재하는 중규모 해양 순환에 민감하게 반응함을 보여줌</td></tr>
<tr><td rowspan="2">색인어
(각 5개 이상)</td><td>한 글</td><td colspan="5">조석내부파, 비선형내부파, 쿠로시오, 내부파모델, 중규모순환</td></tr>
<tr><td>영 어</td><td colspan="5">Internal tide, nonlinear internal wave, Kuroshio, internal wave model, mesoscale circulation</td></tr>
</table>

요 약 문

남중국해와 북서태평양을 연결하는 루손해협을 가로질러 북쪽으로 흘러가는 쿠로시오 해류는 겨울철에 남중국해 내부로 관입하는 현상이 일반적으로 일어난다. 이러한 쿠로시오의 관입이 루손해협에서 발생하여 남중국해 내부로 전파되는 강한 비선형 내부조석파의 생성 및 전파특성에 어떠한 영향을 주는지에 대한 연구를 2010-2011년 겨울 동안 Pressure-recording Inverted Echo Sounder (PIES)를 이용하여 획득한 현장 관측 자료와 자료 동화된 해양 모델 자료, 그리고 내부파 생성, 전파 및 전이를 모의한 2차원 모델을 이용하여 수행하였다. 분석결과 남중국해 내부와 외부역의 성층 차이와 연직 유속시어(shear)는 전파하는 내부파의 진폭 변동에 약간의 역할만 하는 것으로 나타났다. 쿠로시오의 관입이 존재할 때 2시간 정도 빨라진 내부파의 관측점 도달 시간은 성층과 유속시어를 모두 고려하는 내부파의 제1모드 위상 속도를 이용한 레이트레이싱 모델을 통해 잘 모사 되었다. 이 레이트레이싱을 이용하여 2005-2006년 겨울에 관측된 약한 내부파의 원인을 분석한 결과 쿠로시오의 관입에 의한 내부파의 굴절이 관측점에 도달한 내부파 에너지의 약화에 기여했던 것으로 보였다. 본 연구는 남중국해에 존재하는 강한 비선형 내부조석파의 전파특성이 루손해협 및 남중국해 내부에 존재하는 중규모 해양 순환에 민감하게 반응함을 보여준다.

SUMMARY

During winter the Kuroshio tends to cross Luzon Strait, penetrating the northeastern South China Sea where it forms energetic mesoscale structures. Luzon Strait is also a site where westward-propagating large-amplitude internal waves are generated. We describe observations of these waves acquired in the deep basin of the South China Sea during the winter of 2010-2011, with the goal of assessing the influence of mesoscale variability on their properties. Combining tidal current simulations with an internal wave generation and evolution model, we obtain time series of deviations between our observations and the model simulations. These deviations are analyzed in terms of mesoscale variability based on the data-assimilated HYbrid Coordinate Ocean Model (HYCOM) simulations. We find that simplified models of nonlinear internal wave response to changes in horizontal stratification gradients and vertical shear provide at best weak simulations of amplitude modulation. In contrast to these results, deviations of internal wave arrival time, occurring up to 2 h early during Kuroshio inflows, are quite well simulated when derived from integration of the first internal mode phase speed along two-dimensional ray-traced paths using HYCOM simulations of velocity and density fields together with bathymetry. Refraction of the internal waves by Kuroshio intrusions can lead to substantial distortion of the paths, sufficient to provide a potential explanation for the apparent suppression of waves during previous winter measurements. Our results suggest that the internal wave field can be a sensitive indicator of mesoscale variability in Luzon Strait and the northeastern South China Sea.

KEYWORDS
국문: 조석내부파, 비선형내부파, 쿠로시오, 내부파모델, 중규모순환
영문: Internal tide, nonlinear internal wave, Kuroshio, internal wave model, mesoscale circulation

목 차

Contents

제 1 장 서론

해양의 내부파는 성층이 존재하는 모든 해역에서 발생하고 전파할 수 있는 소규모(small scale) 해양과정이다. 해양의 중·심층에서 많이 관측되는 내부파는 그 생성, 전파, 소멸 등 특성이 중규모(meso-scale) 해양과정의 영향을 받지만 동시에 해수 혼합(Ocean Mixing)을 일으켜 중규모 해양과정을 변하게 하는 상호작용을 한다. 전 지구 기후와 관련된 해양 컨베이어 벨트(Ocean Conveyer Belt)를 구성하는 자오면 순환(Meridional Overturning Circulation)에서 상·하층 간 열 교환을 활발하게 하는 내부파에 의한 해수 혼합이 매우 중요한 역할을 하는 것으로 제안되어 왔으나 내부파의 생성 및 전파 특성 등의 기작은 아직 규명되지 못한 부분이 많이 있다.

북서태평양 및 그 주변해는 강한 내부파가 다양한 형태로 존재하는 해역이다. 기존에 중요하게 여겨지지 않았던 내부파와 같은 소규모 해양과정에 대한 연구는 북서태평양과 그 주변해의 해양과정 변동을 이해하기 위한 기초연구로서 반드시 필요하다. 표면 조석과 해저 지형의 상호작용으로 발생하는 조석에 의한 내부파의 생성 에너지는 일정한 것으로 고려되어 왔으나 내부파가 생성될 때의 배경 성층 조건에 따라 생성되는 에너지의 변동이 큰 것으로 알려져 있다. 북서태평양 및 그 주변해의 내부파는 쿠로시오의 변동이 큰 곳에서 활발하게 생성된다. 그러나 쿠로시오의 변동에 따른 내부파의 생성 특성에 관한 연구는 미미했으며 최근에 많은 관심을 받는 연구 주제이다.

내부파는 해양 혼합층 및 수온약층의 깊이를 단기간 내에 변화시켜 조건에 따라서는 해양 생태계의 일차 생산력의 변화에도 많은 영향을 준다. 그러므로 본 연구는 북태평양 및 그 주변해의 해양 생태계 연구에 활용될 수 있는 소규모 물리 과정에 대한 이해를 넓힐 수 있는 연구라고 할 수 있다.

내부파는 수중 음향 전파 특성에 큰 영향을 주는 해양 현상으로 미국 해군연구국 (Office of Naval Research)에서는 이 분야에 대한 연구 투자를

지속적으로 해오고 있다. 내부파의 생성 및 변동 특성을 규명하고자 하는 내부파에 대한 연구는 수중 음향을 이용한 수중 정보통신 기술 개발 및 산업화 과정에 필요한 해양 물리학적 기초 자료를 제공 할 수 있을 것이다. 또한 내부파는 수중 음향 전달에 아주 중요한 영향을 주기 때문에 내부파 영향을 예측하는 기술은 국방과학기술적 측면에서 꼭 필요한 기술이라고 할 수 있다. 따라서 내부파 연구의 결과들은 수중 음향의 전파에 대한 중요한 기초 자료로서 활용될 수도 있다.

제 2 장 국내외 기술개발 현황

북서태평양과 남중국해를 연결하는 해협인 루손해협(Luzon Strait)은 조석에 의한 내부파 발생이 지구상에서 가장 강한 곳 중에 한 곳으로 알려져 있다(e. g., Ramp et al. 2004; Ramp et al., 2010). 남중국해 해역으로 전파된 내부파는 조건에 따라서는 강한 비선형 내부파로 발전하여 수온약층을 수직적으로 200미터 이상 움직인다. 이러한 해양학적으로 특별한 현상으로 인해 미국 및 대만의 해양학자들이 미국 해군연구국의 지원으로 2000년대 초반부터 이 해역의 내부파 연구를 수행해 오고 있다.

최근 미국 해군연구국의의 지원으로 Internal Waves In Straits Experiment (IWISE, 연구기간: 2008~2013)라는 대형 연구사업이 진행 중임. 이 연구 사업에서 국제 공동 현장 관측과 수치모형 실험을 이용한 루손해협의 내부파 발생 및 남중국해에서의 내부파 전파 특성에 관한 연구가 집중적으로 수행되고 있음. 이 사업과 관련하여 본 연구총괄책임자가 공동연구책임자 자격으로 2010~2011년 동안 시행된 예비 관측 실험에 참여하여 Pressure-recording Inverted Echo Sounder (PIES)를 이용한 현장 관측 자료를 획득하였으며(그림 1), 2011~2012년의 주 관측 실험 자료는 2012년 4월에 획득하였다(그림 2). 본 연구에서 주로 분석한 남중국해 및 루손해협 현장 관측 자료는 내부파의 생성 및 전파 특성 연구에 있어서 기존에 없던 매우 귀중한 자료이다.

서울대학교 해양연구소에서 운영하고 있는 동해안에 위치한 ESROB 정점부이 관측 자료를 이용한 관성 주기 내부파에 관한 연구가 진행되어 왔으나 정점부이가 너무 연안에 위치하여 관측된 내부파의 생성 기작 및 전파 특성에 관한 연구는 부족한 실정이다. 또한 한국과학기술원의 최우영 교수 연구팀에서 내부파의 전파 및 전이 특성에 관한 연구를 수행 하고 있으나 이론적인 수치모형 실험에 국한되어 있다. 동중국해 해역에서 수중 음향 전파 특성 변동에 관한 한미 공동 현장 관측 실험이 이뤄졌고 향후에도 지속

적인 실험이 계획되고 있다.

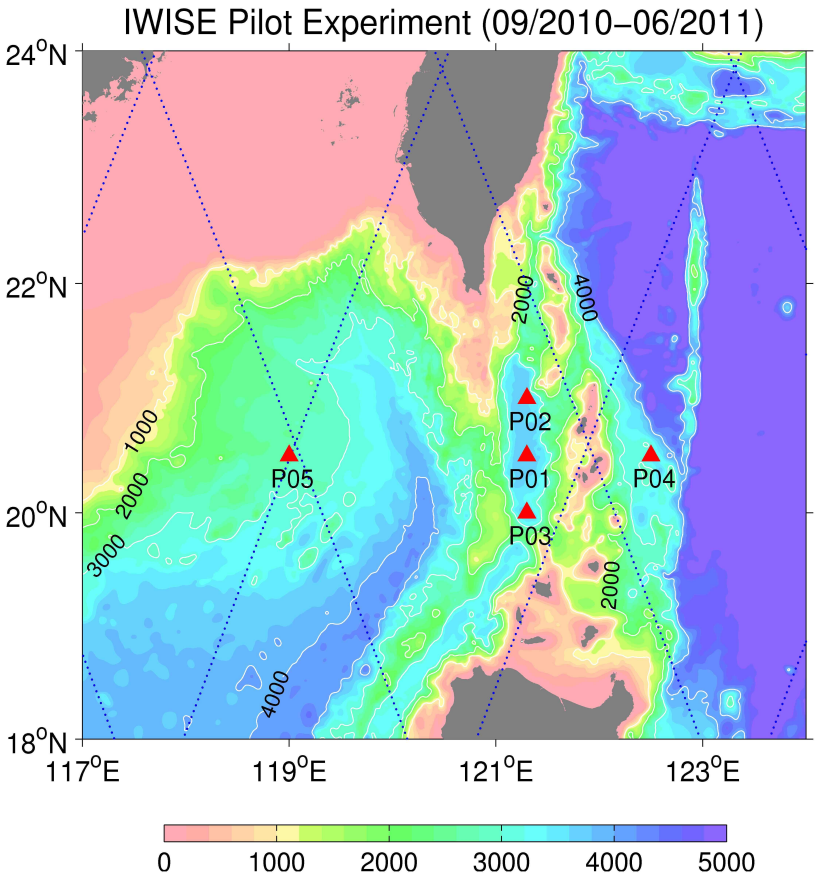

그림 1. IWISE 예비 관측 실험의 PIES 계류 정점 위치. PIES 5기를 2010년 9월부터 2011년 6월까지 투입하였음.

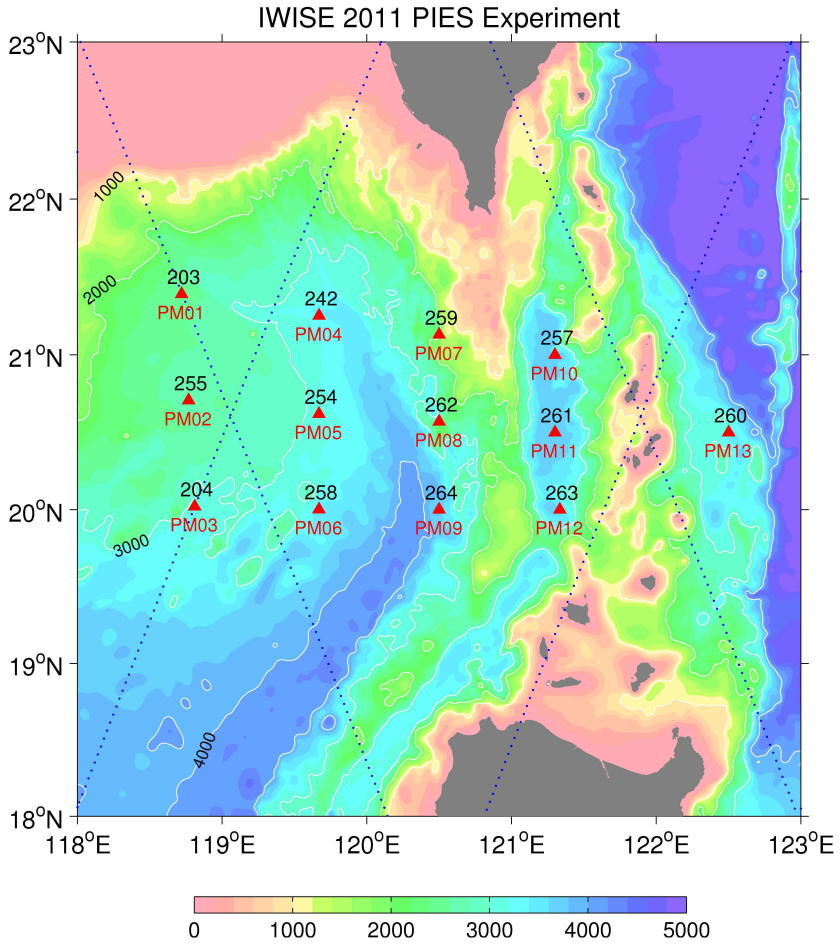

그림 2. IWISE 본 관측 실험의 PIES 계류 정점 위치. PIES 13기를 2011년 7월부터 2012년 4월까지 투입하였음.

제 3 장 연구개발 수행 내용 및 결과

3.1 관측

2010년 11월부터 2011년 4월까지 남중국해 북동해역에서 Pressure-recording Inverted Echo Sounder(PIES)를 이용하여 관측한 자료를 분석하였다. 관측 위치는 그림 3에서 나타내었다. 관측기간의 초반에는 쿠로시오가 남중국해로 관입하는 현상이 자료동화된 모델 결과를 통해서 확인되었다 (그림 3). PIES 정점 P05에서 관측된 결과를 보면 관측기간 동안 비선형 내부파가 계속해서 생성되어 전파되어 왔음을 확인 할 수 있다 (그림 4).

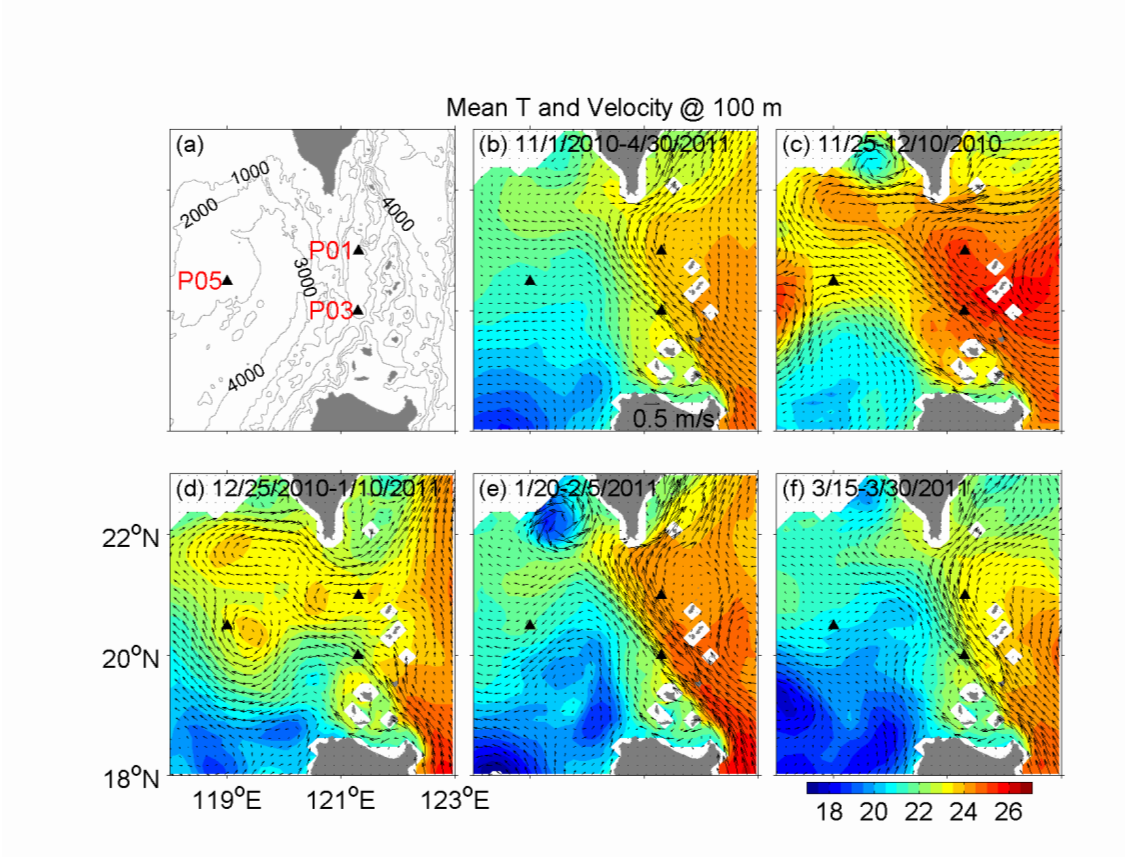

그림 3. (a) PIES 계류 위치. 자료동화된 HYCOM수치모델에서 재현한 (b) 관측기간 6개월 평균 100미터 수심 수온, 유속과 (c-f) 관측기간 중 15일 평균한 수온, 유속 분포.

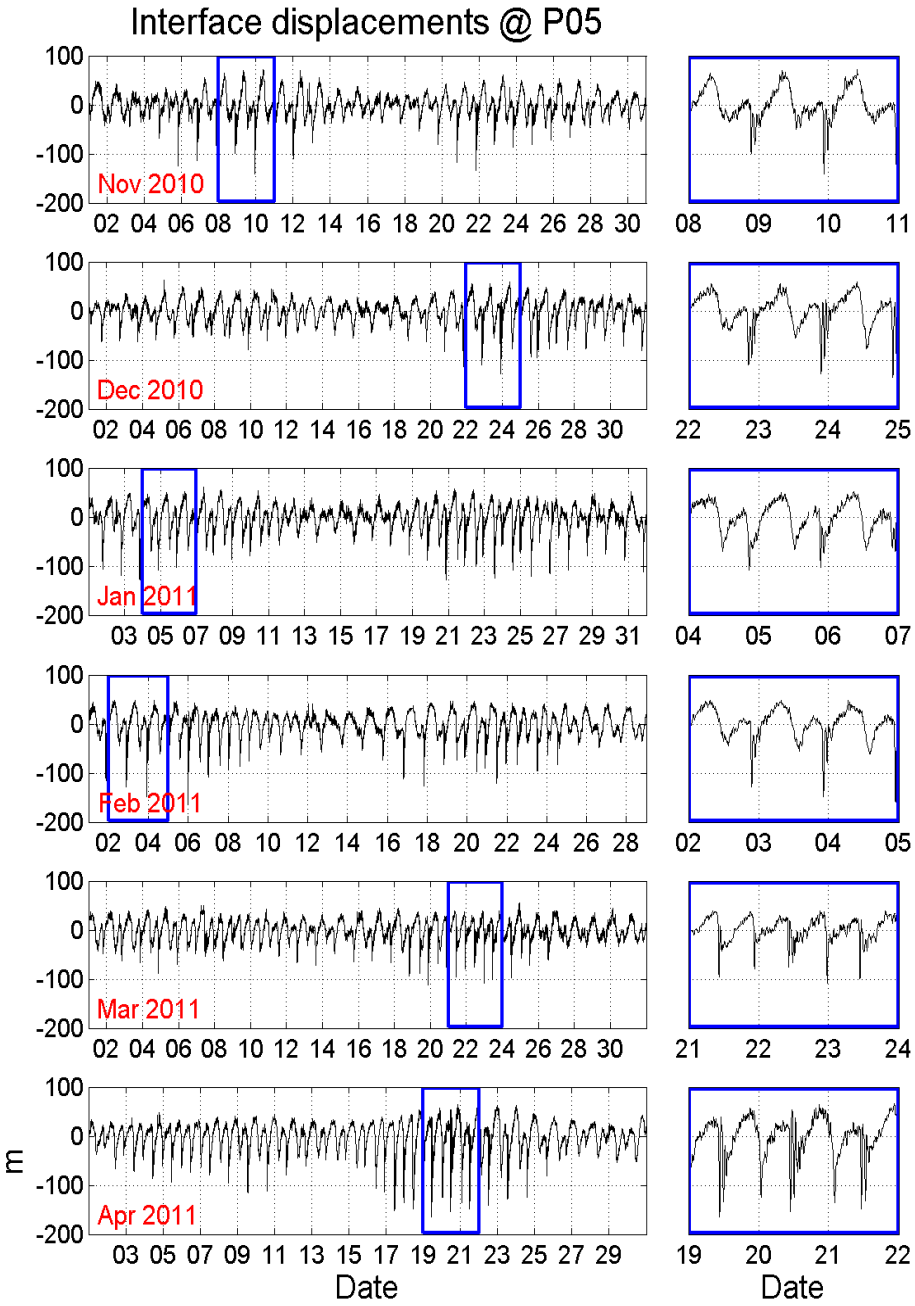

그림 4. PIES 정점 P05에서 관측한 비선형 내부파 시계열

3.2 수치모델과의 비교

P05에서 관측된 내부파와 비교하기 위하여 Li and Farmer (2011)에서 재안한 해석모델을 이용하였다. 그림 5는 해석모델에서 계산

한 결과와 관측결과의 비교를 보여준다. 전체적으로 해석모델이 관측한 내부파를 잘 재현하였으나 내부파의 크기와 내부파의 관측점 도달 시간의 차이가 시간에 따라 변화함을 알 수 있다. 이러한 현상은 쿠로시오의 변동과 밀접한 관련이 있는 것으로 사료된다.

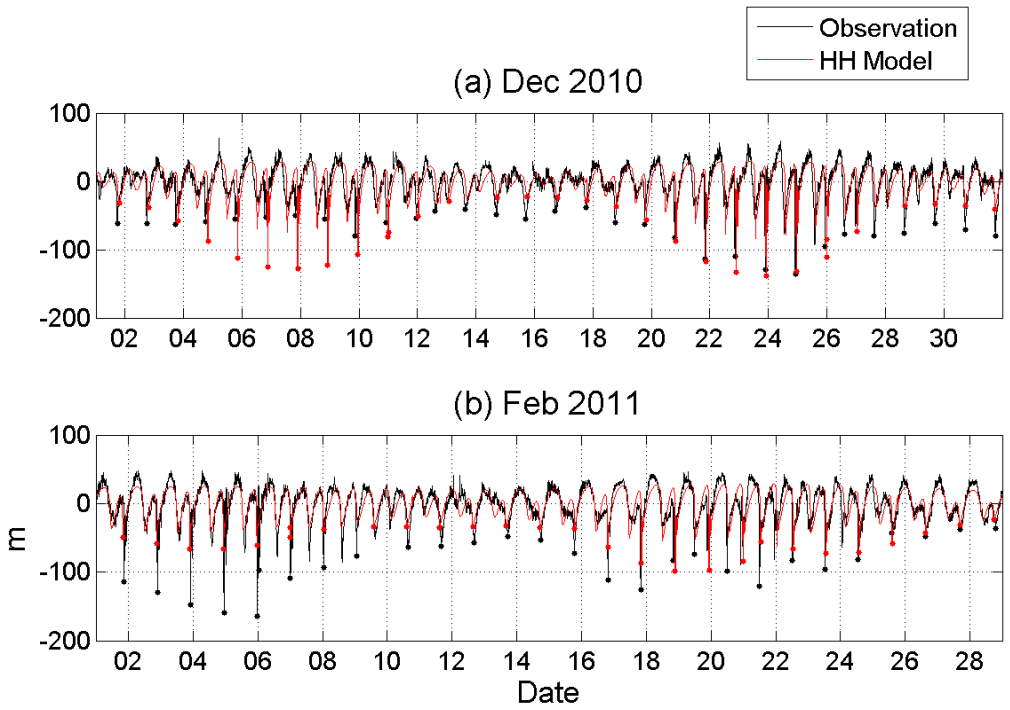

그림 5. 관측된 내부파와 해석모델로 계산한 내부파 비교 (검은색: 관측, 붉은색: 모델)

3.3 내부파 변동에 대한 쿠로시오의 영향

내부파의 전파에 대한 배경 유속의 영향을 확인하기 위하여 쿠로시오 관입이 활발하게 일어난 시기(2010년 12월 11-20일)와 그렇지 않았던 시기(2011년 1월30-2월8일)의 10일간의 유속평균과 성층을 이용하여 Raytracing 수치실험을 실시하였다. 그 결과 쿠로시오의 관입이 활발한 시기에 내부파의 전파속도가 빠르고 내부파가 남중국해에 넓게 퍼져나감을 확인하였다. 쿠로시오의 관입이 없었던 시기에는 내부파의 전파에 특별한 변화가 없이 초기조건과 크게 다르지 않은 전파 특성을 보였

다. 이 결과를 통해 내부파의 전파특성은 배경 유속과 배경 성층이 크게 영향을 미침을 확인 할 수 있었다.

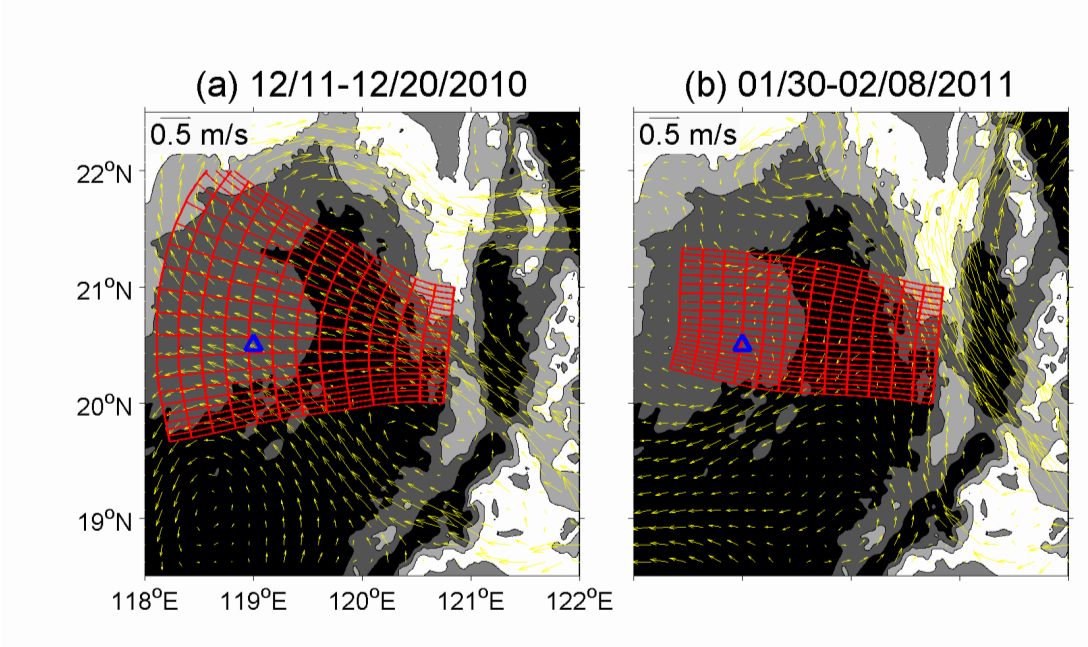

그림 6. 내부파 전파의 Raytracing 모델 결과. 노란색 화살표는 10일평균 유속을 보여줌.

내부파의 전파 속도와 그 크기가 시간적으로 어떻게 달라지는지 알아보기 위하여 관측한 결과와 해석모델로 예측한 결과의 차를 시계열로 표시하여 비교하였다 (그림 7). 관측 초기에는 해석모델이 예측한 내부파의 도달시간 보다 관측된 도달시간이 빠르며 시간이 지남에 따라 그 시간차가 역전되는 현상을 그림을 통해 알 수 있다. 이는 관측초기에는 쿠로시오의 관입이 활발히 일어나 내부파의 전파를 빠르게 했음을 의미하며 Raytracing 계산 결과와도 잘 일치한다.

내부파의 크기도 시간에 따라 변화하는데 관측초기에는 해석모델보다 작은 값이 관측되었으나 시간이 지남에 따라 해석모델의 예측보다 큰 값이 관측되었음을 알 수 있다. 이는 쿠로시오의 관입이 활발한 시기에 내부파의 크기도 작아짐을 보이는 결과 이지만 내부파의 도달시간에

미치는 쿠로시오의 영향에 비해서는 뚜렷하지 않은 것으로 보인다. 이것은 내부파의 에너지는 쿠로시오의 관입 이외에도 내부파 생성지역의 여러 환경 변화에 의한 영향이 큼을 시사한다.

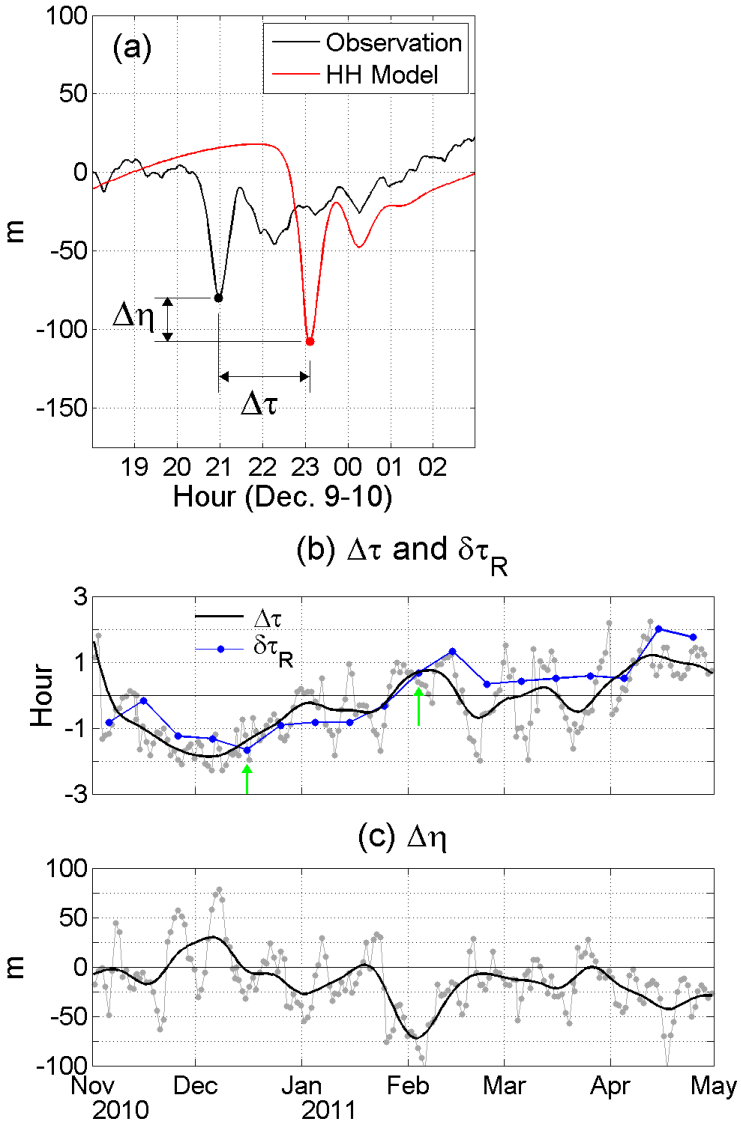

그림 7. (a) 관측과 모델결과의 시간차(Δτ)와 크기차(Δη)의 모식도. (b-c) Dt와 Dn의 시계열 (검은색, 20일 lowpass필터). 파란색 선과 점은 Raytracing의 통해 계산한 시간차($\delta\tau_R$)를 나타내며 녹색 화살표는 그림 6의 시기를 나타냄.

제 4 장 대형 과제제안서

<table>
<tr><td>과 제 명</td><td colspan="2">한반도 해역 해양혼합과 생지화학 물질 순환</td></tr>
<tr><td rowspan="2">사 업 분 류</td><td>분 야 별</td><td>성 격 별</td></tr>
<tr><td>미래자원( ), 환경보존( )
해양공간( ), 지구환경(●)
기타( )</td><td>기초(●), 응용( ), 개발( )</td></tr>
<tr><td rowspan="2">연 구 비</td><td>총 연 구 비(천원)</td><td>직 접 비(천원)</td></tr>
<tr><td>4,000,000</td><td>2,500,000</td></tr>
<tr><td>연 구 기 간</td><td colspan="2">3년</td></tr>
<tr><td>제안자</td><td colspan="2">해양순환기후연구부 책임연구원 박재훈</td></tr>
</table>

4.1 연구개발의 필요성

가. 기술적 측면

○ 해양의 내부파는 성층이 존재하는 모든 해역에서 발생하고 전파할 수 있는 소규모(small scale) 해양과정임. 발생한 내부파는 해양으로 전파되어 소규모의 해수 혼합과정 (ocean-mixing process)을 일으켜 해양 대순환, 열수송, 수중에 존재하는 영양염의 재분배 및 그에 따른 생물 활동의 변화까지 유발하는 것으로 알려져 있음 (그림 8).

○ 해양의 중·심층에서 많이 관측되는 내부파는 그 생성, 전파 및 소산 등의 특성이 중규모(mesoscale) 해양과정의 영향을 받지만 동시에 해수 혼합을 일으켜 중규모 해양과정을 변하게 하는 상호작용을 함.

○ 표면 조석과 해저 지형의 상호작용으로 발생하는 조석에 의한 내부파의 생성 에너지는 일정한 것으로 고려되어 왔으나 내부파가 생성될 때의 배경 성층 조건에 따라 생성되는 에너지의 변동이 큼.

○ 우리나라 주변 해역은 복잡한 해저지형과 강한 조석 및 바람에 의해 다양한 주기의 내부파가 생성, 전파 및 소산을 반복하고 있으며 겨울철 몬순기후, 쿠로시오 변동, 대마난류의 변동 및 와류변동 등에 의한 배경 성층의 변화가 크지만 내부파의 시공간적 변동성에 대한 이해는 아주 부족한 실정임.

○ 전 지구 기후와 관련된 해양 컨베이어 벨트(Ocean Conveyer Belt)를 구성하는 자오면 순환(Meridional overturning circulation)에서 상·하층 간 열 교환을 활발하게 하는 내부파에 의한 해수 혼합이 매우 중요한 역할을 하는 것으로 제안되어 왔음.

○ 그러나 내부파의 생성 및 전파 특성의 기작과 내부파의 소산에 의한 해수 혼합의 물리적 과정 등은 아직도 규명되지 못한 부분이 많이 있음.

○ 기후변화를 예측하는 기후모형에서 해양순환 변동성의 보다 정확한 예

측을 위해서는 해수 혼합 모수화의 개발이 필요하며 내부파 소산의 물리적 과정 규명을 통해 보다 진일보한 해수 혼합 모수화가 가능할 것으로 사료됨.

○ 내부파는 해양 혼합층 및 수온약층의 깊이를 단기간 내에 변화시켜 조건에 따라서는 해양 생태계의 1차 생산력의 변화에도 많은 영향을 줌. 어업이 활발한 우리나라 주변의 해역에서 1차 생산력의 변화는 2, 3차 생산력과 연관이 될 수 있음. 따라서 내부파에 대한 정확한 이해는 생태계 연구에 활용될 수 있는 기초연구로써 중요함.

○ 해양은 온실 가스의 하나인 이산화탄소를 흡수함으로써 기후 변화를 조절하고 있음. 해양에 흡수된 이산화탄소는 확산과 혼합을 통해 해저로 이동하는데 강한 연직 운동인 내부파 혹은 용승과 같은 물리적 과정을 통해 높은 이산화탄소의 수괴가 표층으로 노출된다고 알려져 있음. 이는 해양이 대기로부터의 이산화탄소 농도 흡수능을 떨어뜨리거나 오히려 해양이 흡수했던 이산화탄소가 대기로 방출될 가능성이 있음을 나타냄.

○ 우리나라 주변 해역에서는 계절에 따른 연안 해수표층의 이산화탄소 농도는 편차를 보이고 있으며 이는 용승 및 내부파에 의한 변화의 가능성이 있다고 사료됨. 따라서 해수의 이산화탄소 농도에 영향을 줄 수 있는 내부파의 생성 위치와 규모에 대한 정량적 평가가 필요한 실정임.

나. 경제, 산업적 측면

○ 내부파는 수중 음향 전파 특성에 큰 영향을 주는 해양 현상으로 미국 해군연구국 (Office of Naval Research)에서는 이 분야에 대한 연구 투자를 지속적으로 해오고 있음.

○ 내부파의 생성 및 변동 특성을 규명하고자하는 본 연구는 수중 음향 이용한 수중 정보통신 기술 개발 및 산업화 과정에 필요한 해양 물리학적 기초 자료를 제공 할 수 있음.

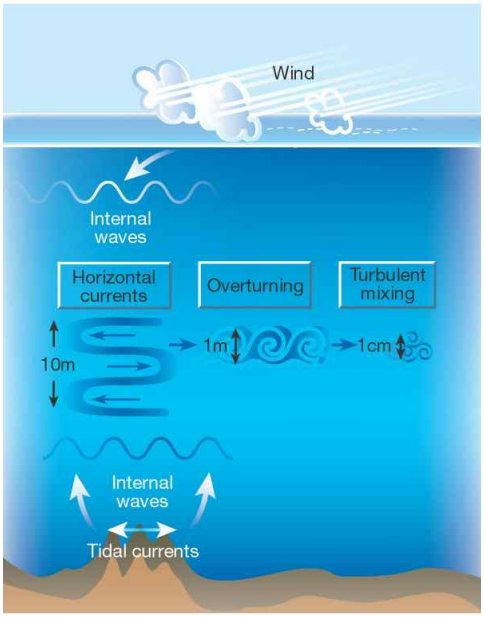

그림 8. 내부파 생성, 전파, 소산의 모식도 (Garrett, 2003, Nature).

○ 해양 내부파에 의한 해수 혼합 모수화 개발은 기후변화에 대응하기 위한 기초 기술로서 모형의 검증 및 성능 향상을 통해 기후변화에 대응하는 기술 수준을 높일 수 있음. 따라서 기후변화에 기인한 경제, 산업적 손실을 줄이고 한반도 기후의 장기 변화를 예측하기 위해서는 소규모의 내부파 소산 과정의 역학적 규명이 꼭 필요함.

○ 내부파 분포의 연구를 통해 온실 가스의 하나인 이산화탄소의 해양으로의 흡수능 평가에 필요한 해양 물리학적 기초 자료를 제공할 수 있음.

다. 사회, 문화적 측면

○ 내부파는 수중 음향 전달에 아주 중요한 영향을 주기 때문에 내부파 영향을 예측하는 기술은 국방과학기술적 측면에서 꼭 필요한 기술임. 본 연구에서 얻어질 결과는 수중 음향의 전파에 대한 중요한 기초 자료로서 활용될 수 있음.

○ 최근 들어 빈번히 발생하는 전지구적 기후변화에 기인한 자연재해 대한 적절하고 정확한 과학적 대응을 통해 사회적 불안감을 저감시키는데 기여할 것임.

4.2 국내·외 연구동향

가. 국외

○ 위성 이미지를 활용하여 전 지구적으로 내부파 분포를 보여주는 지도가 작성된 바 있음. An Atlas of Internal Solitary-like Waves and their Properties (2004) 우리나라 주변의 서해, 남중국해, 동해에서 생기는 내부파의 아주 일부분이 간략하게 소개되었음 (그림 9~11).

○ 우리나라의 대한해협과 동해와 같이 유사한 조석과 해저지형의 상호작용을 보이는 루손해협(Luzon Strait -북서태평양과 남중국해를 연결하는 해협)은 조석에 의한 내부파 발생이 강한 곳임.

○ 루손해협에서 발생하여 남중국해 방향으로 전파된 내부파는 조건에 따라서는 강한 비선형 내부파로 발전하여 수온약층을 수직적으로 200미터 이상 움직임. 이러한 해양학적으로 특별한 현상으로 인해 미국 및 대만의 해양학자들이 미국 해군연구국의 지원으로 2000년대 초반부터 이 해역의 내부파 연구를 수행하여 왔음.

○ 최근 미국 해군연구국의의 지원으로 Internal Waves In Straits Experiment (IWISE, 연구기간: 2008~2013)라는 대형 연구사업이 진행 중임.

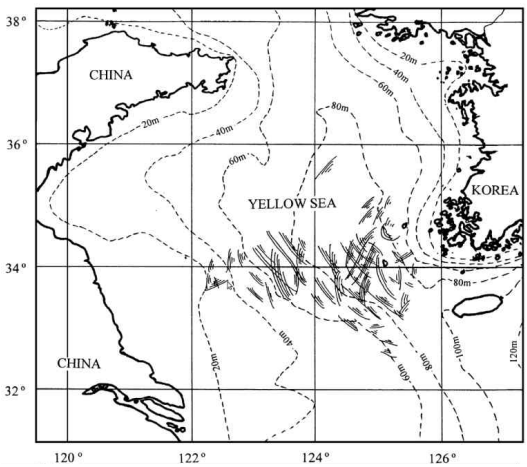

그림 9. 황해의 수심과 내부파의 분포.

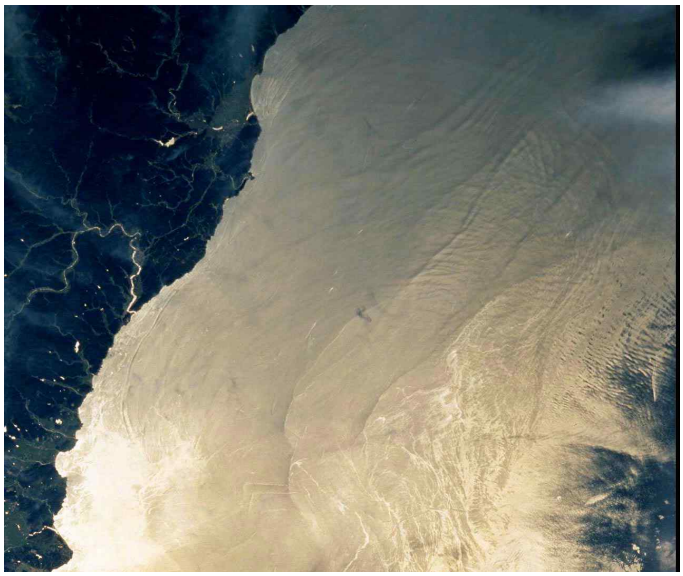

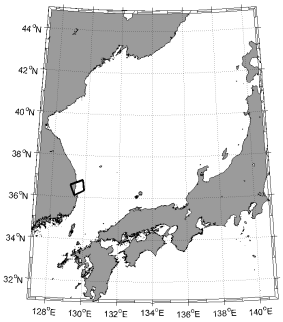

그림 10. 위성사진 (Astronaut photograph)을 통한 내부파 관측 (2000년 9월 20일).

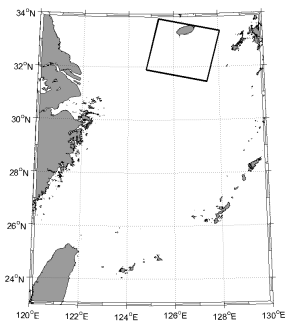

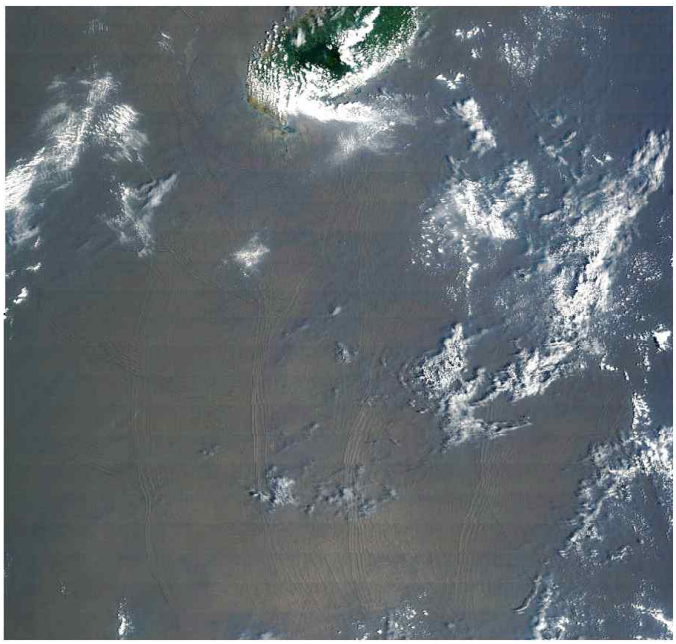

그림 11. MODIS 250-m 해상도의 시각 이미지(2003년 8월 3일). 서쪽으로 전파하는 파군(wave packet)이 관측됨.

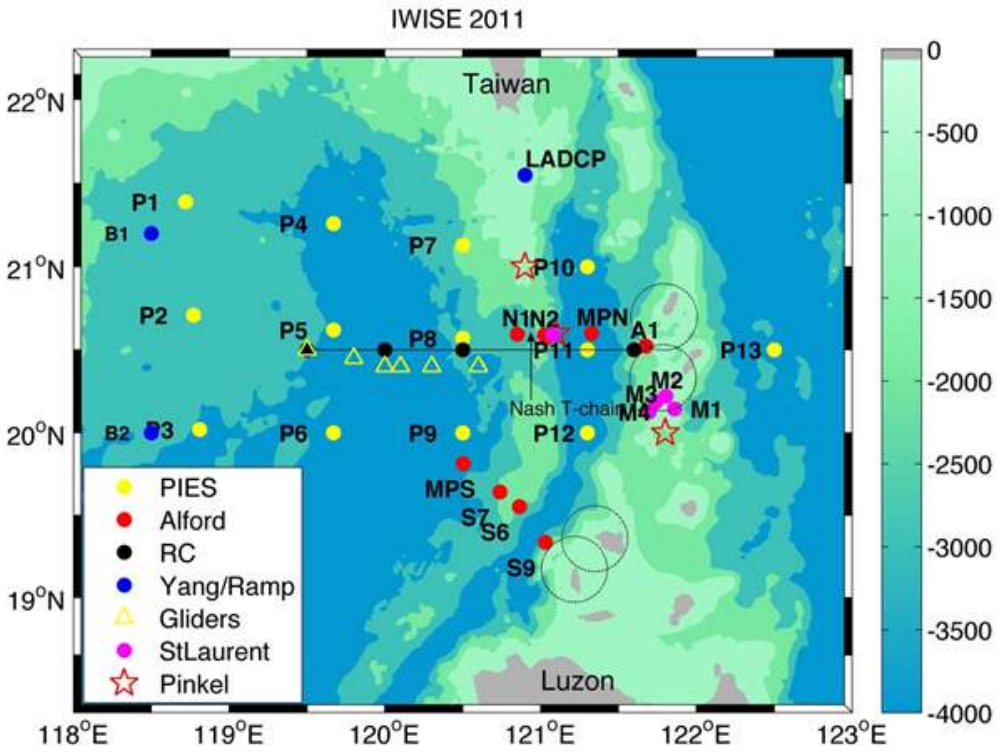

그림 12. 미국해군연구국 (Office of Naval Research)에서 지원하고 있는 Internal Waves in Straits Experiment (IWISE) 프로그램의 현장관측 정점도.

○ IWISE를 통해 국제 공동 현장 관측과 수치모형 실험을 이용한 루손해협의 내부파 발생 및 남중국해에서의 내부파 전파 특성에 관한 연구가 집중적으로 수행되고 있음. 이 사업과 관련하여 본 연구책임자가 공동연구책임자 자격으로 2010~2011년 동안 시행된 예비 관측 실험에 참여하여 Pressure-recording Inverted Echo Sounder (PIES)를 이용한 현장 관측 자료를 획득하였고 내부파의 생성 및 전파특성에 관한 연구를수행중에 있음 (그림 12).

나. 국내

○ 서울대학교 해양연구소에서 운영하고 있는 동해안에 위치한 ESROB 정점부이 관측 자료를 이용한 관성 주기 내부파에 관한 연구가 진행되어 왔으나 정점부이가 너무 연안에 위치하여 관측된 내부파의 생성 기작 및 전파 특성에 관한 연구는 부족한 실정임 (그림 13).

○ 한국과학기술원의 최우영 교수 연구팀에서 내부파의 전파 및 전이 특

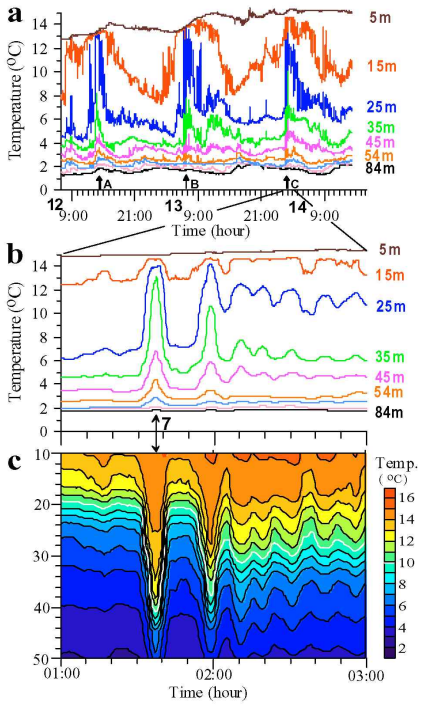

그림 13 (a) 동해 ESROB 관측을 통해 얻어진 수온의 시계열. 19시간 간격으로 강한 크기의 내부파가 관측됨. (b) a의 관측기간 중 2시간 동안의 시계열 자료에서 나타나는 변동. (c) 수온의 연직분포 변화.

성에 관한 연구를 수행 하고 있으나 이론적인 수치모형 실험에 국한되어 있음.

○ 동중국해 해역에서 수중 음향 전파 특성 변동에 관한 한미 공동 현장 관측 실험이 이뤄졌고 향후에도 지속적인 실험이 계획되고 있음.

○ CO2 해양지중저장 후보지 조사에 관한 연구 수행의 일환으로 저장 후보지의 물리적 특성에 대한 이해를 위한 조사과정중 대한해협 북쪽 끝자락의 대륙사면에서 조석에 의한 수온약층의 약 70m (대조기)의 강한 수직 변동이 관측되었음.

○ 조석을 포함한 해양 수치모델을 이용한 동해의 내부조석에 관한 연구는 동해에서 반일주조 내부파가 계절변동성이 강하다고 함. 이는 우리나라 주변 해역에서 내부파에 의한 해양의 물질순환이 계절별로 달라질 수 있음을 시사하고 있음.

4.3 연구 최종 목표

우리나라 주변의 해역에서 발생하는 내부파의 생성, 전파 및 소산의 변동성을 이해하여 해양혼합과정과 생지화학적 물질 순환의 변동 과정 규명

4.4 연구 개발 목표

가. 정성적 연구개발 목표

○ 우리나라 주변 해역의 내부파 아틀라스 작성

○ 해양 내부파가 혼합층, 수온 약층, 심층에서 연직 shear 및 난류를 통한 해양 혼합에 미치는 영향 평가

○ 아틀라스를 통한 내부파의 생성지역에서 생기는 생지화학적 변화 연구
- 내부 조석파에 의한 생지화학적 해저물질순환에 미치는 영향 (다학제간 연구)

○ 해양 혼합과 생태계 변동의 연관성 규명
- 조석이 해양생물 생체리듬에 미치는 영향 평가

○ 관측 결과를 활용한 조석이 포함된 해수순환 모형의 검증 및 최적 해양혼합 모수화를 위한 paramater 값 산정

○ 산정한 해수혼합 parameter를 활용한 기후모형 성능 평가

나. 정량적 연구성과 목표

구 분	계 획					
논문	국외			국내		
	SCI	기타	소계	SCI	기타	소계
	15 (5/년)				15 (5/년)	
Proceeding	국외			국내		
	15(5/년)			15(5/년)		

4.5 연구 개발 내용

연구 목표	내용 및 범위
해양 내부파 데이터베이스(DB) 구축	•현재까지 우리나라 주변 해역에서 관측한 데이터 수집 •수집한 데이터에서 내부파 연구에 활용 가능한 자료 선별 및 DB 구축 •기존 관측기기를 활용한 지속가능한 내부파 연구 활용 가능성 검토 및 원내외 간 공동 연구 협의
내부파 아틀라스 작성	•구축한 DB에 기반한 우리나라 주변 해역의 내부파 생성위치 및 규모 정량화 •내부파 아틀라스 작성 •1차년에 작성한 내부파 아틀라스의 갱신 (3차년) (내부파의 계절변동 등의 시공간적 변동성 연구)
내부파의 계절변동성 연구	•실해역 승선조사를 통한 내부파 계절변동성 연구 (연 4회, 총 2년간 8회) - CTD, LADCP, Aquadopp, Vectormeter 등 고해상도 유속계를 이용한 전 수층 및 해저경계층에서 일어나는 물리적 역학과정 변화조사 - Pressure-recording inverted echo sounder (PIES) 계류를 통한 장기간의 내부파 연구 - TurboMap, VMP를 이용한 난류 측정 : 해양 혼합의 정량적 평가 - pCO2 측정을 통한 해양 용존 이산화탄소 측정 •위성자료와 현장 관측을 통한 내부파와 해양표층의 1차 해양생태계 상관성 연구 •Ocean General Circulation Model (OGCM)을 활용한 내부파 특성 연구 •Non-hydrostatic numerical model (MIT-GCM, SUNTANS)을 이용한 내부파 생성기작 연구
내부파와 생지화학적 해저물질순환 연구	•현장 조사시 Lander를 활용한 생지화학적 해저물질순환 연구
해수혼합 모수화	•현장 관측 자료를 활용한 해수 혼합 parameter 모수화

4.6 연구 추진 전략 및 방법

(1) 추진 전략

연구 내용	1차년				2차년				3차년			
	1/4	2/4	3/4	4/4	1/4	2/4	3/4	4/4	1/4	2/4	3/4	4/4
우리나라 주변해의 내부파 생성지역 아틀라스 작성 연구												
- 기존 관측 기기 및 현장 조사를 통해 얻은 자료수집	■	■										
- 기존 관측 자료를 활용한 내부파 연구 활용가능성 검토 및 DB 구축	■	■	■									
- DB에 기반한 우리나라 주변해의 내부파 아틀라스 작성			■	■	■							
현장 관측을 통한 내부파 및 그 영향에 대한 평가												
- 현장 승선 사전 준비 및 조사 (2년간 계절별 1회씩 총8회 관측)			■	■	■	■	■	■	■	■	■	
- 현장 승선 조사 자료와 동 기간의 위성 자료를 이용한 내부파의 시공간적 계절별 변동 특성 연구				■	■	■	■	■	■	■	■	
- 내부파가 계절별로 해양 혼합 (난류) 에 미치는 영향에 대한 정량적 평가				■	■	■	■					
- 내부파에 의한 해저에서 나타나는 계절별 생지화학적 반응 변화 연구				■	■	■	■	■	■	■	■	
- 해양모형에 필요한 파라미터 산정				■	■	■	■					
수치 모델링을 이용한 내부파의 계절 변동성 연구												
- 산정한 파라미터를 이용한 해양모형 개발 및 개선			■	■				■	■			
- 수치모델을 이용한 내부파의 계절변동성 연구					■	■	■	■	■	■	■	
- 비정압 모델을 이용한 내부파 기작에 관한 연구								■	■	■	■	
종합보고서 작성												■
소요 연구비 (천만원)	25	25	25	25	30	40	40	40	30	40	40	40

(2) 연구 방법

가. 우리나라 주변 해역의 관측 자료 활용
- 국내외 자료 검토
- 내부파 연구에 활용 가능한 데이터 및 관측 기기의 지속적인 이용 가능성 검토

나. 현장 조사 사전 준비 및 관측 장비 구입
- PIES 6기 (5천만원 x 6 = 3억원)를 순차적으로 구입.

다. 현장 승선 조사를 통한 계절별 연구 (내부파 및 내부파에 의한 영향)
- 8회 (4회/연 * 2년)의 현장 조사, 1회시 15일간 관측, 계절별, 대/소조기별 내부파 특성 파악
- CTD, LADCP, PIES, XBT를 이용한 광범위한 전 수층의 물리적 특성 관측
- Aquadopp, Vectormeter 등을 활용한 해저경계층에서의 유속 관측
- Lander를 이용한 해저경계면에서의 생지화학적 물질순환 측정
- TurboMap, SCAMP를 이용한 내부파의 계절변동에 따른 해양 혼합 변화의 정량적 추산
- pCO2 측정을 통한 이산화탄소 농도 변화의 시계열 자료 작성

라. 수치 모델을 이용한 내부파의 생성 기작 및 내부파에 의한 해양혼합 연구진행
- OGCM을 이용한 내부파의 특성 및 혼합 과정 연구
- 미국 MIT 대학에서 개발한 nonhydrostatic MIT-GCM 모델을 이용한 내부파의 생성 기작 연구
- 미국 스탠포드대학에서 개발한 nonhydrostatic SUNTANS모델을 이용한 내부파의 생성 기작 연구

마. 국외 연구진과 공동 연구
- 미국 로드아일랜드대학교 해양대학원과의 공동연구 수행
  (미국의 PIES 6기 + 구입할 6기를 활용한 관측시스템 구축)

사. 국내 연구진과 공동 연구

- 서울대학교 장경일 교수 연구팀과 ESROB을 이용한 내부파 공동 연구 협의
- 한국해양대학교 이호진 교수 연구팀과 조석을 포함한 해양수치모델링 시스템 구축 및 개발

4.7 기대성과

가. 기술적 측면

○ 내부파 아틀라스 제작을 통한 타 분야에서의 활용가능성 제시

○ 계류관측 및 정선 관측 자료 해석을 통한 해양혼합 역학 규명

○ 내부파에 의한 해저에서의 물질 순환 및 생태계의 영향 규명

○ 대/소조기별, 계절별, 지역별 내부파 특성의 차이를 규명함으로써 해양 혼합 모수화 자료 제시

○ 산정한 해수 혼합 parameter를 활용한 기후모형 개선

나. 경제·산업적 측면

○ 상시 해양 (내부파) 관측 시스템 구축 및 운용 가능성 제시

4.8 활용방안

○ 해양 모델에서 내부파에 의한 해수 혼합 및 순환의 모수화 개선을 통하여 단기 및 장기 예보의 정확성을 높일 수 있음.

○ 내부파에 의한 해수 혼합 및 물질순환의 정량적 평가는 일반 고해상도의 해양순환 모델 뿐 만 아니라 미래 기후 예측 모델의 정확도를 높이는 데에도 중요한 역할을 할 것이라 여겨짐. 현재의 기후 모형들은 내부파 등의 프로세스를 대부분 무시하고 있음. 내부파에 의한 정확한 해양 혼합 모수화는 예보뿐만 아니라 미래 기후 예측의 정확도를 급격

하게 향상 시킬 수 있을 것으로 기대함.

○ 내부파에 의한 해저에서의 생지화학적 물질순환 연구를 토대로 전지구적인 다학제간 연구로의 발전가능성이 높음.

○ 한반도 주변 해역은 무수히 많은 내부파들이 혼재하고 있으며 각 해역에 해저지형 및 해수특성에 따라 그 생성 및 전파특성이 다름을 규명함으로써 수중 음향 특성 연구 사업과 같은 국방과학기술과 관련된 대형과제와 연계 가능함.

○ PIES, CTD 등 장비와 해저 통신 및 위성 데이터 송수신 수단을 이용(리모트 센싱)하여 해양 실시간 모니터링의 적합성 및 검토에 활용될 수 있음.

제 5 장 참고문헌

An Atlas of Internal Solitary-like Waves and their Properties (2004) (http://www.internalwaveatlas.com/Atlas2_index.html)

Hsu M. -K., Liu A. K. and Liu C., (2000), A study of internal waves in the China Seas and Yellow Sea using SAR, Continental Shelf Research, 20, 389-410.

Garrett, C. (2003), Oceanography: Mixing with latitude, Nature 422, 477 (3 April 2003) | doi:10.1038/422477a.

Li, Q., and D. M. Farmer (2011), The generation and evolution of nonlinear internal waves in the deep basin of the South China Sea, J. Phys. Oceanogr., 41, 1345-1363.

Ramp, S. R., T.-Y. Tang, T. F. Duda, J. F. Lynch, A. K. Liu, C.-S. Chiu, F. L. Bahr, H.-R. Kim, and Y. J. Yang (2004), Internal solitons in the northeastern South China Sea. Part I : Sources and deep water propagation, IEEE J. Oceanic Eng., 29, 1157-1181.

Ramp, S. R., Y. J. Yang, and F. L. Bahr (2010), Characterizing the nonlinear internal wave climate in the northeastern South China Sea, Nonlinear Processes Geophys., 17, 481-498, doi:10.5194/npg-17-481-2010.

제 6 장 부록

○ 발간 논문 목록 및 원문

게제일	논문명	저자		학술지명	Vol. (No)	국내외 구분	SCI 구분
		주저자	공저자				
2012. 12	Near 13 day Barotropic Ocean Response to the Atmospheric Forcing in the North Pacific	나한나	박재훈 외 4명	Journal of Geophysical Research	117: C12019	국외	SCI
2012. 12	Tidal dynamics in the strong tidal current environment of the Uldolmok waterway, southwestern tip off the Korean peninsula	강석구	정경태 외 5명	Ocean Science Journal	47(4): 453-463	국내	SCIE
2013. 01	Stability of the Kuroshio path with respect to glacial sea level lowering	이경은	이호진 외 6명	Geophysical Research Letters	40(2): 392-396	국외	SCI
2013. 12	Effects of Kuroshio intrusions on nonlinear internal waves in the South China Sea during winter	박재훈	David Farmer	Journal of Geophysical Research	118(1): 7081-7094	국외	SCI

Near 13 day barotropic ocean response to the atmospheric forcing in the North Pacific

Hanna Na,[1] Jae-Hun Park,[2] D. Randolph Watts,[1] Kathleen A. Donohue,[1] and Ho Jin Lee[3]

Received 15 May 2012; revised 19 October 2012; accepted 21 October 2012; published 13 December 2012.

[1] In the Kuroshio Extension System Study (KESS) east of Japan, bottom pressure observations over the 2 year study period exhibit strong high-frequency variability near 13 days. The first cyclostationary empirical orthogonal function mode for the band-pass-filtered KESS bottom pressure explains about 57% of the near 13 day variance and exhibits almost in-phase variability in space with a hint of westward propagation. The 13 day variability is strong during the winter and is driven by the large-scale wind stress curl over a broad region of the North Pacific. Modeling results over the North Pacific closely follow the observations and indicate that topography confines the barotropic response to the west of Emperor Seamount Chain and slows the westward propagation of the near 13 day bottom pressure variability.

Citation: Na, H., J.-H. Park, D. R. Watts, K. A. Donohue, and H. J. Lee (2012), Near 13 day barotropic ocean response to the atmospheric forcing in the North Pacific, *J. Geophys. Res.*, *117*, C12019, doi:10.1029/2012JC008211.

1. Introduction

[2] High-frequency (periods shorter than about 60 days) bottom pressure variability has not been well understood, mainly due to the sparse distribution of observations in both space and time. During the North Pacific Barotropic Electromagnetic and Pressure Experiment (BEMPEX) [*Luther et al.*, 1987], the barotropic response observed by ocean bottom pressure recorders was shown to be related to the large-scale atmospheric forcing for time scales longer than about 10 days [*Luther et al.*, 1990; *Chave et al.*, 1991]. BEMPEX provided insight into bottom pressure variability using a well-sampled data set in time, but not in space.

[3] More recently, analysis of Gravity Recovery and Climate Experiment (GRACE) mission data has lead to an increasingly global view of bottom pressure variability. Yet, GRACE is limited in the time domain due to the monthly mapping interval, which restricts the Nyquist period to 60 days [*Condi and Wunsch*, 2004; *Park et al.*, 2008; *Quinn and Ponte*, 2011; *Quinn and Ponte*, 2012]. Furthermore, *Quinn and Ponte* [2011] have noted that high-frequency (<60 days) bottom pressure variability is underestimated in the Ocean Model for Circulation and Tides (OMCT) that has been used to de-alias the nontidal bottom pressure variability measured by GRACE, and underestimated as well in the data-constrained solutions produced by the Estimating the Circulation and Climate of the Ocean (ECCO) project. Better understanding of high-frequency bottom pressure variability is needed to reduce these aliasing errors.

[4] In the Kuroshio Extension System Study (KESS) east of Japan [*Donohue et al.*, 2008], 2 year long hourly records of bottom pressure were measured at 15 sites (Figure 1a). The barotropic signal exhibited strong high-frequency variability near 13 and 21 days contributing nearly two thirds of the deep subtidal pressure variance [*Donohue et al.*, 2010], however, previous studies have focused on the mesoscale circulation in the KESS region after removing a site-averaged pressure signal [*Jayne et al.*, 2009; *Tracey et al.*, 2012].

[5] Local wind stress curl variability has been reported as a major factor driving the bottom pressure variability at periods shorter than about 7–10 days, whereas remote large-scale wind stress curl can be important at some periods longer than about 7–10 days [*Willebrand et al.*, 1980; *Müller and Frankignoul*, 1981; *Luther et al.*, 1990]. The focus of this study, the near 13 day bottom pressure signals, might therefore arise from a combination of local and large-scale forcing. The objective of this study is to understand what drives the strong near 13 day bottom pressure variability in the Kuroshio Extension and in particular to distinguish between local and large-scale atmospheric forcing. Notably the 13 day period is close to that of the fortnightly lunar tide (Mf), however, the amplitude of Mf in the KESS region is about 4 mm [*Schwiderski*, 1982; *Egbert and Ray*, 2003], an order of magnitude smaller than the observed near 13 day variability.

[6] To interpret the contextual relationship of the KESS measurements, which are restricted within the western edge of the North Pacific (Figure 1a), to the broader regional ocean's response to atmospheric forcing, a basinwide (Figure 1b) barotropic model is employed which is shown to closely replicate the observations. The KESS data, atmospheric data,

[1]Graduate School of Oceanography, University of Rhode Island, Narragansett, Rhode Island, USA.
[2]Korea Institute of Ocean Science and Technology, Ansan, South Korea.
[3]College of Ocean Science and Technology, Korea Maritime University, Busan, South Korea.

Corresponding author: J.-H. Park, Korea Institute of Ocean Science and Technology, 1270 Sa-2-dong, Ansan, 426-744, South Korea. (jhpark@kordi.re.kr)

0148-0227/12/2012JC008211

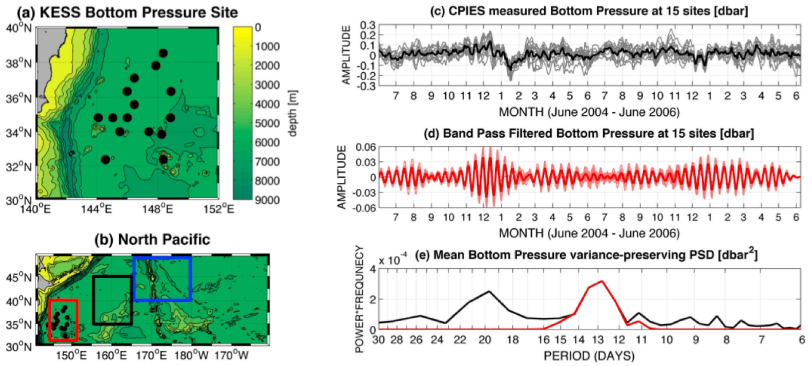

Figure 1. Geographic map of (a) the KESS sites used in this study and (b) the North Pacific, (c) time series of the KESS bottom pressure and (d) KESS band-pass-filtered bottom pressure, and (e) variance-preserving spectra of the KESS mean bottom pressure. Blue, black, and red boxes in Figure 1b represent the regions over the Emperor Seamount Chain (ESC), to the west of the Emperor Seamount Chain (W_ESC), and over the KESS measurements (KESS_box). Light lines in Figures 1c and 1d show time series of the each station, and bold lines in Figures 1c and 1d represent mean of the 15 sites. Black and red lines in Figure 1e are variance-preserving spectra of the mean time series in Figures 1c and 1d, respectively.

barotropic model and the analytical tools used in this study are described in section 2. The near 13 day bottom pressure variability in the KESS measurements is examined, and its relationship with the atmospheric variability in the North Pacific is investigated in sections 3 and 4. A comparison with the results from the barotropic model in the North Pacific and discussion and conclusions follow in sections 5 and 6.

2. Data and Methods

2.1. Data

[7] Fifteen sites within the KESS array spanned the 2 year period from 1 June 2004 to 8 June 2006 (Figure 1c). The 12 hourly detided KESS bottom pressure signal ranges ±0.3 dbar, which is equivalent to ±30 cm in height of the ocean water column, without considering variations in sea level (atmospheric) pressure. To focus upon the near 13 day signal, each time series is band-pass filtered with cut off periods of 11 and 15 days. A fourth-order Butterworth filter is run forward and backward to eliminate phase shifts. Figure 1d shows the band-pass-filtered data; all sites exhibit nearly in-phase fluctuations with highest amplitude (up to 0.06 dbar) in winter. After band-pass filtering, the near 13 day signal remains without a loss of energy (Figure 1e).

[8] The relationship between the near 13 day signal and large-scale atmospheric variability is investigated using wind and sea level pressure over the North Pacific (Figure 1b) from the ERA-Interim (European Centre for Medium-range Weather Forecasts Re-Analysis) data set [*Uppala et al.*, 2005] for the same period as the KESS bottom pressure data. These data are also band-pass filtered for the 11–15 day period. Figure 2 shows the 12 hourly wind stress curl and band-pass-filtered wind stress curl, averaged near the Emperor Seamount Chain (ESC, blue box in Figure 1b). The region near the ESC is where wind stress curl and KESS bottom pressure signal show the highest covariability near 13 day periods in section 4. It is interesting that the wind stress curl near the ESC shows a broad spectral peak near 13 day period (Figure 2c), considering the stochastic nature of atmospheric fluctuations (white noise at periods longer than synoptic time scales).

2.2. North Pacific Barotropic Model

[9] The ocean barotropic model used in this study is the ROMS (Regional Ocean Modeling System) version 3.1, which is a free-surface, terrain-following, primitive equations ocean model (http://www.myroms.org). We focus on the barotropic component of ROMS that solves the vertically integrated momentum equation neglecting density variations. The model bathymetry is setup with ETOPO5, which is a digital bathymetry data set with resolution 5 min (http://www.ngdc.noaa.gov/mgg/global/etopo5.html). The model area covers the region 100°E–70°W, 35°S–65°N with grid resolution of 1/2° in latitude and longitude. The eastern boundary of the model domain (close to the western coast of the Americas) is closed, while Flather boundary condition [*Flather*, 1976] is employed at the open boundaries (southern, northern and western) for barotropic normal velocity components. For the surface elevation, a gradient boundary condition is applied by setting the surface elevation at the open boundary to be equal to the closest interior value. Model results over the region and subregions of the North Pacific shown in Figure 1b are analyzed in this study.

[10] To calculate momentum at the sea surface, wind stress from ERA-Interim data with 1.5° resolution and 12 h intervals are used from January 2004 to December 2006; the

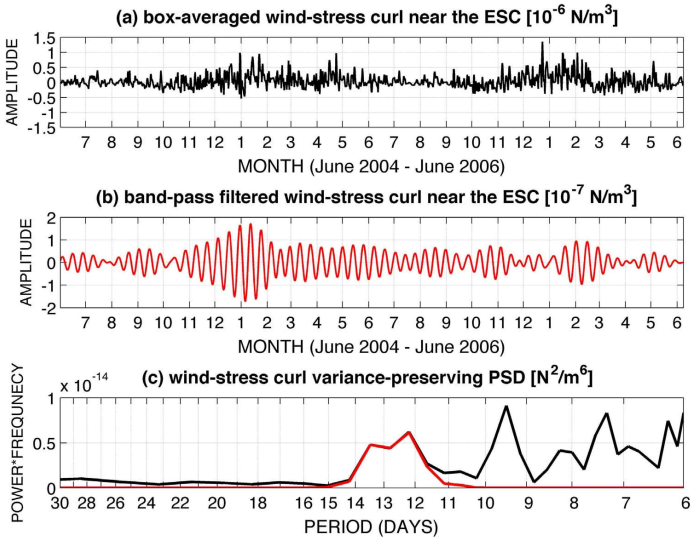

Figure 2. Time series of the (a) wind stress curl averaged over the Emperor Seamount Chain (ESC) (blue box in Figure 1b), (b) band-pass-filtered wind stress curl averaged over the ESC, and (c) variance preserving spectra of Figure 2a in black and 2b in red.

barotropic model does not require a long spin-up time because of a rapid adjustment to the wind stress forcing. Atmospheric forcing was only by wind stress; to have included atmospheric pressure forcing would have required a global model. The wind-only forced barotropic model (North Pacific Barotropic Model, NPBM hereafter) results agree well with the KESS observational data (Figure 3). The bold and light lines in Figure 3 are the time series of NPBM results averaged over the KESS_box (region defined by the red box in Figure 1b) and averaged bottom pressure of the KESS sites, respectively. Correlation coefficient between them is 0.71 for the 2 year period. After band-pass filtering, it decreases to 0.57. Nevertheless, the records match well during the winter when the near 13 day variability is relatively strong.

[11] Two additional experiments were performed with different conditions of bottom topography (Table 1). One experiment uses a 5000 m deep flat bottom over the entire model domain (NPBM_flat) and the other uses real topography, but with the ESC removed (NPBM_noESC). Other conditions, including the wind forcing, are unchanged from the real topography case. A comparison between the results from NPBM with real topography (NPBM_realtopo), NPBM_flat, and NPBM_noESC helps to distinguish the effect of bottom topography on bottom pressure variability.

2.3. Cyclostationary EOF Analysis

[12] Band-pass-filtered KESS bottom pressure data are analyzed using a cyclostationary empirical orthogonal function (CSEOF) technique [*Kim et al.*, 1996; *Kim and North*, 1997]. Space-time data, $P(r, t)$, are decomposed into cyclostationary loading vectors (CSLVs), $\mathrm{CSLV}_n(r, t)$, and their corresponding principal component (PC) time series, $\mathrm{PC}_n(t)$:

$$P(r,t) = \sum_n \mathrm{CSLV}_n(r,t)\mathrm{PC}_n(t), \tag{1}$$

where n, r, and t denote the mode number, space and time, respectively. CSLVs are orthogonal to each other and PC time series are mutually uncorrelated. Each CSLV represents a temporally evolving spatial pattern, and the corresponding PC time series shows the amplitude modulation of that pattern. The CSLVs are periodic with a nested period, d, which is set to be 13 days in this study:

$$\mathrm{CSLV}_n(r,t) = \mathrm{CSLV}_n(r,t+d). \tag{2}$$

The CSEOF technique is useful for extracting physically evolving spatial patterns. The physical evolution within the nested period, which is the near 13 day bottom pressure variability in this study, is captured in the resulting spatial patterns (CSLV_n). The long-term evolution of the physical process is reflected in the corresponding PC time series (PC_n).

[13] A multiple regression analysis is applied to understand the relationship between KESS bottom pressure (a target variable) and wind stress curl or sea level pressure (a predictor variable). After a predictor variable is also decomposed into CSLVs of the same 13 day nested period, its PC

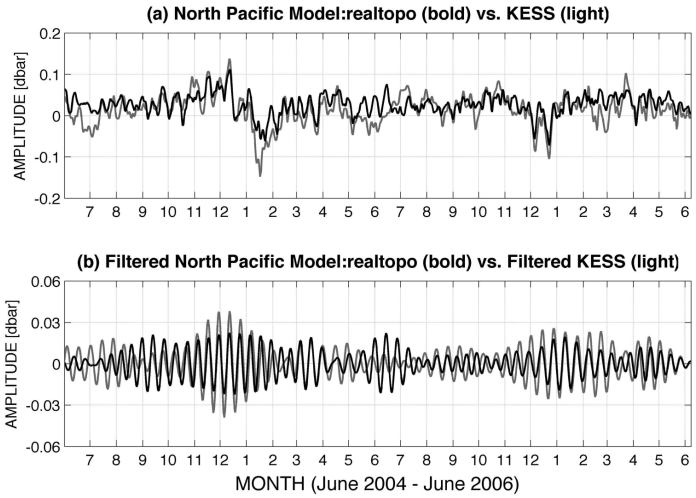

Figure 3. Comparison between the bottom pressure from the North Pacific Barotropic Model (NPBM_realtopo) and KESS sites. Bold and light solid lines represent the mean North Pacific Barotropic Model (NPBM_realtopo) bottom pressure averaged over the KESS_box (red box in Figure 1b) and mean time series of the KESS sites (black dots in Figures 1a and 1b). (a) Unfiltered and (b) band-pass-filtered (11–15 days) time series.

time series are regressed onto the PC time series of the target variable:

$$\mathrm{PC}_i^{(T)}(t) = \sum_{n=1}^{N} a_n \mathrm{PC}_n^{(P)}(t) + \varepsilon(t), \tag{3}$$

where $\mathrm{PC}_n^{(P)}(t)$ is the target PC time series for mode i, $\mathrm{PC}_n^{(P)}(t)$ is the predictor time series for mode n, a_n is the regression coefficient for mode n, and $\varepsilon(t)$ is the regression error. In this study, 10 predictor PC time series are used for the regressions ($N = 10$); the first 10 PC time series explain about 79% and 96% of the wind stress curl and sea level pressure variability in the North Pacific, respectively. Last, the regression patterns of the predictor variable, $\mathrm{CSLV}_n^{(R)}(r, t)$, are obtained using the regression coefficients:

$$\mathrm{CSLV}_n^{(R)}(r,t) = \sum_{n=1}^{N} a_n \mathrm{CSLV}_n^{(P)}(r,t), \tag{4}$$

where $\mathrm{CSLV}_n^{(P)}(r, t)$ are the CSLVs of the predictor variable. The resulting spatial patterns represent the cyclic evolution of the predictor variable, which is physically consistent with the evolution of the target variable based on the regression analysis as in (3). Further details of the regression analysis based on the CSEOF PC time series are presented by *Kim et al.* [2012, section 2]. The relationship between the target mode and predictor variables is investigated by comparing the spatial patterns of the target mode, $\mathrm{CSLV}_i(r, t)$, and the regressed anomalies of the predictor variables, $\mathrm{CSLV}_i^{(R)}(r, t)$.

3. Near 13 Day Ocean Bottom Pressure Variability

[14] Figure 4 shows the first CSEOF mode of the KESS bottom pressure ($\mathrm{CSLV}_1(r, t)$ and $\mathrm{PC}_1(t)$). The 13 daily maps show spatial patterns of the first mode and the site versus time plot (middle) replots these bottom pressures over 13 days (x axis) at the 15 sites (y axis). The sites are arranged as in a Hovmöller plot with the site number increasing from east to west, and they exhibit almost in-phase fluctuations with a slight hint of westward propagation. This mode explains 57% of the near 13 day KESS bottom pressure variance. The second CSEOF mode explains 28% and shows a similar spatial pattern as the first mode, but with 90° (about 3 days) offset (figures not shown here). The 13 daily maps show relatively larger amplitude in the northeastern region and

Table 1. List of the North Pacific Barotropic Model (NPBM) Experiments With Different Conditions of Topography[a]

Experiment	Figure	Topography
NPBM_realtopo	Figures 3, 7, and 9	real topography
NPBM_flat	Figures 8 and 9	flat bottom with 5000 m depth
NPBM_noESC	Figure 9	real topography but no Emperor Seamount Chain

[a]All other conditions are the same for all three experiments.

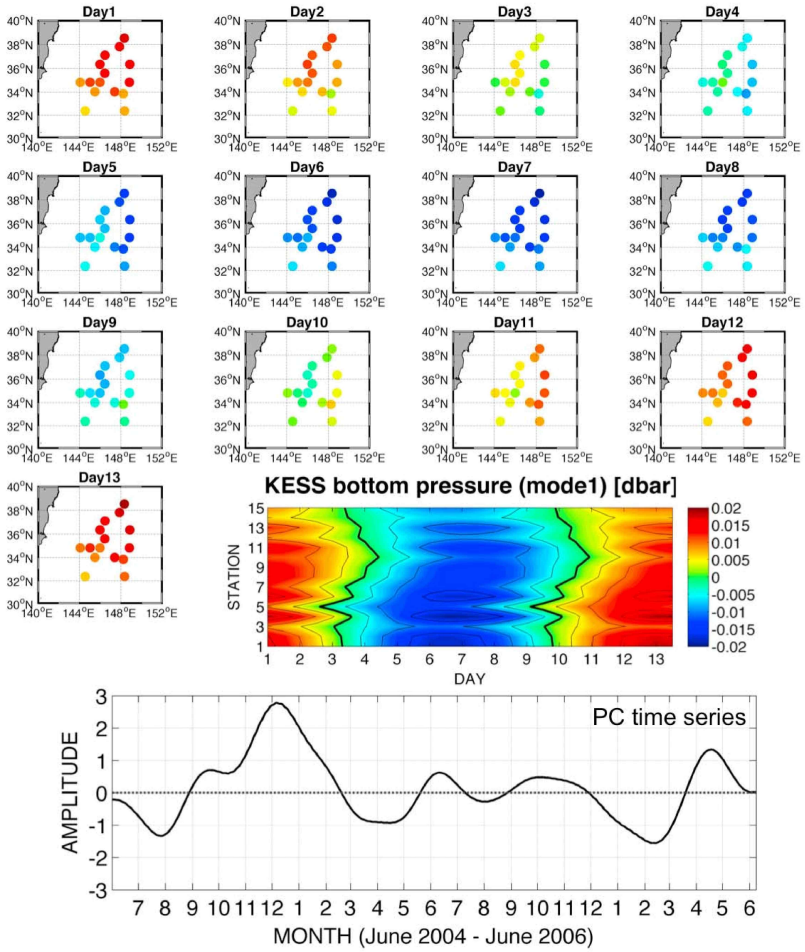

Figure 4. The first CSEOF mode, $CSLV_1(r, t)$, and the corresponding PC time series, $PC_1(t)$, of the bottom pressure at KESS sites. Daily maps (days 1–13) and KESS bottom pressure plot show physical evolution of near 13 day variability at the 15 sites. The strength of the physical evolution depicted in the spatial patterns varies during the observation period, according to the PC time series plot.

smaller amplitude in the southwestern region. The spatial pattern suggests that strong near 13 day variability may extend farther to the northeast than the KESS array.

[15] The corresponding PC time series (Figure 4, bottom) shows the lower-frequency modulation of the 13 day cyclic spatial pattern over the time period from June 2004 to June 2006. Positive (or negative) amplitude in the PC time series indicates that positive (negative) phase in the spatial patterns arrives first (equivalent to 13/2 = 6.5 days of offset). The near 13 day bottom pressure variability is strongest in the 2004–2005 winter, which is consistent with what is inferred from the band-pass-filtered time series in Figure 1d.

[16] It has been known that westward propagating barotropic ocean waves are induced at periods between a week and a month by large-scale atmospheric variability (larger than order of 100 km) [*Willebrand et al.*, 1980; *Gill*, 1982]. Although the westward propagating signal is not very notable in Figure 4, the responsible atmospheric forcing for the

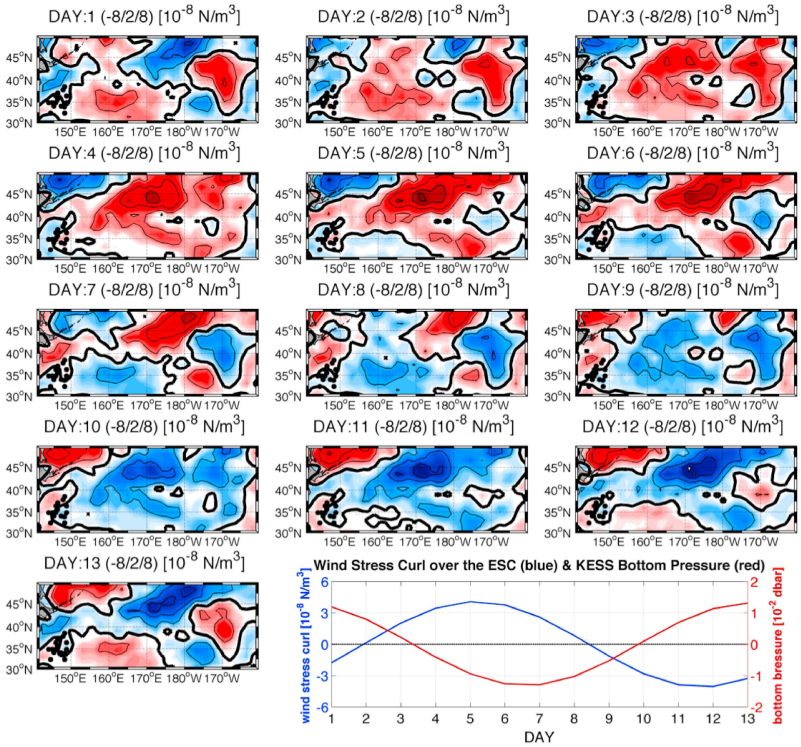

Figure 5. Wind stress curl anomalies, $CSLV_1^{(R)}(r, t)$, regressed onto the first mode of the KESS bottom pressure variability in Figure 4. Contour intervals (minimum/interval/maximum) are shown in the labels. Bold solid lines and black dots represent the zero contours and locations of the KESS sites. The box-averaged regressed wind stress curl anomalies near the Emperor Seamount Chain (ESC, blue box in Figure 1b) and the 15-site-averaged first KESS bottom pressure mode in Figure 4 is also shown and shows the negative relationship between the large-scale wind stress curl and KESS bottom pressure.

near 13 day variability needs to be investigated over a larger domain than the Kuroshio Extension region, as in section 4.

4. Relationship With Atmospheric Variability

[17] The relationship between the near 13 day KESS bottom pressure variability and atmospheric variability in the North Pacific is examined using the regression analysis described in section 2.3. Figure 5 shows the regressed wind stress curl anomalies, $CSLV_1^{(R)}(r, t)$, targeting the first mode of the KESS bottom pressure variability in Figure 4. The r-squared value of the multiple regression is 0.80, which means that low-frequency variability of the wind stress curl spatial patterns in Figure 5 closely follows the low-frequency variability of the KESS bottom pressure (the PC time series in Figure 4) during the time period June 2004 to June 2006. The first mode of KESS bottom pressure variability is large (corresponding to the PC time series in Figure 4) when there are regions of large wind stress curl anomalies as in Figure 5. The interpretation is that the spatial patterns of wind stress curl shown in Figure 5 drive the bottom pressure anomalies shown in Figure 4.

[18] Interestingly, the regressed wind stress curl anomalies in Figure 5 have largest amplitude near the Emperor Seamount Chain (ESC), which is relatively far from the KESS measurements. Note how the positive and negative wind stress curl anomalies propagate eastward and show the largest amplitude near the ESC in Figure 5. The spatial scale of the regressed anomalies is so large as to cover most of the North Pacific. The puzzle of how eastward propagating wind forcing can generate westward propagating oceanic Rossby waves in the 10–30 day band was discussed by *Willebrand et al.* [1980], and observations by *Luther et al.* [1990] reconfirmed that their bottom pressure signals responded to

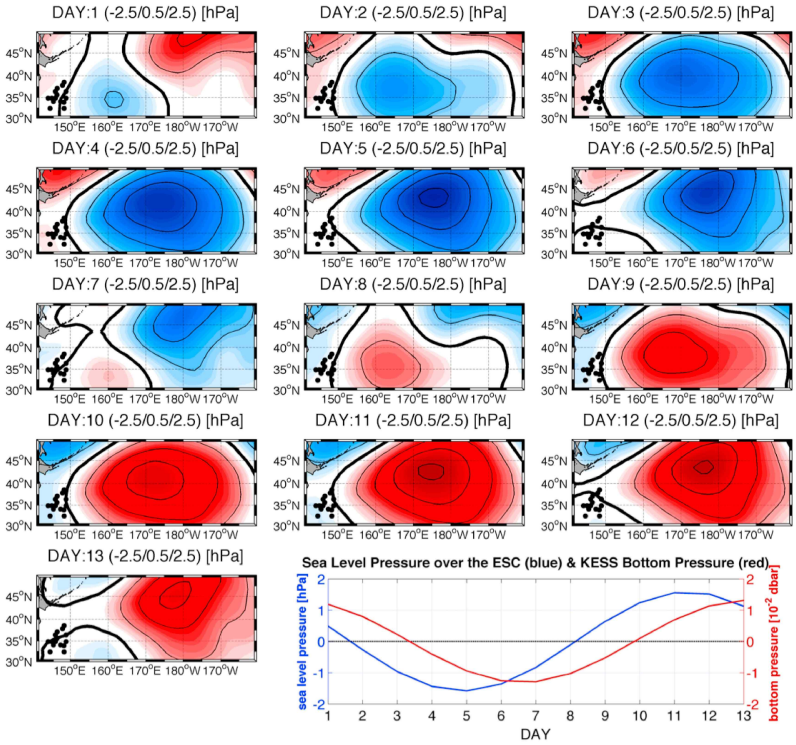

Figure 6. Sea level pressure anomalies, $CSLV_1^{(R)}(r, t)$, regressed onto the first mode of the KESS bottom pressure variability in Figure 4. Contour intervals (minimum/interval/maximum) are shown in the labels. Bold solid lines and black dots represent the zero contours and locations of the KESS sites. The box-averaged regressed sea level pressure anomalies near the Emperor Seamount Chain (ESC, blue box in Figure 1b) and the 15-site-averaged first KESS bottom pressure mode in Figure 4 is also shown. The sea level pressure anomalies are negatively related to the wind stress curl anomalies in Figure 5, consistent with the geostrophic relationship.

wind stress curl forcing to the east of the site. *Gill* [1982] simply states that barotropic waves in the ocean can be produced by the wind and estimates a westward propagating Rossby wave speed based upon the meridional scale of forcing, as discussed in section 5.

[19] The area-averaged time series of wind stress curl anomaly over the ESC box exhibit positive maximum in days 4–6 and negative maximum in days 11–13 (Figure 5, bottom right). The positive phase of the wind stress curl anomalies near the ESC in days 4–6 corresponds to the negative phase of the KESS bottom pressure variability in days 6–8. This 2 day time lag between the wind stress curl near the ESC and KESS bottom pressure is considered in section 5. The negative relationship between wind stress curl and bottom pressure is consistent with Ekman divergence/convergence, e.g., positive wind stress curl induces mass divergence in the ocean and consequently decreases ocean bottom pressure.

[20] North Pacific sea level pressure and KESS bottom pressure exhibit a strong relationship (r-squared value of the regression: 0.74). Figure 6 shows the regressed sea level pressure anomalies in the North Pacific, $CSLV_1^{(R)}(r, t)$, targeting the first mode of the KESS bottom pressure variability. If the response of sea surface height to atmospheric pressure was exactly isostatic ("inverted barometer"), bottom pressure would remain unchanged and there would be no correlation between sea level pressure and bottom pressure. If a correlation between them is observed, it could be explained in two ways. The response of sea surface height is not fully inverted-barometric. Alternatively, the response of sea surface height is related to wind stress curl which itself

is related to the atmospheric pressure [*Ponte*, 1994; *Wunsch and Stammer*, 1997].

[21] The inverted barometric assumption is generally considered to be applicable for time scales longer than 3–4 days and spatial scales larger than 500 km, the dominant atmospheric forcing scales in the North Pacific [*Philander*, 1978; *Chave et al.*, 1992; *Ponte*, 1994]. One notable exception is the near 5 day Rossby-Haurwitz wave [*Luther*, 1982; *Ponte*, 1997; *Hirose et al.*, 2001; *Mathers and Woodworth*, 2004; *Park and Watts*, 2006; *Stepanov and Hughes*, 2006]. Here it is suggested that the significant correlation observed between atmospheric pressure and bottom pressure arises because the sea level pressure anomalies shown in Figure 6 are related geostrophically to the wind stress curl anomalies in Figure 5 and not directly related to the bottom pressure variability. This assertion is supported by the wind-only forced NPBM which reproduces well the bottom pressure variability without including atmospheric pressure forcing (Figure 3).

[22] The area-averaged time series of sea level pressure anomalies over the ESC box exhibit negative maximum in days 4–6 and positive maximum in days 11–13 (Figure 6, bottom right), coinciding with the timing of the regressed wind stress curl anomalies in Figure 5 but with opposite sign. The negative relationship between sea level pressure and wind stress curl is consistent with atmospheric geostrophic balance, e.g., negative sea level pressure is associated with positive wind stress curl. The location and size of the positive and negative anomalies of sea level pressure in Figure 6 match well with those of wind stress curl in Figure 5. This consistency is noteworthy because those anomalies are independently derived from the regression analysis targeting the near 13 day bottom pressure variability in the KESS array in Figure 4.

5. North Pacific Barotropic Model Results

[23] Spatial patterns of the regressed wind stress curl anomalies in Figure 5 (wind forcing responsible for the KESS bottom pressure variability) suggest that the bottom pressure response would occur widely over the North Pacific and not be confined to the region of KESS measurements. To investigate the bottom pressure variability in the wider North Pacific, a wind-forced barotropic model is applied over the North Pacific (NPBM) as described in section 2.2. The NPBM experiments with different conditions of topography are listed in Table 1. The model results with real topography (NPBM_realtopo) agree fairly well with the KESS measurements as seen in Figure 3 (correlation coefficient 0.71) and they are analyzed in the same way as the KESS bottom pressures described in section 2.3.

[24] Figure 7 shows the first CSEOF mode of the bottom pressure variability from NPBM_realtopo. This mode explains about 34% of the near 13 day variance. Spatial patterns of days 1–13 show positive and negative anomalies with westward propagating signals. The corresponding PC time series exhibit largest amplitude during the 2004–2005 winter, consistent with the KESS bottom pressure variability PC time series (Figure 4). The correlation coefficient between the KESS and NPBM_realtopo PC time series is 0.74; this statistically significant correlation suggests that the NPBM_realtopo first mode in Figure 7 is closely related to the KESS bottom pressure first mode in Figure 4.

[25] The significant correlation coefficient (0.74) between the PC time series of the KESS bottom pressure and NPBM_realtopo also implies that regressed wind stress curl and sea level pressure anomalies targeting the NPBM_realtopo first mode for its broad region of the North Pacific would not be very different from those targeting the KESS bottom pressure first mode (Figures 5 and 6); this is confirmed later (Figure 9b). Thus, comparison of spatial patterns in Figures 5, 6, and 7 shows relationship between the bottom pressure variability from NPBM_realtopo and the atmospheric variability. For example, relatively large negative anomalies of the bottom pressure in days 4–6 (Figure 7) match well in time with the relatively large positive regressed wind stress curl anomalies in days 4–6 (Figure 5) and negative sea level pressure anomalies in days 4–6 (Figure 6).

[26] One interesting point is that the large NPBM_realtopo bottom pressure anomalies (Figure 7) are confined in the western region of the North Pacific. Largest amplitudes of the anomalies occur west of the ESC. The area-averaged time series over the W_ESC box shows a negative maximum in days 4–6 and a positive maximum in days 11–13. The area-averaged time series over the KESS_box shows about 2 days delay compared to that over the W_ESC (Figure 7). This 2 day time lag is consistent with the time lag between the wind stress curl anomalies near the ESC and KESS bottom pressure (Figure 5). The interpretation is that the wind stress curl anomalies near the ESC induce bottom pressure anomalies over the W_ESC with no time delay (shorter than resolvable in the daily maps) and the bottom pressure anomalies propagate westward and are observed over the KESS box after 2 days.

[27] Westward propagating phase speed of the barotropic oceanic waves induced by wind forcing can be estimated as β/l^2, where l^{-1} is north-south scale; it is of order 20 m/s with l^{-1} of about 1000 km [*Gill*, 1982]. The propagation speed of the bottom pressure variability in the NPBM_realtopo (Figure 7) can be roughly estimated as 6.6 m/s (determined by dividing the distance between the middle of the W_ESC box (40°N, 160°E) and that of the KESS_box (36°N, 148°E) by 2 days). The north-south scale suggested by Figures 5 and 7 is 600 to 700 km, i.e., shorter than 1000 km, and the corresponding β/l^2 would be about 7 to 10 m/s.

[28] Spatial patterns of the NPBM_realtopo CSEOF mode (Figure 7) suggest that the bottom topography may play an important role in controlling the bottom pressure variability in the North Pacific. In order to investigate the effects of bottom topography, the North Pacific Barotropic Model with 5000 m deep flat bottom (NPBM_flat) is examined. The first mode of the NPBM_flat bottom pressure variability is shown in Figure 8. This mode explains about 31% of the near 13 day variance.

[29] The most notable difference between the NPBM_flat (Figure 8) and NPBM_realtopo (Figure 7) results is that the locations of large anomalies in NPBM_flat are not confined in the western region of the North Pacific, but rather closely located to the large anomalies of wind stress curl (Figure 5). From the NPBM_flat results, the area-averaged time series over the KESS_box in Figure 8 shows about a 2.5 days delay compared to that over the ESC box. Note that the 2.5 days of delay is obtained from the ESC box based on the location of largest anomalies in Figure 8, not from the

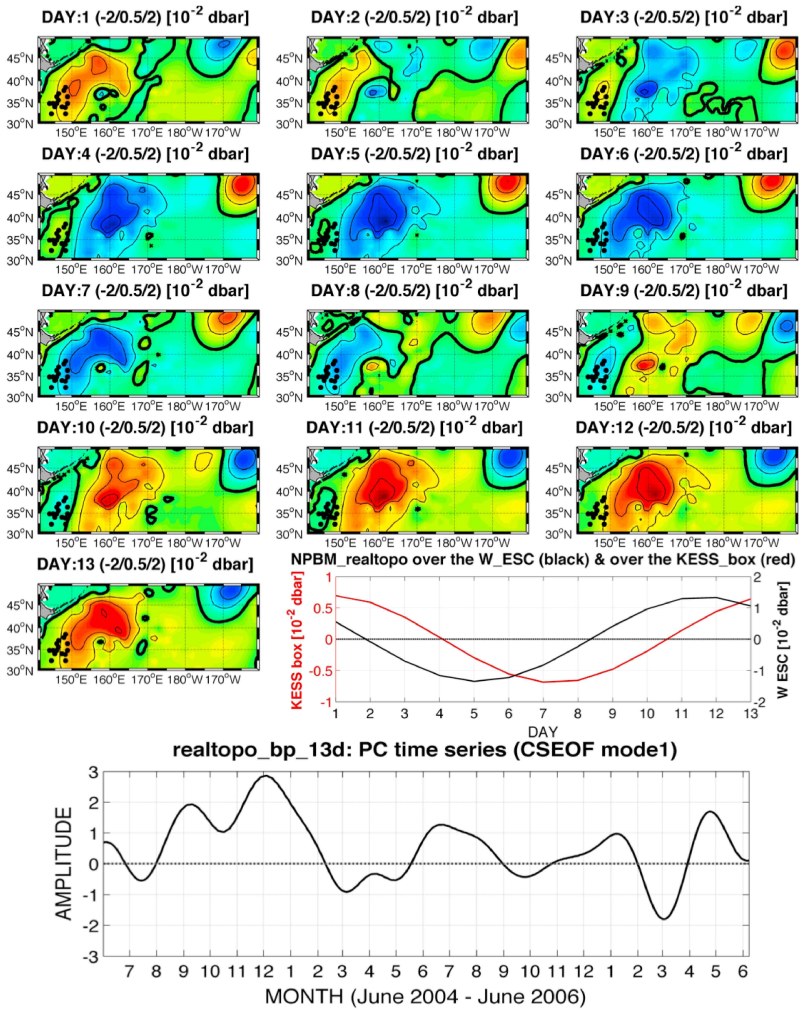

Figure 7. The first CSEOF mode and the corresponding PC time series of the bottom pressure in the North Pacific Barotropic Model with real topography (NPBM_realtopo). Black dots and bold solid lines in the spatial patterns denote the locations of KESS sites and the zero contours. Box-averaged bottom pressure anomalies just west of the Emperor Seamount Chain (W_ESC, black box in Figure 1b) and over the region of KESS measurements (KESS_box, red box in Figure 1b) exhibit westward propagation of the bottom pressure variability in the model results. The strength of the physical evolution depicted in the spatial patterns varies according to the PC time series.

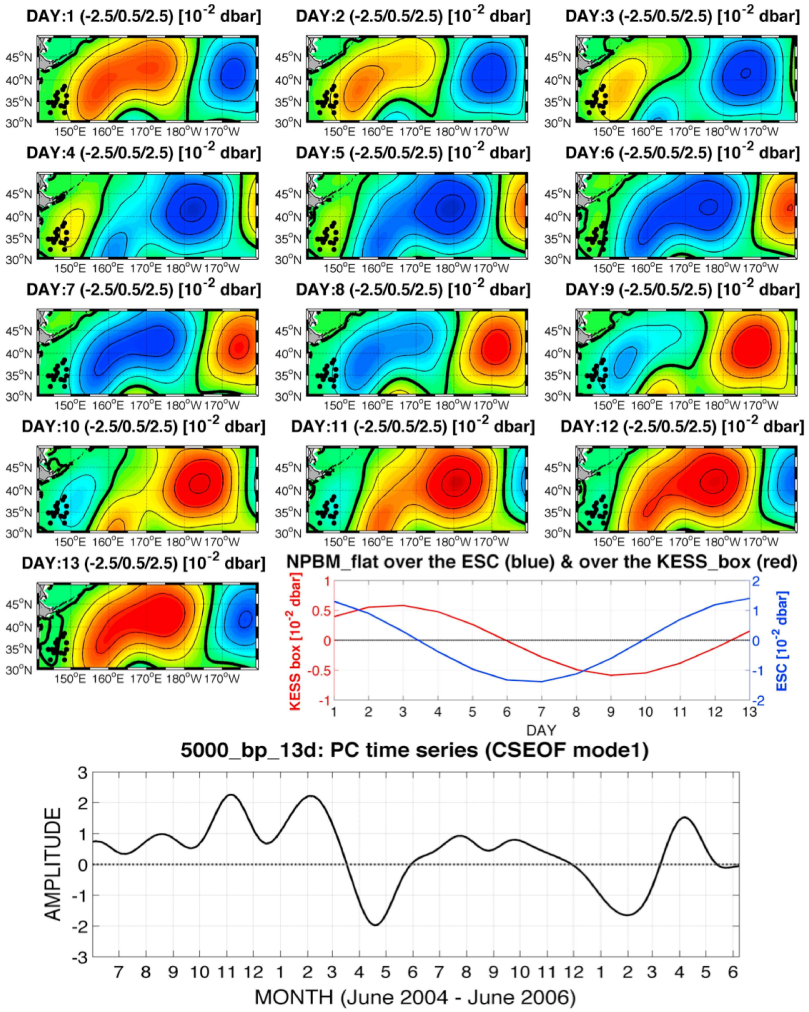

Figure 8. The first CSEOF mode and the corresponding PC time series of the bottom pressure in the North Pacific Barotropic Model with 5000 m depth flat bottom (NPBM_flat). Black dots and bold solid lines in the spatial patterns denote the locations of KESS sites and the zero contours. Box-averaged bottom pressure anomalies over the Emperor Seamount Chain (ESC, blue box in Figure 1b) and over the region of KESS measurements (KESS_box, red box in Figure 1b) exhibit westward propagation of the bottom pressure variability in the model results. The strength of the physical evolution depicted in the spatial patterns varies according to the PC time series.

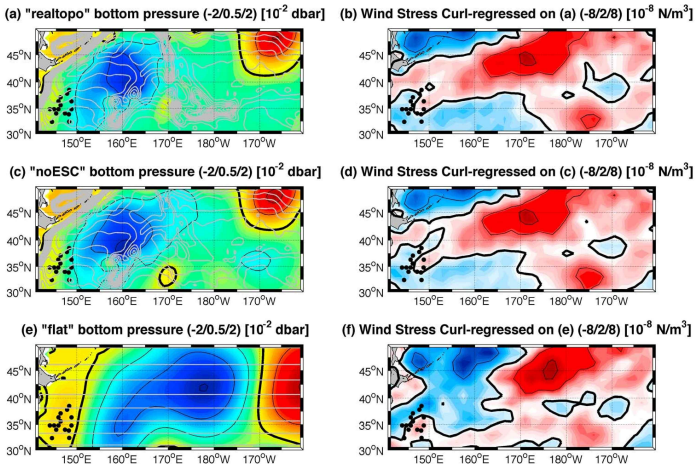

Figure 9. (left) Mean of negative-phase bottom pressure anomalies (days 3–8) in the North Pacific Barotropic Model and (right) mean of regressed wind stress curl anomalies in corresponding positive phase. (a and b) NPBM_realtopo case, where bottom pressure anomalies come from Figure 7. (c and d) NPBM_noESC case. (e and f) NPBM_flat case, where bottom pressure anomalies come from Figure 8. Black dots and bold solid lines denote the locations of KESS sites and the zero contours. Gray lines in Figures 9a, 9c and 9e represent f/H contours ([0.1:0.1:6.0] $\times$ 10^{-8} s^{-1} m^{-1}). Positive wind stress curl anomalies and resulting mass divergence induce negative bottom pressure anomalies to the west of Emperor Seamount Chain (ESC) in Figures 9b and 9d, while the strongest negative bottom pressure anomalies are induced close to the location of positive wind stress curl anomalies in the flat bottom case (Figure 9f).

W_ESC box as in Figure 7. The propagation speed of the bottom pressure variability in the NPBM_flat of 10.6 m/s is roughly estimated by dividing the distance between the middle of the ESC box (45°N, 172.5°E) and that of the KESS_box (36°N, 148°E) by 2.5 days. This propagation speed appears to be as much as 60% faster than that in case of the NPBM_realtopo and is close to the above $\beta/l^2 \sim$ 10 m/s estimate for $l^{-1} \sim$ 700 km [*Gill*, 1982], which is based on a flat bottom ocean. An intriguing question remains of how bottom topography affects the propagation speed, because the large-scale topographic slopes in this region would tend to increase the effective beta, which would not account for the modeled decrease in propagation speed for real versus flat topography.

6. Discussion and Conclusions

[30] The westward propagation signal in the North Pacific was barely detected in the KESS measurements (Figure 4) because of the relatively small longitudinal extent of KESS measurements, which would produce only a half-day lag for the propagation speed indicated by the NPBM_realtopo (Figure 7). This study shows that the near 13 day variability that was observed in the KESS region is a part of the larger-scale bottom pressure variability and is driven by large-scale wind stress curl in the North Pacific. Comparison between the barotropic model results with real topography (NPBM_realtopo) and flat bottom (NPBM_flat) reveals that the bottom topography strongly confines the near 13 day bottom pressure variability to the western North Pacific and slows its westward propagation.

[31] Slower propagation in the NPBM_realtopo compared to the NPBM_flat may be intuitively apparent, considering that wave propagation is constrained by ridges and seamounts and may depend strongly on the shape of bottom topography [*Matano and Palma*, 2005]. However, the limited barotropic response to the east of ESC in the NPBM_realtopo (Figure 7) is not easily explained. Figure 9 summarizes the NPBM results with different conditions of bottom topography (Table 1). An additional experiment with real topography, but removing only the ESC (NPBM_noESC, Figure 9c) shows similar spatial patterns to NPBM_realtopo (Figure 9a). It suggests that the overall bottom topography (f/H contours are shown in Figure 9), not particularly the ESC, controls the western confinement of the barotropic ocean response to atmospheric forcing in the North Pacific. This, however, does not mean that there is little near 13 day variability in the eastern North Pacific. What we showed in Figure 7 is the first mode of the NPBM_realtopo results. Some regions in the east show approximately 80% as high standard deviation as in the west and the variability in the east is captured in the higher modes (not shown). The main point is that the most dominant mode of NPBM_realtopo shows western confinement in

the North Pacific and it is coherent with the variability in the KESS measurements.

[32] The comparison between the NPBM with and without realistic topography (Figures 7, 8 and 9) highlights the effect of bottom topography on the near 13 day barotropic ocean response to atmospheric forcing in the North Pacific. The NPBM results provide insight on the near 13 day bottom pressure variability in the broader region of the North Pacific. However, the NPBM results also raise a lot of questions beyond the scope of this study. Further analysis of the NPBM results in future studies would be helpful to understand more about the topographic effects on barotropic ocean variability in the North Pacific and how they are different for time scales other than the near 13 day period.

[33] **Acknowledgments.** This work was supported by the National Science Foundation as part of the Kuroshio Extension System Study (OCE-0221008, 0827280, and 0851246). J.H.P. was supported by KIOST grants PE98822 and PE98731.

References

Chave, A. D., D. S. Luther, and J. H. Filloux (1991), Variability of the wind stress curl over the North Pacific: Implications for the oceanic response, *J. Geophys. Res.*, *96*(C10), 18,361–18,379, doi:10.1029/91JC02152.

Chave, A. D., D. S. Luther, and J. H. Filloux (1992), The barotropic electromagnetic and pressure experiment 1. Barotropic current response to atmospheric forcing, *J. Geophys. Res.*, *97*(C6), 9565–9593, doi:10.1029/92JC00549.

Condi, F., and C. Wunsch (2004), Measuring gravity field variability, the geoid, ocean bottom pressure fluctuations, and their dynamical implications, *J. Geophys. Res.*, *109*, C02013, doi:10.1029/2002JC001727.

Donohue, K. A., D. R. Watts, K. L. Tracey, M. Wimbush, and J.-H. Park (2008), Program studies the Kuroshio Extension, *Eos Trans. AGU*, *89*(17), 161–162, doi:10.1029/2008EO170002.

Donohue, K. A., D. R. Watts, K. L. Tracey, A. D. Greene, and M. Kennelly (2010), Mapping circulation in the Kuroshio Extension with an array of current and pressure recording inverted echo sounders, *J. Atmos. Oceanic Technol.*, *27*(3), 507–527, doi:10.1175/2009JTECHO686.1.

Egbert, G. D., and R. D. Ray (2003), Deviation of long period tides from equilibrium: Kinematics and geostrophy, *J. Phys. Oceanogr.*, *33*, 822–839, doi:10.1175/1520-0485(2003)33<822:DOLTFE>2.0.CO;2.

Flather, R. A. (1976), A tidal model of the northwest European continental shelf, *Mem. Soc. R. Sci. Liege*, *6*, 141–164.

Gill, A. E. (1982), *Atmospheric-Ocean Dynamics*, Academic, San Diego, Calif.

Hirose, N., I. Fukumori, and R. M. Ponte (2001), A non-isostatic global sea level response to barometric pressure near 5 days, *Geophys. Res. Lett.*, *28*, 2441–2444, doi:10.1029/2001GL012907.

Jayne, S. R., et al. (2009), The Kuroshio Extension and its recirculation gyres, *Deep Sea Res., Part I*, *56*, 2088–2099, doi:10.1016/j.dsr.2009.08.006.

Kim, K.-Y., and G. R. North (1997), EOFs of harmonizable cyclostationary processes, *J. Atmos. Sci.*, *54*, 2416–2427, doi:10.1175/1520-0469(1997)054<2416:EOHCP>2.0.CO;2.

Kim, K.-Y., G. R. North, and J. Huang (1996), EOFs of one-dimensional cyclostationary time series: Computations, examples and stochastic modeling, *J. Atmos. Sci.*, *53*, 1007–1017, doi:10.1175/1520-0469(1996)053<1007:EOODCT>2.0.CO;2.

Kim, K.-Y., H. Na, and J.-G. Jhun (2012), Oceanic response to midlatitude Rossby waves aloft and its feedback in the lower atmosphere in winter Northern Hemisphere, *J. Geophys. Res.*, *117*, D07110, doi:10.1029/2011JD017238.

Luther, D. S. (1982), Evidence of a 4–6 day barotropic, planetary oscillation of the Pacific Ocean, *J. Phys. Oceanogr.*, *12*, 644–657, doi:10.1175/1520-0485(1982)012<0644:EOADBP>2.0.CO;2.

Luther, D. S., A. D. Chave, and J. H. Filloux (1987), BEMPEX: A study of barotropic ocean currents and lithospheric electrical conductivity, *Eos Trans. AGU*, *68*(27), 618, doi:10.1029/EO068i027p00618.

Luther, D. S., A. D. Chave, J. H. Filloux, and P. F. Spain (1990), Evidence for local and nonlocal barotropic responses to atmospheric forcing during BEMPEX, *Geophys. Res. Lett.*, *17*, 949–952, doi:10.1029/GL017i007p00949.

Matano, R. P., E. D. Palma (2005), Energy transmission by barotropic Rossby waves revisited, *J. Phys. Oceanogr.*, *35*, 2228–2236, doi:10.1175/JPO2810.1.

Mathers, E. L., and P. L. Woodworth (2004), A study of departures from the inverse-barometer response of sea level to air-pressure forcing at a period of 5 days, *Q. J. R. Meteorol. Soc.*, *130*, 725–738, doi:10.1256/qj.03.46.

Müller, P., and C. Frankignoul (1981), The direct atmospheric forcing of oceanic eddies, *J. Phys. Oceanogr.*, *11*, 287–308, doi:10.1175/1520-0485(1981)011<0287:DAFOGE>2.0.CO;2.

Park, J.-H., and D. R. Watts (2006), Near 5-day nonisostatic response of the Atlantic Ocean to atmospheric surface pressure deduced from sub-surface and bottom pressure measurements, *Geophys. Res. Lett.*, *33*, L12610, doi:10.1029/2006GL026304.

Park, J.-H., D. R. Watts, K. A. Donohue, and S. R. Jayne (2008), A comparison of in situ bottom pressure array measurements with GRACE estimates in the Kuroshio Extension, *Geophys. Res. Lett.*, *35*, L17601, doi:10.1029/2008GL034778.

Philander, S. G. H. (1978), Forced oceanic waves, *Rev. Geophys.*, *16*(1), 15–46, doi:10.1029/RG016i001p00015.

Ponte, R. M. (1994), Understanding the relation between wind- and pressure-driven sea level variability, *J. Geophys. Res.*, *99*(C4), 8033–8039, doi:10.1029/94JC00217.

Ponte, R. M. (1997), Nonequilibrium response of the global ocean to the 5-day Rossby-Haurwitz wave in atmospheric surface pressure, *J. Phys. Oceanogr.*, *27*, 2158–2168, doi:10.1175/1520-0485(0)027<2158:NROTGO>2.0.CO;2.

Quinn, K. J., and R. M. Ponte (2011), Estimating high frequency ocean bottom pressure variability, *Geophys. Res. Lett.*, *38*, L08611, doi:10.1029/2010GL046537.

Quinn, K. J., and R. M. Ponte (2012), High frequency barotropic ocean variability observed by GRACE and satellite altimetry, *Geophys. Res. Lett.*, *39*, L07603, doi:10.1029/2012GL051301.

Schwiderski, E. W. (1982), Global Ocean Tides, Part X, The fortnightly lunar tide (Mf) atlas of tidal charts and maps, *Tech. Rep. TR 82-151*, Nav. Surf. Weapons Cent., Dahlgren, Va.

Stepanov, V. N., and C. W. Hughes (2006), Propagation of signals in basin-scale ocean bottom pressure from a barotropic model, *J. Geophys. Res.*, *111*, C12002, doi:10.1029/2005JC003450.

Tracey, K., D. Watts, K. Donohue, and H. Ichikawa (2012), Propagation of Kuroshio Extension meanders between 143°E and 149°E, *J. Phys. Oceanogr.*, *42*, 581–601, doi:10.1175/JPO-D-11-0138.1.

Uppala, S. M., et al. (2005), The ERA40 reanalysis, *Q. J. R. Meteorol. Soc.*, *131*, 2961–3012, doi:10.1256/qj.04.176.

Willebrand, J., S. G. H. Philander, and R. C. Pacanowski (1980), The oceanic response to large-scale atmospheric disturbances, *J. Phys. Oceanogr.*, *10*, 411–429, doi:10.1175/1520-0485(1980)010<0411:TORTLS>2.0.CO;2.

Wunsch, C., and D. Stammer (1997), Atmospheric loading and oceanic "inverted barometer" effect, *Rev. Geophys.*, *35*, 79–107, doi:10.1029/96RG03037.

Ocean Sci. J. (2012) 47(4):453-463
http://dx.doi.org/10.1007/s12601-012-0041-3

Article

Available online at http://link.springer.com
SpringerLink

Ocean Science Journal

Tidal Dynamics in the Strong Tidal Current Environment of the Uldolmok Waterway, Southwestern Tip Off the Korean Peninsula

Sok Kuh Kang[1]*, Kyung Tae Jung[2], Ki-Dai Yum[3], Kwang-Soo Lee[3], Jin-Soon Park[3], and Eun Jin Kim[1]
[1]*Ocean Circulation and Climate Research Division, KIOST, Ansan 426-744, Korea*
[2]*Marine Environments & Conservation Research Division, KIOST, Ansan 426-744, Korea*
[3]*Coastal Development & Ocean Energy Research Division, KIOST, Ansan 426-744, Korea*

Received 24 November 2011; Revised 17 September 2012; Accepted 14 December 2012

Abstract – Uldolmok waterway, located between an island off the southwestern tip of Korean peninsula and mainland, is famous for its strong tidal current that has a maximum current of about 6.0 m/s. A series of field observations along with numerical modeling have been carried out in order to understand the tidal dynamics in terms of the force balance along the whole waterway and the energy balance in the narrowest part of the waterway. First, analysis of the ADCP current and the tide level variation data reveals that the tidal dynamics along the total waterway (channel) is balanced dominantly between the pressure gradient and linear bottom frictional forces, with the phase lag of sea level difference for the semi-diurnal constituents leading the current phase about by 10°. Secondly, the result of the numerical modeling reveals that the tidal energy flux vector flows toward the narrowest section, indicating that there should be related nonlinear processes. Through the numerical model experiment with multi-components, the convergence of ($M_2 + S_2$) tidal energy flux of 6.68×10^7 Joule/s in the narrow area of the Uldolmok waterway is explained mainly by the energy consumption of 73% through the nonlinear generation of shallow water components and by the bottom frictional energy dissipation of 27%. This reveals that the remarkably strong nonlinear process dominates in the narrowest section of the Uldolmok waterway, compared with other areas, such as Yellow and East China Seas where the total M_2 energy flux through the open boundary is balanced in terms of the bottom dissipation (Kang et al. 2003; Choi 1980).

Key words – Uldolmok waterway, tidal dynamics, tidal energy balance, tidal model

*Corresponding author. E-mail: skkang@kiost.ac

1. Introduction

The Uldolmok waterway is a channel connecting the entrance of the South Sea and the Yellow Sea (Fig. 1). Its width is of the order of 1-2 km with the total length of about 15 km. The mean water depth is about 15 m. As shown in Fig. 1, the waterway has a narrow section of about 250 m in width. This site is well known for its strong tidal flow. A pre-feasibility study for power generation utilizing these tidal currents was carried out in 1985-1986 by the Korea Ocean Research and Development Institute (1986). And basic research programs were thereafter conducted. In 1992 observations of tidal elevation were made in order to examine the tidal characteristics around the narrow channel and in 2002 further observations were conducted including, for the first time, direct current measurement using ADCP (Acoustic Doppler Current Profiler) for a one month period.

A strong tidal current in the Uldolmok channel was expected to be generated due to the large phase lag difference between both boundary ends of the waterway. Such a large phase lag difference may be attributed to the fact that each boundary is connected to the open seas, with a larger difference in phase lags. This possibility was also hinted at from the result of numerical modeling (Kang et al. 1998), which showed that the M_2 tidal wave propagates from the south both to the Yellow Sea and the East/Japan Sea, and around the southwestern tip of Korean peninsula one branch of the tidal wave propagates to the southeastern boundary of the Uldolmok, while the other tidal wave passes the west of the island, propagating into the northwestern boundary of the

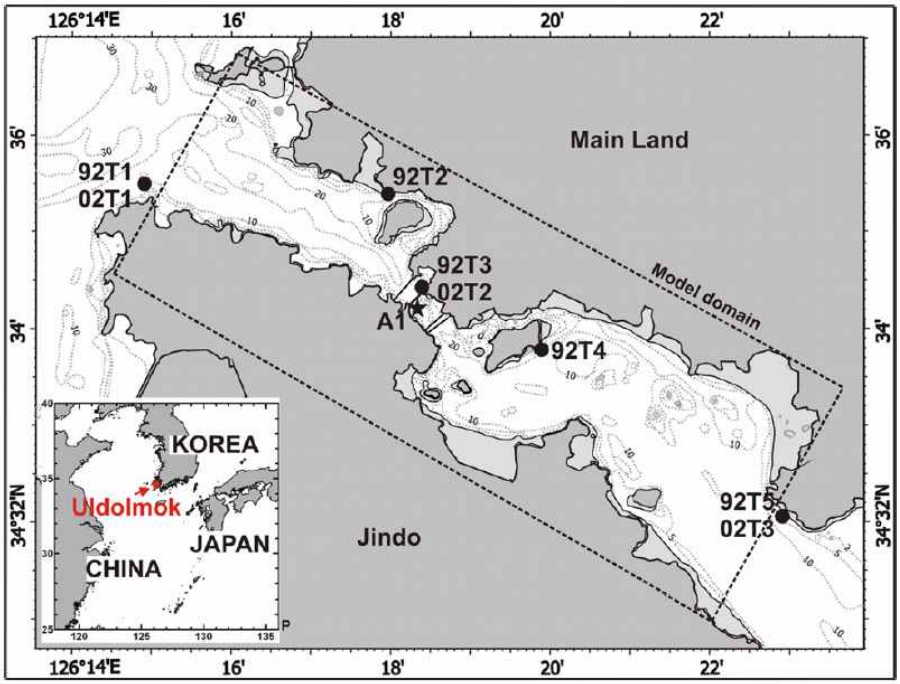

Fig. 1. Tide (92T1(02T1)-92T5(02T5)) (●) and current (A1)(★) stations along the Uldolmok waterway. 92 and 02 in T1-T5 denote observation years of 1992 and 2002

Uldolmok waterway.

Based upon observations and a modeling experiment, Kang et al. (2003) examined the spatial distribution of the constituents M_2 and M_4 in the waterway, confirming that there exists a strong nonlinear process. However, the energy balance was not investigated, even though the topic may be valuable in that the rate of bottom dissipation is very high and that the energy transfer of semi-diurnal constituents to higher harmonics such as the quarter-diurnal, fortnight components and so on may be exceptionally pronounced.

The examination of the dynamic balance along the whole waterway would be an interesting point of investigation, since the prediction by sea level difference between the ends of the channels, based upon the assumption of the dynamic balance between the pressure gradient and bottom friction terms, had been efficiently used by Korea Hydrographic and Oceanographic Administration for the approximate prediction in the narrow channel when the direct current measurement was not made available. In this manuscript we examine how tidal dynamics are balanced in two ways. Firstly, how are the major dynamical terms balanced in the whole waterway? Secondly, we investigated the energy balance, in the narrow section area, among the divergence of the energy flux, the bottom dissipation, and the nonlinear processes of higher and lower harmonics generation, along with the mean sea level change, considering the two major tidal constituents (M_2, S_2). To the authors' knowledge, this energy balance, under a highly nonlinear system, has never been investigated in previous works. Results of simultaneous tide and ADCP current observations were analyzed to examine the tidal dynamics and the energy balance in the narrow strait region was examined after analyzing the model results based upon the depth-averaged numerical modeling.

2. Data Sources, Processing, and Energy Balance Equation

Data sources and processing

Hourly tidal elevation data for one month along the Uldolmok waterway were simultaneously obtained at 5 tidal stations (92T1~92T5) in 1992 as marked in Fig. 1 (for details, see Kang et al. 2003). Tidal station 92T1 was located at the northwestern boundary connected to the Yellow Sea and 92T5 located at the southeastern boundary connected to Southern Sea, with 92T3 being located at the narrowest section of about 300 m. In 2002, to examine the relation between current and sea level variation, a direct current measurement using ADCP was for the first time carried out in the Uldolmok at the narrowest section at a depth of 26 m with a time interval of 5 minutes along with one month measurements of tidal elevation at three tidal stations (02T1 ~ 02T3), where the locations of 02T1, 02T2 and 02T3 were equivalent to those of 92T1, 92T3, and 92T5, respectively. In this work we additionally considered tide data in 2002 to see if the tidal regime changed as a result of some reclamation work carried out in the waterway since 1992, along with the tidal current data measured by ADCP in 2002.

After the basic data process hourly data were collected and the one month hourly data were subjected to harmonic analysis (Foreman 1977; Kang et al. 1995), yielding 27 major constants and 8 inference harmonic constants.

Energy balance equation

Zu et al. (2008), following Garrett (1975), obtained the fully nonlinear energy balance equation. Neglecting the direct generating force and earth tide terms in the Uldolmok waterway, we may write the energy balance equation as follows.

$$\frac{\partial E}{\partial t}+\nabla\cdot(gh\vec{u}\eta)=-\vec{F}\cdot\vec{u}-(h\vec{u}\cdot\nabla\vec{u})\cdot\vec{u}+HA_h\vec{u}\cdot\nabla^2\vec{u} \tag{1a}$$

where $E(=((1/2)H\vec{u}^2+(1/2)g\eta^2))$ denotes the energy density, $h(=(H+\eta))$ the total water depth, η the surface disturbance, H the mean depth, $\vec{u}$ the current vector, $\vec{F}$ the bottom friction vector, A_h the horizontal eddy viscosity. Assuming a steady state and averaging over the tidal cycle with $\rho\times$ (1a), then (1a) becomes

$$-\nabla\cdot\rho g\langle h\vec{u}\eta\rangle = \rho\langle\vec{F}\cdot\vec{u}\rangle+\langle\rho(h\vec{u}\cdot\nabla\vec{u})\cdot\vec{u}\rangle-\langle\rho HA_h\vec{u}\cdot\nabla^2\vec{u}\rangle \tag{1b}$$

where $<>$ denotes the time average. The 1st term of (1b) is the divergence term of the energy flux, the 2nd term the tidal dissipation rate by the bottom friction, the 3rd term the work rate by the non-linear interaction, and the 4th term the dissipation caused by the lateral friction. We examined the energy flux and the bottom flux terms more explicitly in the shallow waters, for application to the narrow section of the Uldolmok tidal waterway, where the last terms can be ignored as follows.

$$-\nabla\cdot\rho g\langle h\vec{u}\eta\rangle=\rho\langle\vec{F}\cdot\vec{u}\rangle+\rho\langle(h\vec{u}\cdot\nabla\vec{u})\cdot\vec{u}\rangle \tag{1c}$$

Integrating (1c) over the small section area (domain S in Fig. 4a) in the waterway yields

$$-\left(\int_{S2}\rho g\langle h\vec{u}\eta\rangle dy-\int_{S4}\rho g\langle h\vec{u}\eta\rangle dy\right)$$
$$=\int_S\rho\langle\vec{F}\cdot\vec{u}\rangle ds+\int_S\rho\langle(h\vec{u}\cdot\nabla\vec{u})\cdot\vec{u}\rangle ds \tag{1d}$$

The barotropic energy flux is usually calculated using the linear term, as done by Kang et al. (2002) and Foreman (1995). However, the barotropic energy flux is now calculated including all the terms of small order, since the strong current speed appears in the Uldolmok waterway. Following Foreman (1995) and Provost and Lyard (1997), the complete barotropic energy flux term in x direction (P_x) instead of the 1st flux term of (1c) is extensively derived as follows.

$$P_x=\frac{1}{T}\int_0^T(H+\eta)\rho\left(\frac{1}{2}|\vec{u}|^2+g\eta\right)udt$$
$$=\frac{1}{T}\int_0^T\left\{\frac{1}{2}\rho H|\vec{u}|^2u+\rho gH\eta u+\frac{1}{2}\rho\eta|\vec{u}|^2u+\rho g\eta^2u\right\}dt$$
$$=\frac{1}{2}\rho gH\hat{U}Z\cos(\phi_z-\phi_u)+\frac{3}{16}\rho Z\hat{U}^3\cos(\phi_z-\phi_u)$$
$$+\frac{1}{16}\rho Z\hat{U}\hat{V}^2\cos(\phi_z+\phi_u-2\phi_v)+\frac{1}{8}\rho Z\hat{U}\hat{V}^2\cos(\phi_z-\phi_u) \tag{1e}$$

Similarly, P_y can be represented as follows.

$$P_y=\frac{1}{2}\rho gH\hat{V}Z\cos(\phi_z-\phi_v)+\frac{3}{16}\rho Z\hat{V}^3\cos(\phi_z-\phi_v)$$
$$+\frac{1}{16}\rho Z\hat{V}\hat{U}^2\cos(\phi_z+\phi_v-2\phi_u)+\frac{1}{8}\rho Z\hat{V}\hat{U}^2\cos(\phi_z-\phi_v) \tag{1f}$$

where T, H, η, Z, $\hat{U}$, $\hat{V}$, ϕ_u, ϕ_v, and and ϕ_z are the tidal period, the mean depth, the surface disturbance, the amplitude of

surface disturbance, u component amplitude, v component amplitude, the phase lag of u, the phase lag of v, and the phase lag of surface disturbance, respectively. Usually the first potential energy terms of equation (1d) and equation (1e) are dominant terms, compared with other terms due to the kinetic energy.

The bottom friction term (the 2nd term of (1c)) is more explicitly presented, as done in Glarioso and Simpson (1994). The mean rate of the total energy dissipation per unit area due to the bottom friction can be estimated by the expression

$$E_d = \rho\langle\vec{F}\cdot\vec{u}\rangle = C_d\rho N^{-1}\sum[u^2(i,j)+v^2(i,j)]^{3/2} \quad (1g)$$

where C_d, ρ, N, $u(i,j)$, and $v(i,j)$ are bottom friction coefficient, water density, the number of data, u and v velocities at grid point (i, j), respectively. The integrated dissipation rate of the work by the bottom friction over the domain S can be obtained by integration over the domain S. The bottom dissipation was also computed in the same way by Kang et al. (2002) for the Yellow and East China Seas and in Kang et al. (2003) for the M_2 along the narrow area in the waterway.

3. Results

Revisit to the characteristics of principal and shallow water tidal components in consideration of the higher and lower harmonics in the energy balance

We will re-examine the nonlinear tidal characteristics in the Uldolmok waterway, based upon both previous work (Kang et al. 2003) and the analysis of additional data measured in 2002, to gain further insights in the following sections. It is evident from the phase lags of the constituents (Table 1) that the tidal waves propagate from 92T5 to 92T1, as also shown in Kang et al. (2003) for the 1992 data. It is noticeable that, in spite of the short distance of about 15 km between the two stations (02T1 and 02T3), a big difference in M_2 phase lag is present over the narrow part of the waterway. This large phase lag difference, with relatively large amplitudes of semi-diurnal constituents, results in the stronger current speeds of semi-diurnal constituents than those of the diurnal constituents. It is likely that, compared with the diurnal constituents, the potential energy of the semi-diurnal constituents is significantly more converted into the kinetic energy, which induces an amplitude decrease toward the narrowest section. The harmonic constants of the major constituents in 2002 show quantitative differences at a certain level compared with those values derived from the 1992 analysis. However, the general trend, such as the decrease in amplitudes toward the narrowest channel, is similar between the observations in 1992 and 2002, even though there had been reclamation work or coastal line changes in the total waterway over the 10 years.

Nonlinear interaction between tidal components leads to the generation of shallow water tides which are usually found in basins or rivers of shallow depth. The results of analyses at 5 stations for the shallow water tides are listed in Table 2. The results of analysis observed both in 1992 and 2002 are more or less similar.

In the case of the overtide, M_4, the amplitudes along the waterway are of the order of 10 cm except for 92T3 (02T2), which is located near the narrowest section of the channel. Interestingly, the variation of amplitude along the waterway is not smooth. Furthermore, the amplitude distributions of the compound tides MS_4 and MN_4 also show the same trend as that of the M_4. In the case of the lower harmonics MSf and MM the amplitudes at 92T3 are larger than those of other stations in contrast to the higher harmonics while the amplitudes at the two open boundaries are smaller, which indicates that a nonlinear generation effect dominates near the narrow section. This feature suggests that much of the energy should be transferred from other major components. Therefore, the generation of higher or lower harmonics should be taken into consideration in the energy balance in

Table 1. Tidal harmonic constants for major components from observed data (Jan. to Feb., 2002 and 1992) along the Udolmok waterway, Korea. Am(cm) denotes tidal amplitude in cm and Ph(ph) phase lag referred to135°E. For the locations of stations, see Fig. 1. Refer to Tables 1 and 2 of Kang et al. (2003) where 1986 and 1992 data was given. In spite of some reclamation work in coastal sites, the trend is similar over the 10 years

Stations	M_2		S_2		K_1		O_1	
	Am(cm)	Ph(deg)	Am(cm)	Ph(deg)	Am(cm)	Ph(deg)	Am(cm)	Ph(deg)
02T1	123.5	21.9	40.6	69.1	31.3	243.9	22.5	211.9
(92T1)	(117.1)	(22.1)	(39.9)	(66.0)	(30.0)	(243.9)	(21.3)	(213.6)
02T2	113.7	15.8	37.7	61.3	29.9	243.1	21.2	213.7
(92T3)	(109.1)	(15.4)	(37.6)	(58.0)	(29.7)	(244.6)	(20.5)	(217.4)
02T3	116.0	333.6	43.6	11.1	30.5	219.9	20.7	188.8
(92T5)	(114.1)	(332.6)	(43.7)	(5.8)	(30.2)	(220.3)	(20.3)	(189.9)

Table 2. Same as in Table 1, except for major shallow water components

Stations	M_4		MS_4		MN_4		MSF		MM	
	Am(cm)	Ph(deg)	Am(cm)	Ph(deg)	Am(cm)	Ph(deg)	Am(cm)	Ph(deg)	Am(cm)	Ph(deg)
02T1 (92T1)	12.4 (11.1)	184.0 (198.1)	10.2 (9.8)	260.5 (262.4)	5.4 (4.6)	164.1 (152.3)	3.5 (1.2)	94.0 (68.2)	1.7 (3.2)	329.2 (150.7)
(92T2)	(9.6)	(186.4)	(8.5)	262.2	(4.0)	(147.0)	(4.8)	(350.8)	(8.8)	(26.5)
02T2 (92T3)	4.2 (2.9)	187.1 (205.3)	4.3 (3.7)	283.8 (294.9)	1.4 (0.6)	144.7 (157.3)	4.7 (13.1)	222.5 (190.6)	2.0 (10.9)	262.8 (233.0)
(92T4)	(8.8)	(159.7)	(7.3)	238.1	(3.6)	(135.4)	(2.0)	(42.6)	(5.4)	(137.6)
02T3 (92T5)	8.8 (7.9)	152.8 (154.0)	7.2 (6.9)	227.4 224.8	3.9 (3.3)	132.2 (120.9)	3.0 (0.4)	134.6 (186.0)	1.8 (4.1)	262.3 (147.6)

the narrow section area. The remarkable characteristics of quarter-diurnal tides or higher harmonics (M_4, MS_4, and MN_4) take place in the phase lag distribution of the above constituents. The phase lag patterns of the quarter-diurnal constituents show that the quarter-diurnal tidal waves propagate from 92T5 to 92T1, but a discontinuous behavior or abrupt jump in phase lag is found at 92T3, which strongly supports the argument that some nonlinear process occurs around the narrowest part of the waterway. One point to remember is that an external M_4 tidal wave may propagate from 92T5 to 92T1, since its existence is expected to be possible from the propagation of the tidal wave around the southwestern peninsula. The results of the depth-averaged two-dimensional numerical model for the M_4 tide in the Yellow and East China Seas in Fig. 6a of Kang et al. (1998) support the interpretation that the external M_4 tide with 10-cm amplitude exists around the southwestern tip of Korean peninsula. Consequently, both the internal generation and outer propagation of the higher harmonics should be considered in evaluating the energy balance in the narrow section area.

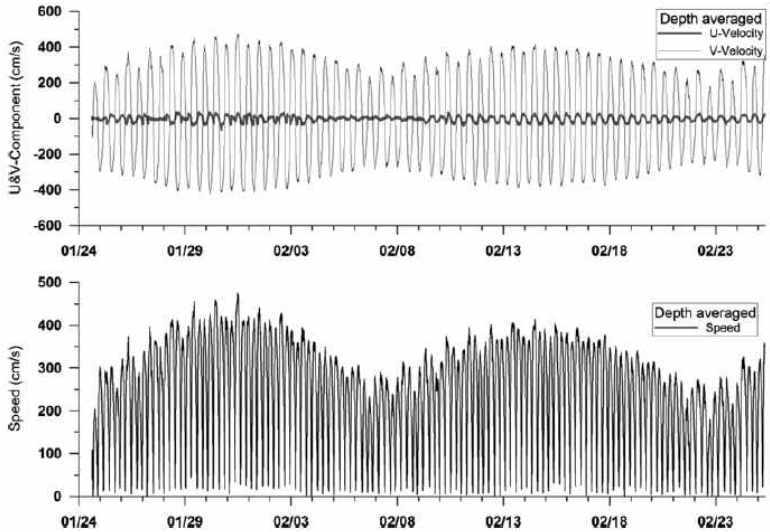

Fig. 2. Depth-averaged along (V)-channel and cross (U)-channel tidal current (upper) and current speed (lower) in the Uldolmok waterway measured by ADCP during Jan. to Feb., 2002

Dynamics along the whole waterway

The tidal current from ADCP mooring in the central point was observed during Jan. to Feb., 2002. Depth averaged along- and cross-channel components of the current are for simplicity shown in Fig. 2. Depth averaged current speed for the whole period is 244 cm/s and the instantaneous maximum depth averaged speed is 475 cm/s, while an instantaneous maximum speed of about 630 cm/s occurs at 23 m from the bottom (total water depth is about 27 m). Based upon the depth averaged current and tide data in 2002, we examined the relation between the tide elevation and the current along the waterway.

It may be instructive to investigate the overall dynamic balance in a channel using a linear theory. The governing equation for a channel of variable cross-section, after integrating the dynamical equation governing the depth averaged flow along the channel and with linear friction assumption, can be given as follows (Garrett and Cummins, 2004):

$$c\frac{dQ}{dt} - g\varsigma_0 = \int_0^L F dx - \frac{1}{2}u_e|u_e| \tag{2}$$

where $c = \int_0^L A^{-1}dx$, $Q(t) = Au$, with A being cross sectional area, $u = u(x, t)$ along-channel current, L length of the channel, $\varsigma_0(t)$ the sea level difference, F opposing force (or natural friction) against pressure gradient to derive the flow, and u_e the exit flow at the end of channel. Assuming the bottom drag is linearly proportional to the current with sinusoidal time variation of sea level difference, the governing equation (Equation (2.4) of Garrett and Cummins (2005)) under the linear assumption is as follows.

$$c\frac{dQ}{dt} - ga\cos\omega t = -\lambda Q \tag{3}$$

where λ is here a linear friction coefficient and a is the amplitude of the sea level difference. The overall tidal dynamic balance in the Uldolmok channel can be examined among local acceleration, pressure gradient, and bottom frictional terms.

In order to analyze the dynamic balance between frictional and pressure gradient terms, the current and tide data that were measured simultaneously are used. Fig. 3 presents the time variation of sea level difference (02T3 minus 02T1) and the depth mean current at the narrowest section. The M_2 amplitude of sea level difference is 0.983 m with the maximum amplitude of about 1.4 (= 0.983 + 0.409) m during the spring tide. The M_2 phase lag (263.7°) of the sea level difference leads the phase lag (275.3°) of the M_2 current by nearly 12, implying that sea level difference or pressure gradient is rather balanced by the linear bottom friction. Considering that perfect balance between the sea level difference and the linear bottom friction can be achieved with 0 difference, the deviation of the balance may be explained additionally by the local acceleration term. Table 3 shows the amplitude and phase lags for the sea level difference (02T3-02T1) and depth mean current (A1) for 5 major

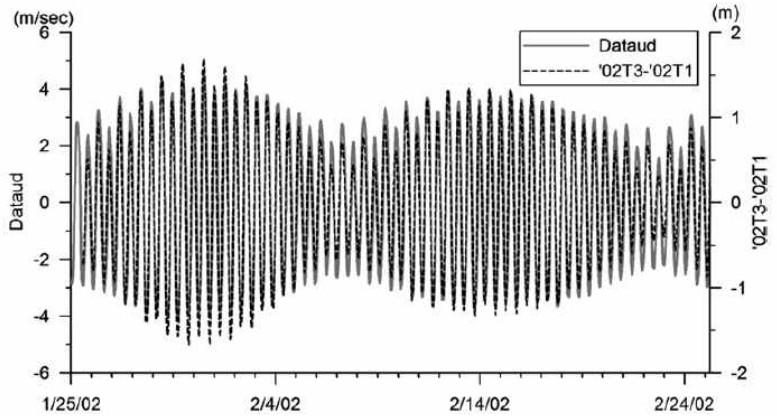

Fig. 3. Observed sea level slope (02T3-02T1) (dotted line) and depth mean along-channel current (solid line) from ADCP observation (Dataud, A1) during Jan. to Feb., 2002

Table 3. Harmonic constants of sea level difference (02T3-02T1) and current (A1) at narrow section for 5 major components. Unit for current amplitude (Am) is m/s, with unit of sea level difference being m

Stations	M_2		S_2		N_2		K_1		O_1	
	Am	Ph	Am	Ph	Am	Ph	Am	Ph	Am	Ph(deg)
02T3-02T1	0.983	263.7°	0.409	313.9°	0.186	243.3°	0.128	138.4°	0.088	99.1°
(A1)	3.316	275.3°	1.119	322.0°	0.592	259.9°	0.385	140.1°	0.262	118.1°

constituents. Phases of the semi-diurnal constituents (M_2, S_2, N_2) in the sea level difference lead the corresponding phase lags of the current constituents by about 10°, while the strong diurnal constituent (K_1) of the sea level difference leads the current by 1.7°, which implies that the longer period wave experiences less friction. Meanwhile the phase difference for the diurnal current (O_1) has a rather larger phase lag of 19.0°. This may be because the O_1 signal has a relatively weak signal, compared with that of the K_1 component. Generally it can be said that the tidal dynamics in semi-diurnal tidal constituents are balanced between the pressure gradient force and the linear frictional force in the Uldolmok waterway, with relatively limited contributions by local acceleration or diffusion.

On the other hand, Leblond (1978) demonstrated in the tidal propagation of the Fraser river, Canada, that the local acceleration term is balanced by the diffusion term. We see that the tidal dynamics in the Uldolmok are quite different even though both of the channels almost take the form of the same one dimensional channel. This can be explained as a difference of the governing system, since both boundaries in the Uldolmok are influenced by the ocean tide, while the river discharge from the upstream dominates in the Fraser river.

Energy balance and convergence of barotropic energy flux

Energy balance (refer to section 2.2), in the waterway with high nonlinearity, deserves special attention, since the nonlinear processes have seldom been examined in previous works. If we consider two constituents (M_2+S_2), the work rate by the nonlinear interaction comprises the work rate through higher and lower harmonics generation and mean sea level distortion in the Uldolmok waterway (section 3.1 and Kang et al. 2003).

Convergence of barotropic energy flux

We considered the detailed tidal current and elevation by the numerical tidal model near the narrow sections to calculate how much barotropic energy flux exists in the narrow section S of the Uldolmok channel. The tidal model KORFLO (KORdi FLOw model in Plan) used in this work has been used for the Yellow and East China Seas (Kang et al. 1998), which was also used for the M_2 and M_4 validation of the tidal model for Uldolmok in Kang et al. (2003). The modeling scheme is based upon the alternating direction implicit (ADI) method and a modeling version upon the spherical polar coordinate system (Kang et al. 1998) was developed, as well as a version under the rectangular coordinate system (Kang et al. 2003). Bottom friction parameters are 0.0025 for the (M_2+S_2) experiment and 0.0027 for the 8 constituent experiment and the coefficient (C_z of equation (4c) in Kang et al. (2003)) of the subgrid scale stress is 0.2. The other details for the modeling system for the Uldolmok waterway are described in Kang et al. (2003).

The model experiments were carried out for the two cases, with the input of 8 constituents (M_2, S_2, K_1, O_1, M_4, MS_4, MSf, S_4) (experiment usur6b) and 2 constituents (M_2 and S_2) (experiment usur7b) in the boundaries. The model grid of 50 m resolution is presented in Fig. 4a and the energy flux (refer to section 2.2) was integrated at the narrowest S2-S4 section area. Fig. 4b presents the validation result of the numerical model result against the observed depth-mean ADCP current. The results of one and half month-long calculations were subjected to the harmonic analysis to yield the harmonic constants of the current and elevation for the energy flux and the tidal charts.

The barotropic energy flux vector from the numerical modeling of the M_2 is presented in Fig. 5, in which energy flux flows toward the central narrowest section. The energy flux from the southern boundary (right boundary in model domain) connected with the South Sea is stronger than that from the northern boundary (left boundary in model domain) connected with the southeastern entrance of the Yellow Sea. The barotropic energy fluxes from the both boundary converge toward the narrow section domain (S), which implies that all the energy should be consumed there. The energy flux pattern of the S_2 is similar to that of the M_2. This converging

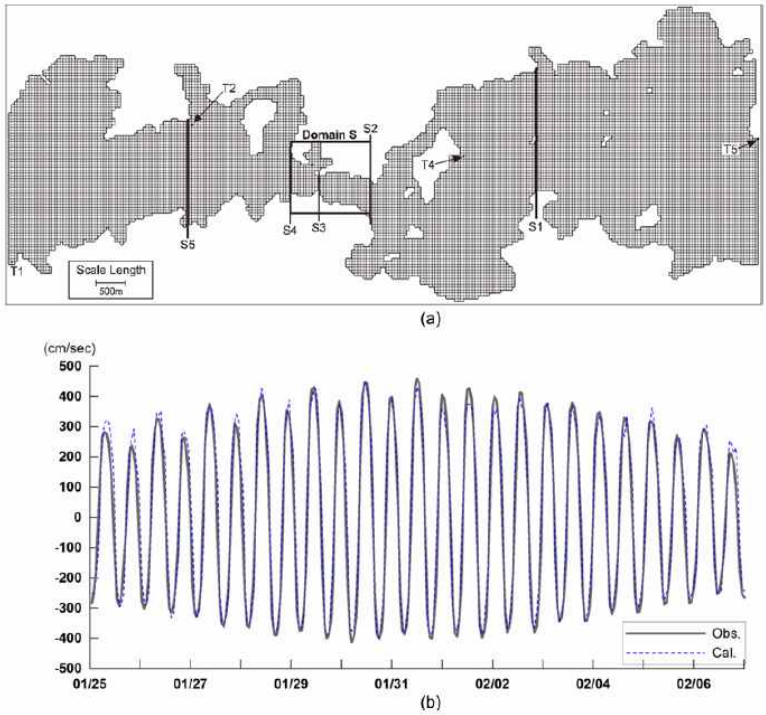

Fig. 4. (a) Grid system of numerical model with sections (S1-S5) where energy flux was computed. Tidal station (T1-T5) denote the tidal stations for open boundary and model validation done in Kang et al. (2003). Energy consumption was integrated over the domain S between section S2 and section S4. (b) Model validation of the depth averaged along-channel current (Obs) from ADCP data (A1) observed in 2002 and model result (Cal). Unit of vertical axis is cm/s

pattern is quite special. The M_2 and S_2 energy fluxes across the cross sections (S2, S4) were calculated. The energy fluxes at sections S2 and S4 are listed in Table 4, for the experiments of usur6b and usur7b. As parameters related to the dissipation, the bottom friction coefficients of 0.0025 and 0.0027 were used for experiments usur6b and usur7b, respectively, since the number of input components affects the mutual friction (Kang et al. 1998).

The total energy flux of the M_2 is about 7 times larger than that of the S2 from both boundaries. The energy flux convergence by $(M_2 + S_2)$ between S2 and S4 section is 6.68×10^7 Joule/s (Watt) for experiment usur6b and 6.48×10^7 Joule/s (Watt) for experiment usur7b. This difference may be due to the varying energy flux of the M_2 and S_2 constituents by nonlinear processes along the boundaries S2 and S4. This amount of the converging energy must be consumed inside the domain by several processes. First, we should consider the $(M_2 + S_2)$ energy dissipation by the bottom friction. Second, some of the power flowing into the narrowest section may be used for higher and lower harmonic constituents (M_4, MS_4, MSf) generation, as discussed in section 3.1, as well as the distortion (depression or rise) of the mean (or residual) sea level.

The integrated work rate over the domain S by the bottom dissipation was calculated based upon the expression of (3f) and integration over the domain S. The work rate by the bottom dissipation is 1.82×10^7 Joule/s for experiment usur6b and 1.75×10^7 Joule/s for the experiment usur7b. It is thought

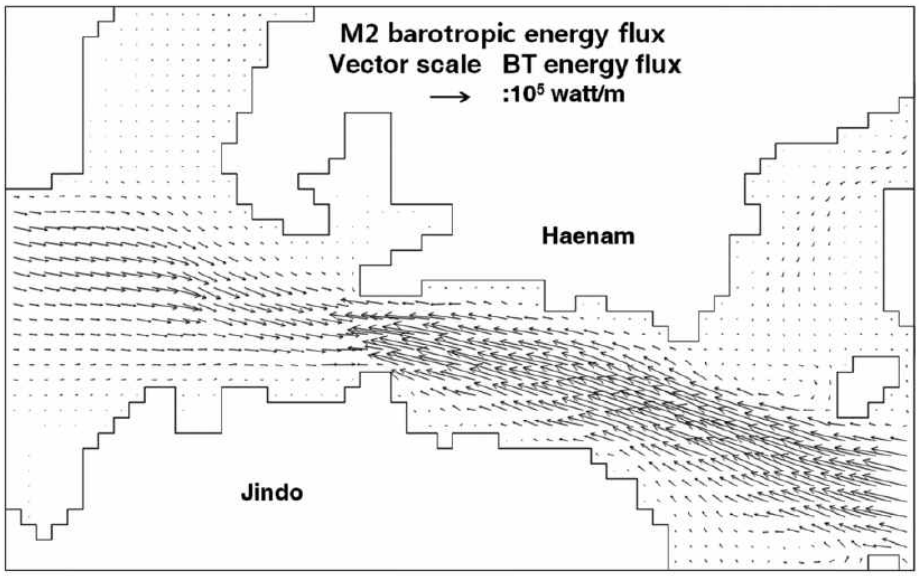

Fig. 5. Barotropic M_2 energy flux vector in the Uldolmok waterway. Energy flux vector flows toward the narrow section. Energy flux from south sea (from east direction in this figure) is stronger

Table 4. Energy flux through S2 and S4 sections, bottom dissipation in area (S) between S2 and S4 (refer to Fig. 4a), and power for generating nonlinear shallow water components. Power input into area between S2 and S4 is denoted by + and power consumption there denoted by -. Unit is 10^7 Joule/s

Experi-ment	Energy flux through S2-S4		Bottom dissipation in area S	Power for generation of shallow components and mean sea level variation in area S
	M_2 S_2	Sum1	Sum2	Nonlinear interaction (M_4,MS_4,MSf, MSL change)
Run6b	5.85 0.83	+6.68	-1.82	-4.86
Run7b	5.67 0.81	+6.48	-1.75	-4.73

that the current speed in the domain S is generally stronger in experiment usur6b than in experiment usur7b. Remarkably the consumption of the work rate by the bottom friction explains only 27% of the converging energy flux toward the narrow section area S. This contribution by the bottom dissipation in the narrow section of the Uldolmok waterway is much less compared with that of the Yellow and East China Seas, where energy flux through boundaries in the shelf of the Eastern East China Sea and Korea Strait is about 12.5×10^{10} Joule/s and bottom dissipation explains more than 90% (or $11\sim12 \times 10^{10}$Joule/s) (Choi 1980).

The work rate by nonlinear process of harmonics generation and MSL distortion

The work done by the nonlinear term is not explicitly calculated due to their complexity. Instead the work rate by the nonlinear term is estimated from the total energy balance of equation (3d), using the explicit values of the work rates both by the bottom friction and the energy fluxes across the open boundaries (S2 and S4 of Fig. 4a).

The barotropic energy flux through the boundaries sections (S2 and S4) of 6.68×10^7 Joule/s (Watt) amounts to all the energy flux input into the narrow section area S in the

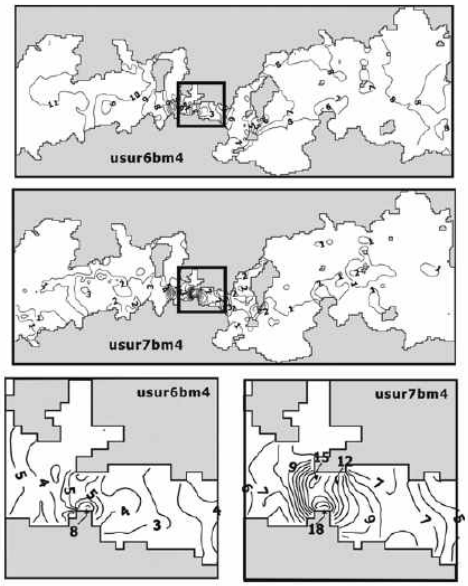

Fig. 6. M_4 co-amplitude lines for experiments run6b and run7b. Amplitudes in subset of experiment usur6b are much smaller than those in amplitudes in subset of experiment usur7b. This indicates that boundary forced M_4 was superposed with generated M_4, yielding the more realistic pattern with less amplitudes in the narrow section area, in the result of the experiment usur6b

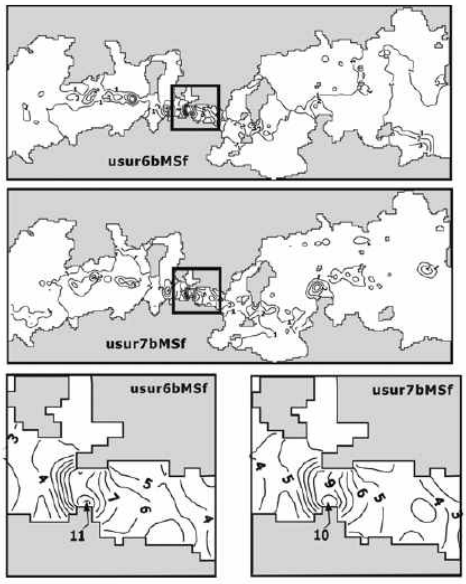

Fig. 7. MSf co-amplitude lines for experiments usur6b and usur7b. Amplitudes in subset of experiment usu6b are similar to those in amplitudes in subset of experiment usur7b. This indicates that the superposition of boundary forced MSf is nearly unnoticeable due to the minor boundary forcing, with magnitude of about 1 cm

Uldolmok waterway. Since the work rate by the lateral friction can be assumed to be negligible in the small region where the barotropic energy flux vector doesn't show any features of eddy motion (see Fig. 5), the incoming barotropic energy flux should be explained in terms of the summation of the work rates both by the bottom friction and by the nonlinear interaction. The efficient understanding of the energy balance for the nonlinear interaction would be through the consideration of the M_2 and S_2 interaction, which generates the major nonlinear components (M_4, MS_4, MSf, S_4).

Actually the nonlinear components, described in the observation result of section 3.1, are dominantly generated in the narrow section. However, the boundary forcing is also strong in the case of the M_4 component with about the 10 cm amplitude forcing. The model results of the amplitude of the higher harmonic component M_4 and the lower harmonic component MSf are presented in Figs. 6 and 7.

The spatial pattern of the M_4 amplitude generated by nonlinear effect, that is, without M_4 open boundary forcing (usur7b), deserves special attention since the M_4 energy looks to be mainly trapped near the narrow section region, with a maximum amplitude of about 15 cm in the narrow section area (bottom right panel of Fig. 6) and 1-2 cm amplitudes outside the narrow section (middle panel of Fig. 6). When the open boundary forcing of the M_4 is given with about 10 cm (experiment usur6b), the M_4 amplitudes in the narrow section decrease down to about 5 cm (bottom left panel of Fig. 6), with about 10 cm amplitude outside of the narrow section (top panel of Fig. 6). Occurrence of smaller M_4 amplitudes of 3~4 cm (02T2 and 92T3 in Table 2) near the narrow section indicates that the superposition of the generated and propagating M_4 tidal waves takes place in reality, since the result of experiment usur6b explains the observed result well. Meanwhile in the case of the MSf constituent, the amplitudes look also to be trapped near the

narrow section (top and middle panel of Fig. 7), whether the MSf boundary forcing is given or not. This is due to the fact that the boundary forcing effects are quite small and only the nonlinear generation effect between the M_2 and S_2 components is dominant near the narrow section.

Therefore, it is expected that the nonlinear process contributes to the energy balance significantly. It would be reasonable to assume that the difference between the integrated barotropic energy flux and the bottom friction corresponds to the work rate by the nonlinear interaction, at about 4.86×10^7 Watt for the experiment usur6b and 4.73×10^7 Watt for the experiment usur7b (Table 4). This amounts to about a 73% portion in the energy balance in the narrow section area S, which indicates that the nonlinear process is a prevailing mechanism in the highly nonlinear Uldolmok waterway. The mean sea level dropping in the narrow sect area (Kang et al. 2003) may also consume power in terms of the nonlinear interaction. The integrated energy flux difference toward the narrow section between experiments usur6b and usur7b may be because the M_2 (S_2) constituents are changed with/without M_4 (S_4) boundary forcing and also with the interaction M_2 (S_2) with M_4 (S_4) near the narrow section.

It would be interesting to estimate the work rate by each nonlinear term, but it would be complicated because the nonlinearity and the explicit estimation of the work rates for the nonlinear terms is beyond the scope of the present work.

4. Conclusions

Uldolmok waterway is famous for its strong tidal current, with a maximum 5 minute mean current speed of about 6.3 m/s observed near surface layer, above 23 m from bottom, in 2002. This implies along with abrupt changes in the waterway width that a strong nonlinear process may exist in the waterway. A theoretical analysis was attempted to explain tidal dynamics in the Uldolmok waterway. Analysis of ADCP current and tide level variation data reveals that the tidal dynamics of the major semi-diurnal components in the whole channel are balanced dominantly between the pressure gradient and linear bottom frictional forces. The tidal energy flux vectors in the waterway deserve careful examination, since the energy flux vector shows a convergent pattern toward the narrowest section. The convergence of the M_2 and S_2 tidal energy fluxes in the narrow section area is explained in terms of the power consumption through the work rate by the total nonlinear generation process (73%) and the bottom frictional dissipation (27%), which is quite different from the basins such as in the Yellow and East China Sea where the energy is mainly balanced between the work rate by the boundary forced energy flux and work rate by the bottom dissipation.

Acknowledgments

First, the author wishes to thank Chris Garrett of University of Victoria for discussing tidal dynamics during his visit to KORDI. We thank the two anonymous reviewers and Dr. Jae Hun Park of KIOST for their valuable suggestions and English correction work. We also would like to thank Mee Kyung Kim for drafting some of the figures. This work has been supported by a grant from KORDI Research programs (PE98812, PE98743, PE98822, and PE98801).

References

Choi BH (1980) A tidal model of the Yellow Sea and the eastern China Sea. KORDI report 80-02, 72 p

Foreman MGG (1977) Manual for tidal height analysis and prediction. Institute of Ocean Science, Sidney, Canada, Pac Mar Sci Rep 77-10, 66 p

Foreman MGG, Walters RA, Henry RF, Keller CP, Dolling AG (1995) A tidal model for eastern Juan de Fuca Strait and the southern Strait of Georgia. J Geophys Res **100**(C1):721-740

Garrett C (1975) Tides in gulf. Deep-Sea Res **22**:23-35

Garrett C, Cummins P (2005) The power potential of tidal currents in channels. Proc Roy Soc A **461**:2563-2572

Glorioso PD, Simpson JH (1994) Numerical modeling of the M_2 tide on the northern Patagonian Shelf. Cont Shelf Res **14**(2/3):267-278

Kang SK, Chung JY, Lee SR, Yum KD (1995) Seasonal variability of the M2 tide in the seas adjacent to Korea. Cont Shelf Res **15**:1087-1113

Kang SK, Yum KD, So JK, Song WO (2003) Nonlinear tidal characteristics along the Uldolmok waterway off the Southwestern tip of the Korean Peninsula. Ocean and Polar Res **25**(1):89-106

Kang SK, Foreman MGG, Lies HJ, Lee JH, Cherniawsky JY, Yum KD (2002) Two-layer tidal modeling of the Yellow and East China Seas with application to seasonal variability of the M2 tide. J Geophys Res **107**(C3):3020. doi:10.1029/2001JC000838

Kang SK, Lee SR, Lie HJ (1998) Fine grid tidal modeling of the Yellow and East China Seas. Cont Shelf Res **18**:739-772

LeBlond PH (1978) On tidal propagation in shallow rivers. J Geophys Res **83**(C9):4717-4721

Zu T, Gan J, Erofeeva SY (2008) Numerical study of the tide and tidal dynamics in the South China Sea. Deep-Sea Res **55**:137-154. doi:10.1016/j.dsr.2007.10.007

GEOPHYSICAL RESEARCH LETTERS, VOL. 40, 392–396, doi:10.1012/GRL.50102, 2013

Stability of the Kuroshio path with respect to glacial sea level lowering

Kyung Eun Lee,[1] Ho Jin Lee,[1] Jae-Hun Park,[2] Yuan-Pin Chang,[3] Ken Ikehara,[4] Takuya Itaki,[4] and Hyun Kyung Kwon[1]

Received 19 November 2012; revised 18 December 2012; accepted 18 December 2012; published 31 January 2013.

[1] We investigate the changes of the Kuroshio Current in the East China Sea during the last glacial maximum, based on numerical experiments using an ocean model and geochemical analyses of marine sediments. Our numerical experimental results indicate that there was little effect of sea-level change on the path of the Kuroshio during the glacial period. Geochemical proxy records of marine sediment cores recovered from inside and outside the Okinawa Trough (OT) show no significant difference in glacial sea surface temperature and planktonic foraminiferal $\delta^{18}O$ between the OT and the Ryukyu forearc. This indicates that the glacial sea surface temperature and salinity were almost the same inside and outside the OT. Hence, during the glacial period, Kuroshio water most likely intruded into the OT and flowed along the shelf break until it drained out through the Tokara Strait. **Citation:** Lee, K. E., H. J. Lee, J.-H. Park, Y.-P. Chang, K. Ikehara, T. Itaki, and H. K. Kwon (2013), Stability of the Kuroshio path with respect to glacial sea level lowering, *Geophys. Res. Lett.*, *40*, 392–396, doi:10.1002/grl.50102.

1. Introduction

[2] The Kuroshio is a strong western boundary current of the subtropical North Pacific gyre. It enters the Okinawa Trough (OT) in the East China Sea (ECS) through the Yonaguni Depression (between Taiwan and the Ryukyus) and its main stream flows northeastward until it drains out through the Tokara Strait. Changes of the Kuroshio Current path during the last glacial maximum (LGM) have been suggested by previous studies. Paleontological studies speculated the migration of the Kuroshio to the east of the Ryukyu Islands during the LGM [e.g., *Ujiié et al.*, 2003]. A recent modeling study also suggests a significant change of the Kuroshio pathway when the sea level was lowered by 80–135 m [*Kao et al.*, 2006]; although the model Kuroshio main stream entered the OT through the Yonaguni Depression during the LGM (as at present), it flowed out through the Kerama Gap located southwest of Okinawa. However, there is still uncertainty regarding the variability of the Kuroshio path during the LGM [e.g., *Kawahata and Ohshima*, 2004].

[3] In this study, we have investigated changes of the Kuroshio in the ECS during the LGM by conducting both numerical and geochemical experiments. First, this study has conducted numerical experiments using an ocean model to calculate flow fields under the different sea-level conditions and hence to test the effects of sea-level change on the Kuroshio. Second, sea surface temperature (SST) and salinity changes during the LGM have been reconstructed based on foraminiferal oxygen isotope and Mg/Ca ratios of marine sediments collected from the Ryukyu forearc. Together with the previously published records, spatial and temporal changes in the SST and SSS both inside the OT and on the Pacific side of the Ryukyu Islands have been investigated to identify Kuroshio variations. Our numerical model results combined with these proxy records provide complementary information on variations of the Kuroshio during the LGM.

2. Material and Methods

[4] The ocean model used in this study is the Regional Ocean Model System version 3.5 which is a free-surface, terrain-following, primitive-equations ocean model (http://www.myroms.org). The model area covers the region of 15°N–52°N in latitude and 115°E–150°E in longitude with grid resolution of 1/8°. There are 50 generalized s-coordinate levels, with increasing vertical resolution toward the surface. We set up model bathymetry with ETOPO5, which is a digital bathymetry dataset with resolution of 5 min (http://www.ngdc.noaa.gov/mgg/global/etopo5.html). Vertical mixing coefficients are calculated from the level 2.5 Mellor-Yamada turbulence closure scheme [*Mellor and Yamada*, 1982].

[5] To calculate momentum, heat, and freshwater fluxes at the sea surface, this model used monthly mean ERA-Interim data with a resolution of 1.5° during the period of 1999–2008. Heat and fresh water fluxes were calculated based on the bulk parameterization of *Fairall et al.* [1996]. The model employed *Flather's* [1976] boundary condition for the barotropic normal velocity components and *Chapman's* [1985] boundary condition for the free surface along the open boundary. The radiation condition of *Marchesiello et al.* [2001] was set for temperature, salinity, and baroclinic velocity components at the open boundary. Additional nudging from real-time ocean forecasting data [*Hirose*, 2011] was included with the radiation condition.

[6] Geochemical analysis was done using gravity core (GH08-2004) materials collected from the continental slope off the Ryukyu forearc during cruise GH08 of Geological Survey of Japan in 2008 by the R/V Haurei No. 2 (26°12.86′N, 128°14.17′E, water depth 1166 m). The core (2.73 m long) is mainly composed of olive gray silty clay. A volcanic-ash

[1]Division of Marine Environment and Bioscience, Korea Maritime University, Busan, South Korea.
[2]Korea Institute of Ocean Science and Technology, Ansan, Korea.
[3]Institute of Marine Geology and Chemistry, National Sun Yat-sen University, Kaohsiung, Taiwan.
[4]Institute of Geology and Geoinformation, Geological Survey of Japan/AIST, Tsukuba Central 7, Tsukuba, Ibaraki, Japan.

Corresponding author: Kyung Eun Lee, Division of Marine Environment and Bioscience, Korea Maritime University, Busan 606-791, South Korea. (kyung@hhu.ac.kr)

0094-8276/13/10.1012/grl.50102

layer was identified as wide spread tephra Kikai-Akahoya erupted 7300 years ago. The ages of core sediments were also determined based on radiocarbon dating. Accelerator mass spectrometry (AMS) ^{14}C dates for planktonic foraminifera from five depths in core GH08-2004 were measured at Beta Analytic Inc. (Table 1, Figure 2a). Calendar ages were converted from radiocarbon ages using CALIB rev. 6.0 [*Stuiver and Reimer*, 1993]. The local reservoir correction, ΔR, was determined to be 44 ± 16 years based on six data values from the Ryukyu Islands [*Yoneda et al.*, 2007]. Planktonic foraminifera *Globigerinoide ruber* (250–350 μm) were picked from the core to measure stable oxygen isotope ratios at 4 cm interval. The oxygen isotopic composition of *G. ruber* was measured at National Taiwan Normal University. The analytical precision of individual oxygen isotope analysis is better than 0.1‰ ($\pm 1\sigma$) as determined by repeated analysis of NIST standards. The Mg/Ca ratio was measured using *G. ruber* from core GH08-2004 in order to reconstruct past sea surface temperature. Cleaning of *G. ruber* mainly followed the method published by *Barker et al.* [2003] modified with more reduction steps. The calculation of paleotemperatures from Mg/Ca ratios was done using a coretop-calibrated function [*Anand et al.*, 2003]. The estimation error was less than 1°C. All Mg/Ca ratios were measured at National Taiwan University with ICP-MS (inductively coupled plasma-mass spectrometry) (Element II).

Table 1. ^{14}C Ages for Core GH08-2004

Sample Depth (cm)	Materials[a]	AMS ^{14}C Age (year BP)	Calibrated Age (year BP)	Lab Code
19.3–21.4	Pl. Foram.	3,530 ± 40	3,370	Beta-260492
40.5–42.7	Pl. Foram.	6,450 ± 40	6,880	Beta-293085
120.9–123.1	Pl. Foram.	11,600 ± 60	13,030	Beta-260493
142.9–145.2	Pl. Foram.	12,940 ± 70	14,300	Beta-260494
225.6–227.9	Pl. Foram.	18,780 ± 100	21,870	Beta-260495

[a]Pl. Floram., planktonic foraminifera.

3. Numerical Experiments

[7] To investigate the effect of sea-level change on the path of the Kuroshio, we conducted two numerical experiments using (i) present sea level (CT) and (ii) sea level 135 m lower than present (CT-135). Time integration was carried out for 20 years, and yearly averaged values for the final year were used for the analysis. Figure 1a shows the flow field at 50 m depth computed for the CT case. The Kuroshio flows along the 200 m isobath after entering the ECS through the Yonaguni Depression and flows out through the Tokara Strait. This result shows reasonably good agreement with the 18 year (1993–2010) mean sea surface velocity pattern of the ECS reconstructed from satellite altimeter measurements, produced by Ssalto/Duacs and distributed by AVISO (http://www.aviso.oceanobs.com/duacs/) (Figure 1c). Notably, the 200 m isobath, shown as a thick blue line in Figure 1c, seems to be a boundary of the Kuroshio main stream, although there are intrusions of the Kuroshio into the shelf region. The appearance of the axis of the Kuroshio along the 200 m isobath also has been reported in previous studies [*Lie et al.*, 1998; *Liu*

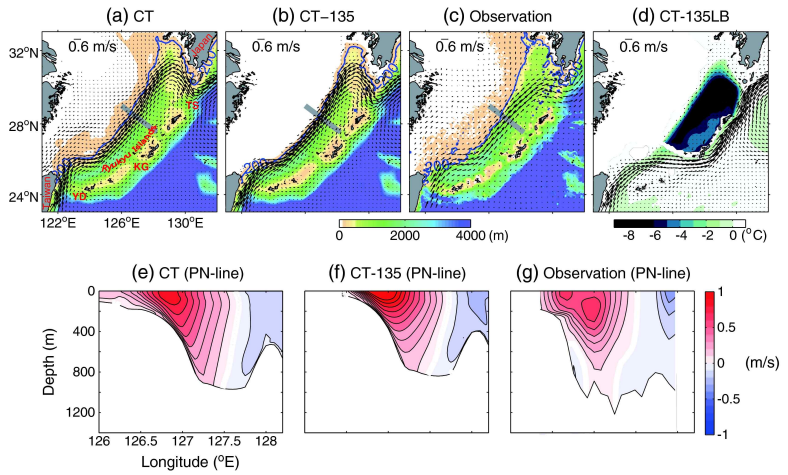

Figure 1. (a) Calculated flow fields at 50 m depth for the CT case. Colors indicate model bathymetry, and the blue line shows the 200 m isobath. Gray line indicates the PN line. YD, KG, and TS indicate Yonaguni Depression, Kerama Gap, and Tokara Strait, respectively. (b) As for Figure 1a, but for the CT-135 case. (c) As for Figure 1a, but for the flow field derived from satellite altimetry data (1993–2010). (d) Calculated flow field in the CT-135LB case. Color indicates seawater temperature difference (at 20 m deep) between CT-135LB and CT-135. (e) Vertical structure of mean velocity across the PN line in the CT case. (f) As for Figure 1e, but for the CT-135 case. (g) Observed mean velocity across the PN line derived from moored instrument data (2003–2004) [*Andres et al.*, 2008]. (e–g) Velocity contours (black, except for a white zero contour) are shown at 0.1 m/s intervals.

and Gan, 2012]. A comparison of our CT run results with the satellite-observed surface velocity indicates that they are consistent with each other.

[8] To check the model performance in another way, we also compared CT model results with long-term mooring measurement data across the PN line (gray lines in Figures 1a, 1b, and 1c), which were recovered from six current-and-pressure-recording inverted echo sounders and two acoustic Doppler current profilers from October 2003 to November 2004 [*Andres et al.*, 2008]. Modeled and measured vertical distributions of mean velocity are illustrated in Figures 1e and 1g, respectively. Both results show positive (northeastward) flow over the continental slope and negative (southwestward) flow further offshore. The negative flow has been reported as a re-circulation flow between the Kuroshio and the Ryukyu Islands [*Oka and Kawabe*, 2003; *Andres et al.*, 2008]. The strongest positive velocity is 0.8 m/s in the model and 0.65 m/s in the observations. It is notable that the positive and negative flows extend vertically to the seafloor in both results, and the boundaries between the two regions also correspond well with each other.

[9] For the CT-135 case, the simulated flow field at 50 m depth and vertical distribution of velocity across the PN line are shown in Figures 1b and 1f, respectively. A comparison of these with the CT results shows that the sea-level change has little effect on the path of the Kuroshio in the ECS, but the maximum velocity is about 25% stronger in the CT-135 case than in the CT case. This result is in contrast to *Kao et al.'s* [2006] result: according to their results, the main outflow of the Kuroshio switched from the Tokara Strait to the Kerama Gap when the sea level was lowered by 80 m. Under present sea-level conditions, the Kuroshio axis in their simulation seems to be more deflected toward the Kerama Gap after entering the ECS than the measurement data shown. It is plausible that bathymetry around the OT was not much changed by the glacial sea-level change, even though the total depth decreased overall. The present sill depth is about 800 m around the Yonaguni Depression, and thermocline is approximately shallower than 400 m deep. Since the sill depth is much deeper than thermocline, there is little influence of sill-depth change on the thermocline change during the glacial period. Therefore, despite the 135 m lowering of sea level, the Kuroshio is still expected to flow along the 200 m isobath after entering the ECS and to leave the ECS through the Tokara Strait.

[10] Table 2 lists the simulated mean volume transports across the PN line. The positive and negative volume transports are estimated from the positive and negative velocities in the cross-section, respectively, and the net transport indicates the difference between them. The simulated transports for the CT case are comparable to those observed: the net transport corresponds to approximately 90% of the observed one. According to our results, the net transport decreased by about 22% in the CT-135 case compared to the CT case. We consider the possibility that a portion of the Kuroshio might be blocked by decreasing sea level at the entrance strait (Yonaguni Depression) when the sea level is lowered by 135 m. *Kao et al.* [2006] also calculated the annual mean volume transports integrated for the upper 800 m along three lines in the OT. The present-day estimated volume transport was approximately 30 Sv around the PN line, which is about 60% larger than the observed PN-line value. According to them, when the sea level was lower by 135 m, the volume transport decreased by 40% and most of it flowed out of the ECS through the Kerama Gap, which is different from our results.

Table 2. Mean Absolute Volume Transports Across the PN Line (1 Sv = 10^6 m^3/s)

	OBS[a]	Model	
	(Sv)	CT (Sv)	CT-135 (Sv)
Positive Transport	24.0	21.1	16.7
Negative_R[b]	−4.9	−4.5	−3.5
Negative_C[b]	−0.5	0.0	−0.2
Net	18.5	16.6	13.0

[a]OBS is the observed mean transport from October 2003 to November 2004 [*Andres et al.*, 2008].
[b]Negative_R and Negative_C mean recirculation and countercurrent transports, respectively (defined by *Andres et al.*, [2008]).

[11] Here, we considered only the effect of sea-level change on the Kuroshio in the numerical experiments. Other factors such as atmospheric pressure systems, wind, and monsoon changes during the glacial period should also be considered. These will be discussed later. More importantly, however, we present geochemical proxy results in the following section. The proxy records which are comparable to the "observational" data are substantially significant in understanding the glacial changes.

4. Proxy Records

[12] We examined the SST proxy records from marine sediment cores to investigate the glacial Kuroshio. First of all, the influence of the Kuroshio on the SST change in the OT was tested by conducting another numerical experiment (CT-135LB case, Figure 1d). In the experiment, land bridges were inserted in the middle of the OT and Ryukyu Islands at the CT-135 case (see white bridge in Figure 1d). Results show that when the Kuroshio flows out through the Kerama Gap, the temperature at 20 m depth in the northern part of the OT decreases by 6°C to 8°C (Figure 1d). A steep SST gradient of 6°C to 8°C across the Kuroshio is a typical feature in the ECS [e.g., see Figure 1 in *Xie et al.*, 2002], and sporadic intrusions of the Kuroshio front into shelf and coastal waters south of Japan have been reported to cause sudden SST changes of about 4°C within few days [e.g., *Isobe et al.*, 2012]. Thus, the SST change caused by the land bridges is considered to be reasonable in the ECS. The CT-135LB result suggests that if the glacial Kuroshio did not enter the northern OT or if its main stream flowed out through the Kerama Gap, the OT would be occupied by relatively cold water, instead of the warm Kuroshio. The glacial SST would then be different inside and outside the OT. Hence, we reconstructed past SST outside the OT and compared the results with those inside the OT. The Mg/Ca ratio of *G. ruber* measured for core GH08-2004 (located on the Pacific side) is illustrated in Figure 2b. They are compared with previously published results from cores located inside the OT in Figure 2b. In particular, we consider only the Mg/Ca proxy values because they are comparable with each other. The coretop value indicates the averaged value for the interval between 0 and 3 cal kyr BP, and the LGM value corresponds to the interval between 18 and 21 cal kyr BP. Mg/Ca ratio-based temperature estimates indicate that coretop-LGM SST difference is 3°C to 4°C for all cores (see Figure 2). Hence, there was no

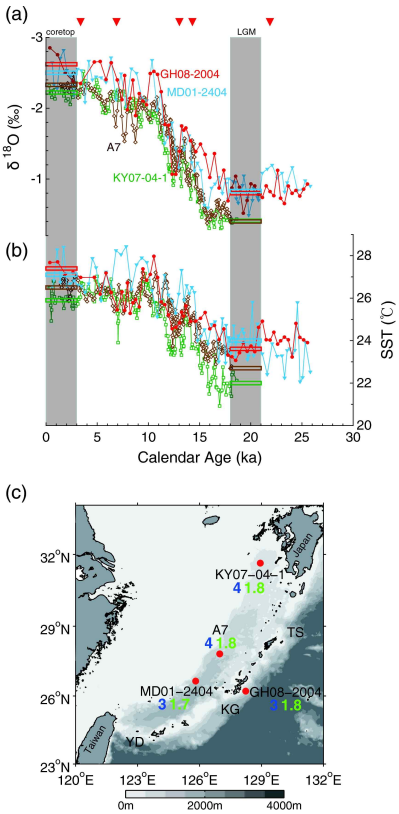

Figure 2. (a) $\delta^{18}O$ and (b) Mg/Ca temperature of *G. ruber* of cores from inside the Okinawa Trough and core from Ryukyu forearc. (c) Difference in Mg/Ca-based SST between coretop and glacial (blue) and difference in $\delta^{18}O_{pf}$ between coretop and glacial (green) reconstructed from cores. Cores used are KY07-04-1 [*Kubota et al.*, 2010], A7 [*Sun et al.*, 2005], MD12404 [*Chang et al.*, 2009; *Chen et al.*, 2010], and GH08-2004 (this study). Red arrow heads indicate radiocarbon date of GH08-2004. Gray color indicates bathymetry.

significant difference in the glacial-interglacial SST change between the OT and Ryukyu forearc. This implies that Kuroshio water at least intruded into the glacial OT and flowed along its western continental slope, which is consistent with the numerical experimental results.

[13] OT water characteristics could have been significantly influenced by variations in the large input of fresh water from the Changiang River, especially when the estuary shifted to the east during low sea levels [cf., *Chang et al.*, 2009]. However, the reconstructions of glacial salinity based on the oxygen isotope and Mg/Ca temperature of *G. ruber* demonstrate that there is little difference in the surface salinity during the LGM compared to today. The difference between the average $\delta^{18}O$ values of *G. ruber* measured for the coretop interval and those of the glacial is about 1.8‰, and the SST difference is about 3°C (Figure 2). If the ice volume effect is 1.2‰ [*Fairbanks*, 1989], the residual $\delta^{18}O$ is 0.6‰. If we consider 0.2‰/°C [*Erez and Luz*, 1983], this residual entirely corresponds to the temperature change. It means that there is little salinity change and there is little influence of fresh water near the central part of the OT. In addition, the carbon isotopic composition of organic matter measured from the bulk sediments of the core used by *Chang et al.* [2009] indicates that the organic matter deposited at this site during the LGM is mostly of marine origin. Pollen data in the sediments of the central OT also indicate that the pollen was transported from the New Guinea/Indonesia/Malaysia/Philippine region to the OT most likely by the Kuroshio Current during the LGM [*Kawahata and Ohshima*, 2004]. These observations all indicate that the Kuroshio water intruded into the OT during the glacial period. Although there may have been an influence of fresh water on the continental shelf during the glacial period, the effect appears to have been minimal in the OT.

[14] Variations in the flow pattern of the Kuroshio could have been induced by variation in intensity of the trade winds and westerlies associated with the subtropical North Pacific high pressure. *COHMAP members* [1988] demonstrated that the subtropical high was displaced to the south and weakened during the LGM. Hence, the subtropical gyre system of the North Pacific was shifted southward and weakened in its intensity during the LGM. Geological records of marine sediment cores from the North Pacific support these [e.g., *Kent et al.*, 1971; *Sawada and Handa*, 1998]. Our records indicate that the Kuroshio path in the ECS appears to have followed closely the steep continental slope during the LGM, although its transport may have been reduced. This Kuroshio transport may have been related to that of the North Equatorial Current which, in turn, was influenced by trade-wind strength in the eastern equatorial North Pacific. It has been suggested that latitudinal changes in the position of the subarctic boundary associated with the westerly jet could also be related to the tropical Pacific changes [*Yamamoto et al.*, 2005]. During the deglaciation, the subtropical high intensified gradually. This may have strengthened the subtropical North Pacific circulation, which in turn, led to the strengthening of the Kuroshio.

[15] **Acknowledgments.** We thank the reviewers and the Editor for their constructive comments and suggestions. This work was supported by CATER 2012–7050 (K.E. Lee) and KIOST in-house project PE98822 (J-H Park), and Grant-in-Aid for Young Scientists (21740373 by JSPS (T. Itaki)).

References

Anand, P., H. Elderfield, and M. H. Conte (2003), Calibration of Mg/Ca thermometry in planktonic foraminifera from a sediment trap time series, *Paleoceanography*, *18*(2), 1050, doi:1010.1029/2002PA000846.

Andres, M., M. Wimbush, J.-H. Park, K.-I. Chang, B.-H. Lim, D.R. Watts, H. Ichikawa, and W.J. Teague (2008), Observations of Kuroshio flow variations in the East China Sea, *J. Geophys. Res.*,*113*, C05013, doi:10.1029/2007JC004200.

Barker, S., M. Greaves, and H. Elderfield (2003), A study of cleaning procedures used for foraminiferal Mg/Ca paleothermometry, *Geochem. Geophys. Geosyst.*, *4*(9), 8407, doi:8410.1029/2003GC000559.

Chang, Y. P., M. T. Chen, Y. Yokoyama, H. Matsuzaki, W. G. Thompson, S. J. Kao, and H. Kawahata (2009), Monsoon hydrography and productivity changes in the East China Sea during the past 100,000 years: Okinawa

Trough evidence (MD012404), *Paleoceanography*, *24*, PA3208, doi:10.1029/2007PA001577.
Chapman, D. C. (1985), Numerical treatment of cross-shelf open boundaries in a barotropic coastal ocean model, *J. Phys. Oceanogr.*, *15*, 1060–1075.
Chen, M. T., X. P. Lin, Y. P. Chang, Y. C. Chen, L. Lo, C. C. Shen, Y. Yokoyama, D. W. Oppo, W. G. Thompson, and R. Zhang (2010), Dynamic millennial-scale climate changes in the northwestern Pacific over the past 40,000 years, *Geophys. Res. Lett. 37*, L23603.
COHMAP Members (1988), Climate changes of the last 18,000 years: Observations and model simulations, *Science*, *241*, 1043–1052.
Erez, J., and B. Luz (1983), Experimental paleotemperature equation for planktonic foraminifera, *Geochim. Cosmochim. Acta*, *47*, 1025–1031.
Fairall, C. W., E. F. Bradley, D. P. Rogers, J. B. Edson, and G. S. Young (1996), Bulk parameterization of air-sea fluxes for tropical ocean-global atmosphere Coupled Ocean-Atmosphere Response Experiment, *J. Geophys. Res.*, *101*, 3747–3764.
Fairbanks, R. G. (1989), A 17,000-year glacio-eustatic sea level record: Influence of glacial melting rates on the Younger Dryas event and deep-ocean circulation, *Nature*, *342*, 637–642.
Flather, R. A. (1976), A tidal model of the northwest European continental shelf, *Mem. Soc. R. des Sci. Liege*, *6*, 141–164.
Hirose, N. (2011), Inverse estimation of empirical parameters used in a regional ocean circulation model, *J. Oceanogr.*, *67*, 323–336.
Isobe, A., S. Kato, X. Guo, and H. Takeoka (2012), Ensemble numerical forecasts of the sporadic Kuroshio water intrusion (kyucho) into shelf and coastal waters. *Ocean Dynam.*, *62*, 633–644.
Kao, S. J., C.-R. Wu, Y.C. Hsin, and M. Dai (2006), Effects of sea level change on the upstream Kuroshio Current through the Okinawa Trough. *Geophys. Res. Lett.*, *33*, L16604, doi:10.1029/2006GL026822.
Kawahata, H., and H. Ohshima (2004), Vegetation and environmental record in the northern East China Sea during the late Pleistocene. *Global Planet. Change*, *41*, 251–273.
Kent, D., N. D. Opdyke, and M. Ewing (1971), Climate changes in the North Pacific using ice-rafted detritus as a climate indicator, *Geol. Soc. Am. Bull.*, *82*, 2741–2754.
Kubota, Y., K. Kimoto, R. Tada, H. Oda, Y. Yokoyama, and H. Matsuzaki (2010), Variations in East Asian summer monsoon since the last deglaciation based on Mg/Ca and oxygen isotope of planktonic foraminifera in the northern East China Sea, *Paleoceanography*, *25*, doi:10.1029/2009PA001891.
Lie, H. J., C. H. Cho, J. H. Lee, P. P. Niiler, and J. H. Hu (1998), Separation of the Kuroshio water and its penetration onto the continental shelf west of Kyushu, *J. Geophys. Res.*, *103*, 2963–2976.
Liu, Z., and Gan, J., 2012. Variability of the Kuroshio in the East China Sea derived from satellite altimetry data. *Deep Sea Res. I*, *59*, 25–36.
Marchesiello, P., J. C. McWilliams, and A. F. Shchepetkin (2001), Open boundary conditions for long-term integration of regional ocean models, *Ocean Model.*, *3*, 1–20.
Mellor, G. L., and T. Yamada (1982), Development of a turbulence closure model for geophysical fluid problems, *Rev. Geophys.*, *20*, 851–875.
Oka, E., and M. Kawabe (2003), Dynamic structure of the Kuroshio south of Kyushu in relation to the Kuroshio path variations, *J. Oceanogr.*, *59*, 595–608.
Sawada, K. and N. Handa (1998), Variability of the path of the Kuroshio ocean current over the past 25,000 years, *Nature*, *392*, 592–595.
Stuiver M., and P. J. Reimer (1993), Extended ^{14}C database and revised CALIB radiocarbon calibration program, *Radiocarbon*, *35*, 215–230.
Sun, Y.B., D. W. Oppo, R. Xiang, W. G. Liu, S. Gao (2005), Last deglaciation in the Okinawa Trough: Subtropical northwest Pacific link to Northern Hemisphere and tropical climate, *Paleoceanography*, *20*, PA4005.
Ujiié, Y., H. Ujiié, A. Taira, Y. Nakamura, and K. Oguri (2003), Spatial and temporal variability of surface water in the Kuroshio source region, Pacific Ocean, over the past 21,000 years: evidence from planktonic foraminifera. *Mar. Micropaleontol.*, *49*, 335–364.
Xie, S.-P., J. Hafner, Y. Tanimoto, W.T. Liu, H. Tokinaga, and H. Xu (2002), Bathymetric effect on the winter sea surface temperature and climate of the Yellow Sea and East China Sea, *Geophys. Res. Lett.*, *29*, doi:10.1029/2002GL015884.
Yamamoto, M., R. Suemune, and T. Oba (2005), Equatorial shift of the subarctic boundary in the northwestern Pacific during the last deglaciation, *Geophys. Res. Lett.*, *32*, doi:10.1029/2004GL021903.
Yoneda, M, H. Uno, Y. Shibata, R. Suzuki, Y. Kumamoto, K. Yoshida, T. Sasaki, A. Suzuki, and H. Kawahata (2007), Radiocarbon marine reservoir ages in the western Pacific estimated by pre-bomb molluscan shells. *Nucl. Instrum. Meth. B*, *259*, 432–437.

JOURNAL OF GEOPHYSICAL RESEARCH: OCEANS, VOL. 118, 7081–7094, doi:10.1002/2013JC008983, 2013

Effects of Kuroshio intrusions on nonlinear internal waves in the South China Sea during winter

Jae-Hun Park[1] and David Farmer[2,3]

Received 28 March 2013; revised 29 November 2013; accepted 3 December 2013; published 20 December 2013.

[1] During winter the Kuroshio tends to cross Luzon Strait, penetrating the northeastern South China Sea where it forms energetic mesoscale structures. Luzon Strait is also a site where westward-propagating large-amplitude internal waves are generated. We describe observations of these waves acquired in the deep basin of the South China Sea during the winter of 2010−2011, with the goal of assessing the influence of mesoscale variability on their properties. Combining tidal current simulations with an internal wave generation and evolution model, we obtain time series of deviations between our observations and the model simulations. These deviations are analyzed in terms of mesoscale variability based on the data-assimilated HYbrid Coordinate Ocean Model (HYCOM) simulations. We find that simplified models of nonlinear internal wave response to changes in horizontal stratification gradients and vertical shear provide at best weak simulations of amplitude modulation. In contrast to these results, deviations of internal wave arrival time, occurring up to 2 h early during Kuroshio inflows, are quite well simulated when derived from integration of the first internal mode phase speed along two-dimensional ray-traced paths using HYCOM simulations of velocity and density fields together with bathymetry. Refraction of the internal waves by Kuroshio intrusions can lead to substantial distortion of the paths, sufficient to provide a potential explanation for the apparent suppression of waves during previous winter measurements. Our results suggest that the internal wave field can be a sensitive indicator of mesoscale variability in Luzon Strait and the northeastern South China Sea.

Citation: Park, J.-H., and D. Farmer (2013), Effects of Kuroshio intrusions on nonlinear internal waves in the South China Sea during winter, *J. Geophys. Res. Oceans*, *118*, 7081–7094, doi:10.1002/2013JC008983.

1. Introduction

[2] A prominent feature of remotely sensed images of the South China Sea is the westward radiation of nonlinear internal waves from Luzon Strait. When the cumulative patterns of multiple images acquired over an extended period are superimposed as in Figure 1a, the westward-propagating waves appear to radiate with few significant deviations as a fairly well-defined beam originating just west of the strait, prior to its interaction with the shoaling topography of the mainland coast. The tidally linked appearance of these waves and the way in which they are formed, evolve and subsequently interact with the shoaling topography of the mainland coast have attracted close attention and motivated numerous observations and numerical model simulations which have led to many new insights, but also raise a number of questions. One question relates to variability in the occurrence and properties of these waves over periods of weeks to months, including interannual effects. Here, we describe results of a study that addresses this aspect, with particular attention given to the role of Kuroshio intrusions in influencing internal wave propagation paths and arrival times. By Kuroshio intrusions, we refer the well-known behavior of the Kuroshio which can traverse Luzon Strait in variable ways such as looping, leaking, and leaping paths [*Nan et al*., 2011], contributing to strong currents and mesoscale variability in the northeastern South China Sea. The leaping path produces relatively small net inflow into the South China Sea with enhanced zonal gradient of thermocline depth near Luzon Strait, while the other two paths bring more Pacific waters into the South China Sea with reduced zonal gradient of thermocline depth near Luzon Strait.

[3] Most reported observations of the waves have been acquired over the spring, summer, and autumn months, during which the nonlinear waves are readily observed. However, *Ramp et al*. [2010] described an interesting 13 month data set acquired with a comprehensive line array of oceanographic moorings supporting thermistor strings. A surprising result of these observations was the almost complete

[1]Ocean Circulation and Climate Research Division, Korea Institute of Ocean Science and Technology, Ansan, South Korea.
[2]Graduate School of Oceanography, University of Rhode Island, Narragansett, Rhode Island, USA.
[3]Now at School of Earth and Ocean Sciences, University of Victoria, Victoria, British Columbia, Canada.

Corresponding author: J.-H. Park, Korean Institute of Ocean Science and Technology, 787 Haean-ro,, Sangnok-gu, Ansan 426-744, South Korea. (jhpark@kordi.re.kr)

2169-9275/13/10.1002/2013JC008983

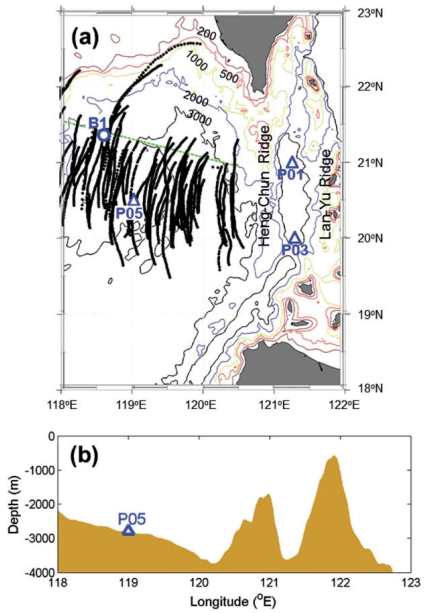

Figure 1. Locations of pressure-recording inverted echo sounders (P01, P03, and P05) and thermistor mooring B1. Solid dots indicate nonlinear internal waves acquired from MODIS satellite images between February 2003 and December 2006 (adapted from *Jackson* [2009] to show regions where the water depths are greater than 2000 m). The approximate northern boundary of the nonlinear internal waves obtained from $-0.24 \times$ longitude $+ 49.87°$ is indicated by the dashed green line. (b) Meridionally averaged topography between 20°N and 21°N.

disappearance of nonlinear internal waves at the measurement sites during the period December 2005 through early March 2006, raising the question as to the cause of this feature and whether it was unique or occurred every winter. In 2007, Zheng et al. reported results of a statistical analysis of remotely sensed images from 1995 to 2001 in which the presence of identifiable nonlinear internal waves was found to exhibit both a significant interannual and also a seasonal variation. The seasonal frequency at which waves were detected in remotely sensed images varied greatly, with a relative occurrence in June 10 times that in February. The authors explored the possible role of wind conditions in obscuring identifiable features of internal waves; corrections for such effects accounted for some, but not all of the implied internal wave variability.

[4] The present work formed part of a pilot study of the Internal Waves in Straits Experiment (IWISE) and included observations with Pressure-sensor-equipped Inverted Echo Sounders (PIES). These were deployed in Luzon Strait (P01, P03) and in the deep basin (P05) of the northeastern South China Sea (Figures 1a and 1b). Our primary focus is on the measurements at P05, which provide a clear signal of the westward-propagating waves radiating from the source region in Luzon Strait. Observations at P01 and P03 reveal three-dimensional features between the ridges and are the subject of a separate study [*Buijsman et al.*, 2013]. Station B1 is the location of the observations described by *Ramp et al.* [2010].

[5] Sections 2 and 3 provide background to the study and our observational approach, illustrating time series measurements with PIES during the winter of 2010−2011 and seasonal density structure, together with HYCOM data-assimilated simulations [*Chassignet et al.*, 2007] for the observational period of temperature and current fields in Luzon Strait and the northeastern South China Sea. In section 4, measured wave amplitude and wave arrival time at station P05 are compared with simulations based on the two-layer Hibiya-Helfrich model [*Li and Farmer*, 2011] using nominal stratification and TPXO global inverse tidal current simulations [*Egbert and Erofeeva*, 2002] (http://volkov.oce.orst.edu/tides/global.html). In section 5, the HYCOM results are used to derive fluctuations in the slope of dynamic height between P03 and P01 for comparison with our PIES measurements, in order to assess the validity of the simulations at this location. Discrepancies between the two-layer model simulations and PIES observations are explored in terms of Kuroshio penetration into the South China Sea simulated by HYCOM. It is proposed that refraction of internal waves by Kuroshio intrusions simulated using two-dimensional ray tracing can help explain some of the observed variability. The results are summarized in section 6.

2. Background

[6] Modeling and observations [e.g., *Ramp et al.*, 2004, 2010; *Chao et al.*, 2007; *Jan et al.*, 2008, 2012; *Farmer et al.*, 2009, 2011; *Buijsman et al.*, 2010a, 2010b; *Zhang et al.*, 2010; *Li and Farmer*, 2011; *Simmons et al.*, 2011; *Cai et al.*, 2012; *Vlasenko et al.*, 2012; *Wang*, 2012] have now demonstrated that internal tides are generated by tidal interaction with two ridges in Luzon Strait, Lan-Yu Ridge on the east, which includes some islands, and Heng-Chun Ridge on the west (Figure 1). Except in the north of the strait, the Lan-Yu Ridge is shallower and appears to play a dominant role in generation of internal tides, but the Heng-Chun Ridge also has an important influence, partly on account of its spacing of approximately half the horizontal wavelength of the first internal mode semidiurnal tides, thus acting as a resonator and amplifying the semidiurnal component of the westward-propagating internal tides [e.g., *Buijsman et al.*, 2010b]. Tidal forcing over these ridges is dominated by four components (O_1, K_1, M_2, and S_2) leading to a complex barotropic structure [*Jan et al.*, 2008] that in turn drives the baroclinic response. The latter leads to the prominent pattern of high-frequency nonlinear internal waves, readily identified in both remotely sensed images and in situ observations. A notable feature first identified by *Ramp et al.* [2004] is a pattern that alternates between a nonlinear wave train referred to as an *a*-wave, which occurs at the same time each day, and a single

nonlinear wave referred to as a *b*-wave occurring about 1 h later each day. The complexities of the topographic structure and the barotropic forcing have motivated many model simulations including two-dimensional, two-layer, idealized, weakly nonlinear, three-dimensional, continuous stratification, fully nonlinear, hydrostatic, and nonhydrostatic approaches.

[7] There have been few discussions on the impact of the Kuroshio on internal wave generation. *Shaw et al*. [2009], following a similar approach to *Gerkema* [2001], used a continuously stratified model to show that barotropic forcing of the stratified water along critical slopes of the Lan-Yu Ridge could launch an internal tidal beam toward the ocean surface which then interacts nonlinearly with near-surface stratification to form nonlinear internal waves trapped in the surface layer which then propagate westward across the South China Sea. They proposed that this two-step process could be inhibited during winter, first by intrusion of water from the Philippine Sea that would tend to reduce the stratification at depth, disrupting the critical slope interaction and internal tidal beam generation, and secondly through cooling and wind mixing resulting in diffusion of the near-surface stratification. This seasonal change in stratification would tend to reduce or eliminate trapped waves and bores.

[8] We lack potential density profiles available for the northeastern South China Sea (19°N−22°N, 118°E−122°E) during the period of our observations. Thus, we derived them from the World Ocean Database 2009 for summer and winter months, together with corresponding buoyancy profiles and the first three vertical displacement internal wave normal modes, as shown in Figure 2. We picked profiles reaching to 2500 m depth within the domain. The seasonal change in near-surface stratification has only a moderate impact on the linear internal tide, reducing the first internal mode long wave speed C_1 from 2.87 to 2.73 m s^{-1}; the corresponding M_2 wavelength varies from 128 km in summer to 122 km in winter. The data shown in Figure 2 provide an indication of both the variability as well as the mean stratification profile within a season. While variability in smaller-scale density structure is not captured by the mean seasonal profile and may play a role in nonlinear internal wave behavior especially in shallower water, we anticipate that the first-mode internal wave properties will be adequately described by the mean profiles in the deep basin.

[9] Strong Kuroshio intrusions into the northeastern South China Sea, which tend to occur in winter [e.g., *Shaw and Chao*, 1994; *Farris and Wimbush*, 1996], might be expected to influence internal wave generation and propagation through modification of the density and shear structures and by direct effects of advection. Penetration of the Kuroshio into the South China Sea results in a deepening of the thermocline and modifies the zonal and meridional density gradients. *Buijsman et al*. [2010b] used a two-dimensional model to determine the effects of a sloping thermocline, the double ridges, and asymmetric tides on soliton growth to the east and west of Luzon Strait, in particular explaining the much enhanced growth of the westward-propagating waves, relative to those radiated into the Pacific. *Jan et al*. [2012] further explored effects of the Kuroshio on internal tide generation with a three-dimensional model, leading to a prediction of a 20−40% enhancement of the westward-propagating M_2 internal tide when the northward flowing Kuroshio is located in the middle or along the western ridge of Luzon Strait. It was also shown that when the Kuroshio was present in Luzon Strait, the westward-propagating internal tide is 4−14% shorter and hence the phase speed is reduced by 10%. However, their study did not include the influence of Kuroshio inflows (i.e., incorporating a westward component of flow) on internal tide generation and evolution. *Jan et al*. [2012] comment that "The complicated topography and hydrography, as well as the curved rather than straight Kuroshio path in Luzon Strait, defy explanation by only a single mechanism."

[10] *Zheng et al*. [2007] used the perturbed KdV equation to investigate the influence of Kuroshio inflows on internal wave evolution. They showed that a weakly nonlinear wave of amplitude (η) propagating along a sloping thermocline would evolve as

$$\eta=\eta_0(h_0/h_1)^{3/2}, \tag{1}$$

where η_0 is the initial solitary disturbance amplitude, and h_0 and h_1 are the upper layer depths on the deep and shallow sides, respectively, of the shoaling thermocline, which they defined as the 15°C isotherm. The parameter $(h_0/h_1)^{3/2}$ is referred to as the Soliton Amplitude Growth Ratio (SAGR). Their discussion also invoked dissipation in the generation region as a potential mechanism for inhibiting initial formation of the waves. Their result would imply that a Kuroshio intrusion, which deepens the thermocline in the northeastern South China Sea and thus reduces the value of h_0/h_1, would tend to suppress internal wave growth. However, comparisons between the precise shape of the zonal stratification change and the location of internal wave measurement need to be taken into account. Although the SAGR appeared to have good predictive capability during the summer months, it did not work well in winter when the intrusions are most common. One proposed possibility was that high sea states obscured detection of the waves. Nevertheless, this issue was not explored further because they had no in situ measurements for comparison: this lack of winter observations motivated the present study. *Choi* [2006] used a fully nonlinear stratified two-layer analysis to explore the role of current shear on wave growth. He showed that the shear associated with negative horizontal vorticity in the *x*-*z* plane suppresses an internal solitary wave propagating in the positive *x* direction by inhibiting steepening of the leading interfacial slope, thus decreasing the nonlinearity. This situation is also consistent with a Kuroshio intrusion associated with a westward component of flow in the upper layer influencing westward-propagating internal waves. Thus, both the reduction of the horizontal density gradient (reduction of h_0/h_1) and also the westward component of flow in the upper layer tend to suppress growth of nonlinear internal waves. Both of these effects can be expected during a Kuroshio inflow.

[11] Effects of mesoscale variability on modulation of internal waves are examined using data-assimilated HYCOM results, which covers the global ocean with 1/12° spatial resolution. It uses a hybrid isopycnal-sigma-

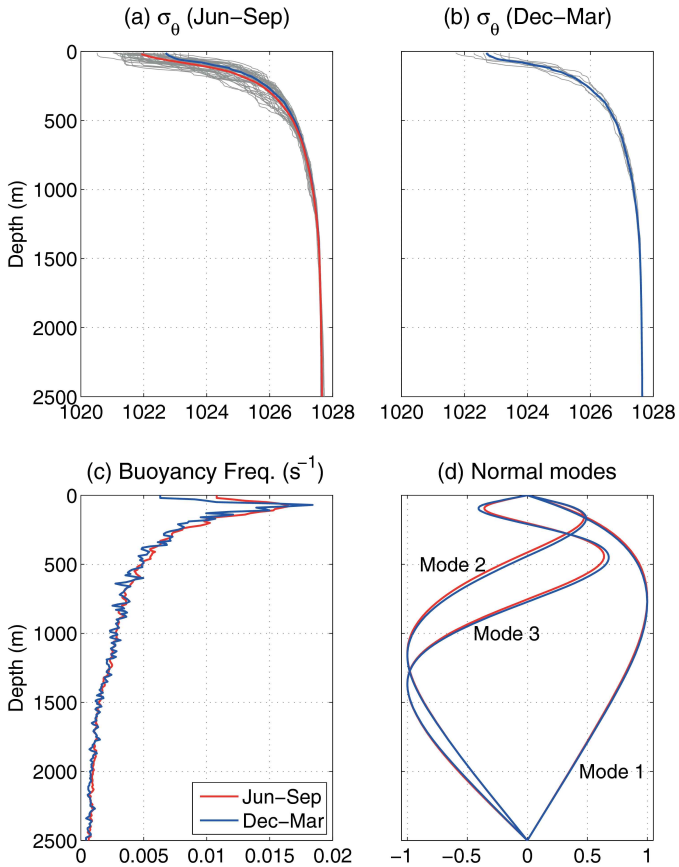

Figure 2. Potential density profiles collected for the area within 19°N–22°N, 118°E–122°E region (gray curves), and their means (red and blue curves) (a) during June to September, and (b) during December to March from World Ocean Database 2009. For comparison between the two 3 month profiles, Figure 2a also includes the blue curve which is identical to that in Figure 2b. (c) Buoyancy frequency profiles calculated from the mean profiles in Figures 2a and 2b. (d) Normal mode profiles for the first three modes calculated using Figure 2c.

pressure coordinate, but the outputs such as temperature, salinity, and velocity available to the public are at the 33 Levitus standard depths. Assimilated data include satellite-measured sea level and sea surface temperature and vertical profiles from expendable bathythermographs (XBTs), conductivity-temperature-depths (CTDs), and ARGO profiling floats [*Chassignet et al.*, 2007]. More details about the data-assimilated HYCOM are found at www.hycom.org. Figure 3 shows examples of inflows and corresponding variability in the stratification and current fields in the northeastern South China Sea and Luzon Strait from the HYCOM simulations during the 2010–2011 winter. The inflow tends to run northwest across Luzon Strait, with a narrow return current close to the Taiwanese coast. Over the middle and southern portions of Luzon Strait there is a net westward component during inflows, but there is considerable variability in the strength of the current and its shape. During strong inflows (i.e., late November to early December 2010) the warm surface water penetrates to greater depth in the Luzon Strait area.

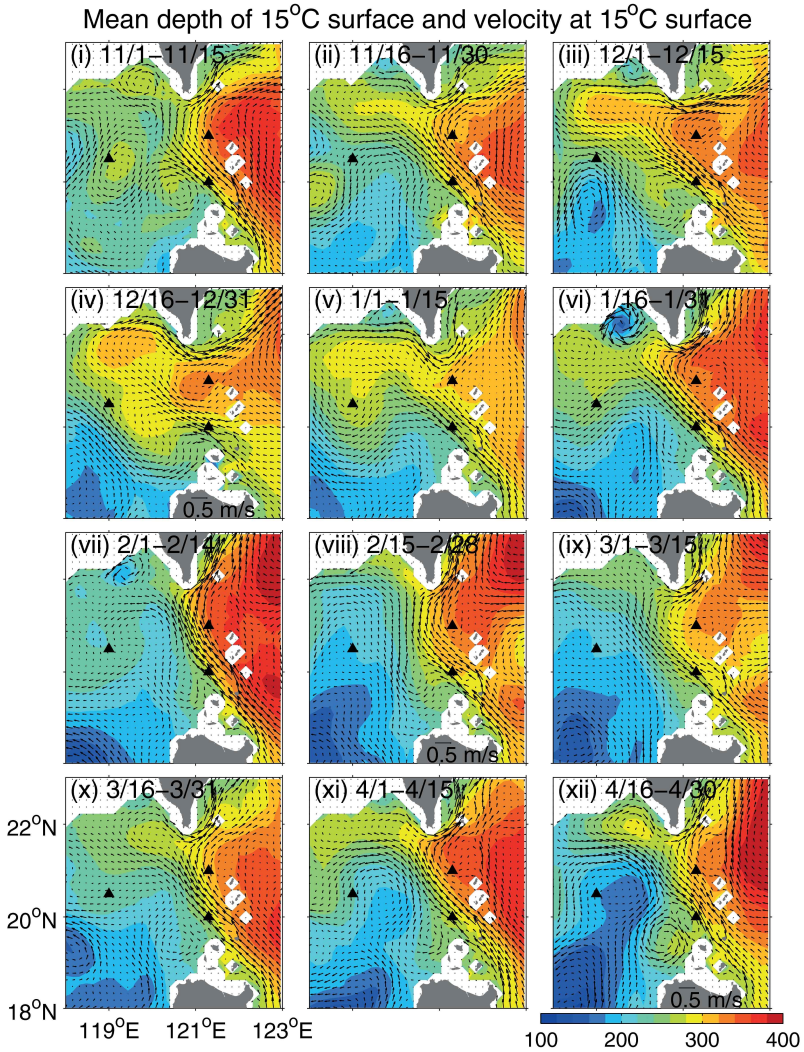

Figure 3. Half-monthly time series of mean isothermal depth of 15°C (m) and velocity fields at that depth estimated from data-assimilated HYCOM outputs. Durations are indicated in each plot. Solid triangles represent PIES sites.

3. Observations

[12] The PIES that we deployed can only acquire useful information about the first internal mode (details of instrument performance are discussed by *Li et al*. [2009]). While this restricts our analysis to first-mode behavior, the vertically integrated measurement also has the advantage of removing almost all contributions from the higher modes, leaving a clean first internal mode signal for analysis. The measurement of return acoustic travel time depends on the

sound speed profile, which depends on the corresponding profiles of temperature, salinity, and pressure. The time series of pressure measured by the instrument is used to separate the barotropic from the baroclinic contributions to the measured travel time signal. In analyzing wave-induced fluctuations, it is assumed that the background temperature and salinity profiles are perturbed by the internal waves without contributing to mixing or other changes to the background density field. Measurement of background changes in mesoscale thermal structure has been a primary motivation for development of the PIES technology [*Watts and Rossby*, 1977], for which data inversion depends on historical records of the relationship between acoustic travel time and thermal structure [e.g., *Watts et al*., 2001; *Park et al*., 2005]. For internal wave measurements, which are the focus of the present discussion, the signal of primary interest is the rapidly fluctuating component (tidal frequencies and above) induced by internal tides and nonlinear internal waves. For this purpose, *Li et al*. [2009] used mean temperature/salinity profiles from historical hydrocasts, although longer period changes due to mesoscale structure, which can impact the internal waves [*Park and Watts*, 2006], may also be observed. Inversion of the acoustic travel time data can exploit nonlinear wave models, but practical constraints favor a linear inversion [*Li et al*., 2009] and we have taken this approach here. For the thermal and acoustic characteristics of the northeastern South China Sea, a decrease of 1 ms in return acoustic travel time corresponds to a deepening of the first internal vertical displacement mode maximum of 24 m.

[13] The instruments were set to measure the return acoustic travel time and bottom pressure at 6 and 12 s intervals, respectively. The acoustic echo time records were processed into 1 min samples using the method described by *Li et al*. [2009], and filtered using the third-order Butterworth high-pass filter with a cutoff at 60 h. The effects of free surface displacement due to barotropic tides and long period surface displacements were corrected using the bottom pressure measurements. Figure 4 shows the time series of vertical displacement at P05 for the duration of the deployment, together with short segments at finer resolution illustrating the characteristic alternating pattern of *a*- and *b*-waves on the right. It is apparent from Figure 4 that nonlinear internal waves occur throughout the period of our winter observations.

4. Comparison of PIES Time Series With Model Simulations

[14] Energetic internal tides, generated by the interaction of strong tidal currents with ridges in Luzon Strait, evolve nonlinearly during their westward propagation across the South China Sea. Meaningful comparisons of the observed internal wave signal with environmental conditions such as Kuroshio intrusions require that we first allow for the complex tidal effects. For this purpose, we use as reference a much simpler two-layer model of internal wave generation and propagation implemented by *Li and Farmer* [2011], and then seek explanations for discrepancies between the model output and observations. The model combines *Hibiya*'s [1986] linear internal tide generation model with TPXO global inverse tidal current simulations in Luzon Strait, which is then matched to *Helfrich*'s [2007] fully nonlinear two-layer model. The matching procedure is as follows [*Li and Farmer*, 2011]: (1) The internal tide generated at the eastern ridge is used as input to the Helfrich's model. (2) When this wave reaches the western ridge in Helfrich's model, the internal tide generated at the western ridge also simulated by Hibiya's model is superimposed. (3) This superposed internal tide becomes a revised input to Helfrich's model with a new starting point at the western ridge. *Li and Farmer* [2011] show that the effect of the western ridge in the model cannot be ignored, though the dominant internal tide energy source is the eastern ridge. The Hibiya-Helfrich model is not a resonant calculation, but does include a superposition of the westward radiation from the western ridge on the westward radiation from the eastern ridge. A comprehensive model would be needed to resolve nonlinear effects in the resonant behavior but this is beyond the scope of the present study. The calculations using the Hibiya-Helfrich model are carried out with averaged seasonal density stratification shown in Figure 2. Comparisons using two-ridge Gaussian fits to meridionally averaged topography between 20°N and 21°N (Figure 1b) were compared with PIES observations acquired during August 2005 to October 2005 and April 2007 to October 2007 [*Li and Farmer*, 2011]. The analysis reproduced results of the measured time series, illustrating essential features of the first-mode internal tide response and its transformation into nonlinear internal waves, including the characteristic pattern of *a*- and *b*-waves.

[15] Figure 5 compares simulated with measured vertical displacements at P05 in December 2010 and February 2011. These 2 months correspond to the largest discrepancies between observed and simulated amplitude and arrival time. We track the discrepancy between the observed and simulated signal, limiting our analysis to the depth of the vertical excursion associated with the leading nonlinear internal wave and the delay in its arrival time for each tidal cycle. We are concerned with the magnitude and timing of the discrepancies between modeled TPXO forced internal waves and our observations rather than attempting to achieve a precise fit.

[16] The discrepancies between observed and modeled amplitude ($\eta_{obs} - \eta_{model} = \Delta\eta$) and between observed and modeled arrival time ($\tau_{obs} - \tau_{model} = \Delta\tau$) are shown in Figure 6a. Note that a more negative amplitude discrepancy corresponds to a thermocline deepening that *exceeds* the modeled result ($|\eta_{obs}| > |\eta_{model}|$). The full time series for both variables are shown in Figures 6b and 6c, respectively. Both the raw values and 20 day low-pass filtered results are shown. Time series of $\Delta\eta$ (Figure 6b) show two major events; weaker than simulated waves were observed from late-November to mid December and stronger than observed waves during early January and early February. Details of these events in December and February are shown in Figure 5. The *Hibiya-Helfrich* model simulates delayed arrival of nonlinear internal waves by about 2 h relative to the observations during the first half of December 2010 (Figure 6c), but somewhat irregularly trending toward a 1 h advance in April 2011. November 2010 to December 2010 is the period of strong Kuroshio intrusion into the South China Sea (see Figure 3), which is expected to influence the propagation speed of internal waves due to deepened thermocline and advection.

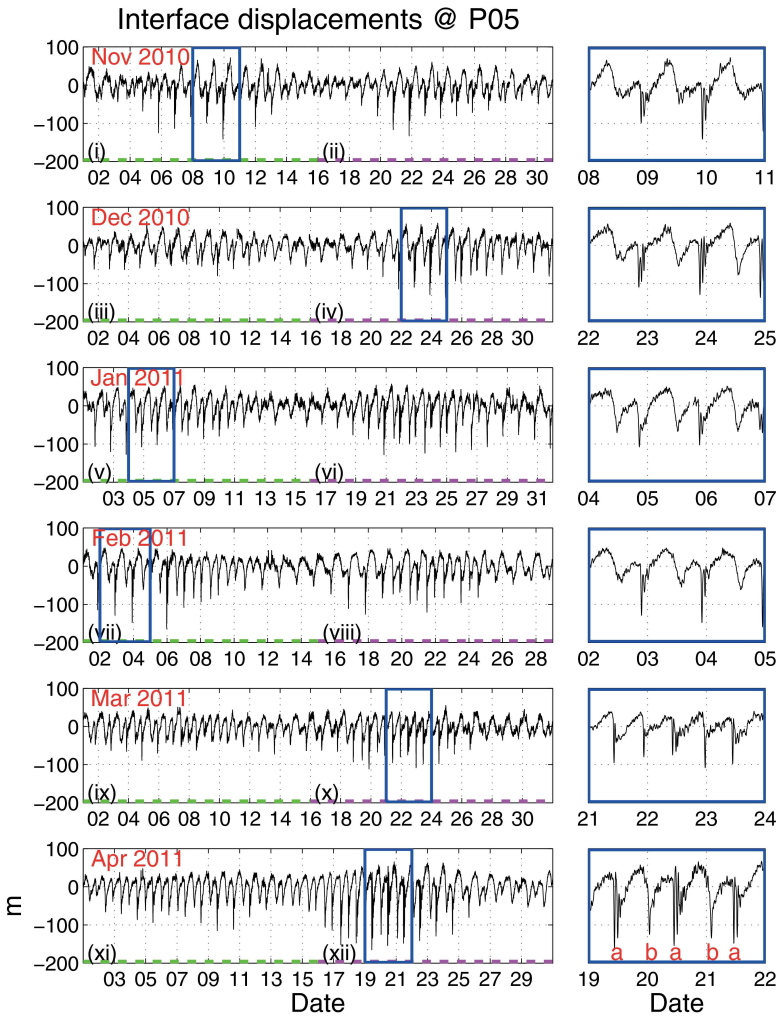

Figure 4. Time series of first-mode vertical displacements observed at P05 by PIES. (left) Time series for each month from November 2010 to April 2011, with data in blue rectangles expanded at right to illustrate *a*- and *b*-waves. Green and magenta dashes with roman numerals correspond with durations shown in Figure 3.

5. Modulation of Nonlinear Internal Waves by the Kuroshio Variation

[17] The data-assimilated HYCOM model output (Figure 3) yields a rich data set providing an opportunity to visualize the time evolving density and velocity fields associated with the Kuroshio variability in Luzon Strait. However, its validity is subject to limitations of the assimilated data and model constraints. A helpful indication of the validity of the HYCOM simulations can be achieved by comparing them with our observations at P01 and P03. Figure 7a shows fluctuations in sea surface height differences

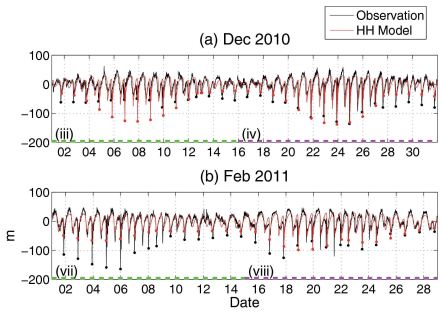

Figure 5. Time series comparisons between observations and two-layer model (*Hibiya-Helfrich*) outputs in (a) December 2010 and (b) February 2011. The model calculations of two-layer interface displacements (red) are superimposed on observations (black). Dots indicate peaks. Green and magenta dashes with roman numerals correspond with durations shown in Figure 3.

between P03 and P01 (ΔSSH) derived from our measurements (see Appendix for details), with the corresponding simulations from HYCOM. As expected, high-frequency fluctuations are weakly correlated with HYCOM since the primary data assimilated into HYCOM fields are satellite altimeter measurements with sampling intervals of ∼10 days or longer. However, the signal is moderately well correlated with longer period fluctuations and some of the higher-frequency features (i.e., a brief but sharp fluctuation in slope in early February) are shown to be consistent with the HYCOM simulations. The cross-spectral density between the two time series significantly increases for periods of 20 days and longer (Figure 7b); in what follows we use 20 days as a low-pass time scale for filtering the various results. PIES-measured ΔSSHs between P05 and P01 and P05 and P03 (not shown) reveal relatively larger differences from HYCOM-simulated ΔSSHs during November–December, but the HYCOM output converges quite closely to the PIES observations from mid January to April. P05 is in a location affected by mesoscale eddies as well as Kuroshio intrusions, which may account for some of the deviations from the PIES measurements. Note that larger amplitude of SSH differences between P03 and P01 do not always indicate a strong Kuroshio inflow into the northeastern South China Sea when the Kuroshio takes a leaping path [*Nan et al*., 2011]. For example, ΔSSH during mid January to mid February show larger amplitude of negative values than those during mid November to mid December, but velocity fields in Figure 3 show weaker Kuroshio intrusion during mid January to mid February even though the Kuroshio itself was stronger as a result of the Kuroshio path turning to the north near the Luzon Strait after passing between P03 and P01.

[18] Internal waves propagating into the northeastern South China Sea from Luzon Strait encounter a progressively shallower thermocline. During Kuroshio intrusions this thermocline structure will be modified as the surface layer deepens within the area of intrusion. The SAGR derived by *Zheng et al*. [2007] is calculated using h_0 and h_1 produced by averaging 15°C isothermal depths within the regions bounded by 20°N−21°N, 122.5°E−124°E, and 20°N−21°N, 119°E−121°E, respectively, from HYCOM outputs. These areas are determined so as to avoid the effect of submesoscale fluctuations on h_0 and h_1 estimations and to retain comparable sizes for each region.

[19] SAGR is dimensionless and in Figure 8a is therefore scaled to $\Delta\eta$ with a change in sign for consistency. The time series reveals fluctuations of 2−3 month period with a weaker signal at higher frequency. The primary fluctuation in SAGR is shown to be related to the varying dynamic slope (ΔSSH) associated with the Kuroshio in Luzon Strait (Figure 7a). Cross correlation of the SAGR with ΔSSH after running 20 day low-pass filtering yields a correlation coefficient of −0.24 with a 95% confidence limit of −0.10. Overall the SAGR decreases when the dynamic slope becomes weak and vice versa, which is expected since the dynamic slope indicates the strength of the Kuroshio in Luzon Strait and a stronger Kuroshio will increase the

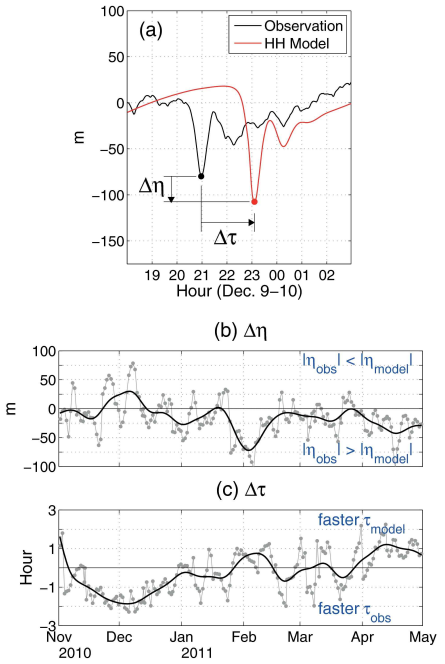

Figure 6. (a) Definition of discrepancies between observed and modeled wave arrival time ($\tau_{obs}-\tau_{model}=\Delta\tau$) and wave amplitude ($\eta_{obs}-\eta_{model}=\Delta\eta$) at P05. Time series of (b) $\Delta\eta$ and (c) $\Delta\tau$. Gray lines and dots indicate raw values and black curves superimposed on them indicate their 20 day low-pass filtered results.

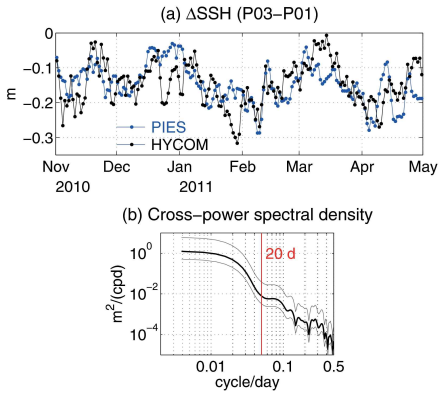

Figure 7. Time series of sea surface height difference (ΔSSH) between P03 and P01. Black lines and dots indicate ΔSSH from HYCOM model outputs and blue lines and dots from PIES measurements. (b) Cross-power spectral density from the two ΔSSH time series (black curve). Gray curves indicate 95%-confidence intervals, and vertical red line 20 day period.

thermocline depth difference and hence the SAGR. Cross correlation of the SAGR with $\Delta\eta$ after running 20 day low-pass filtering yields a correlation coefficient of −0.47 with 95% confidence limit of −0.33.

[20] Vertical current shear associated with the Kuroshio inflows will also influence nonlinear internal wave evolution [*Choi*, 2006]. This effect may be intermittent, but will be particularly significant when the Kuroshio intrudes into the South China Sea, whereas the thermocline slope is a relatively permanent feature of Luzon Strait even without intrusion of the Kuroshio. For this study, the mean current shear is calculated across a 200 m depth interval from 100 m above to 100 m below the 15°C isotherm, for each HYCOM output grid location. The resulting shears were then averaged across the area 20°N−21°N, 119°E−121°E. Figure 8b shows time series of HYCOM-simulated current shear with its sign changed. Comparison of the HYCOM-simulated current shear with $\Delta\eta$ also reveals a modest correlation, but more so during the first half of our measurements. During the period of weak internal wave amplitudes from late-November to mid December (see Figure 5a), a consistent event of strong mean current shear caused by the Kuroshio intrusion occurs. Cross correlation of the mean current shear with $\Delta\eta$ after 20 day low-pass filtering yields a correlation coefficient of −0.39 with 95% confidence limit of −0.25.

[21] Internal tide generation and evolution can be influenced by the Kuroshio intrusion near the generation region, which results in asymmetry of the tidal forcing. *Buijsman et al*. [2010a] and *Li and Farmer* [2011] showed that steady background barotropic flow superimposed on tidal current increases (decreases) the amplitude of internal tides propagating against (with) the flow due to the Doppler effect during internal tide generation. Thus, the Doppler effect during a Kuroshio inflow might be expected to reduce the corresponding internal tide amplitude. Stratification changes also can modulate the internal tide generation, which is greatest when the bottom slope matches the wave characteristics, a function of the buoyancy frequency (N) [i.e., *Baines*, 1982]. Figures 8c and 8d show time series of the HYCOM-simulated zonal component of background flow and the buoyancy frequency N near the internal tide generation region (20.35°N−20.65°N, 121.9°E−122.1°E), revealing significant higher frequency variability, with characteristics similar to the current shear. However, comparison of these two variables with $\Delta\eta$ reveals almost no meaningful correlations (0.15 and 0.0), suggesting that the SAGR and current shear play more efficient roles in modulating the internal tidal amplitude, although much longer time series would be required to make a compelling case.

[22] Strong currents associated with Kuroshio inflows can also be expected to modify the arrival time of waves at the measurement location. Changes in both the current and

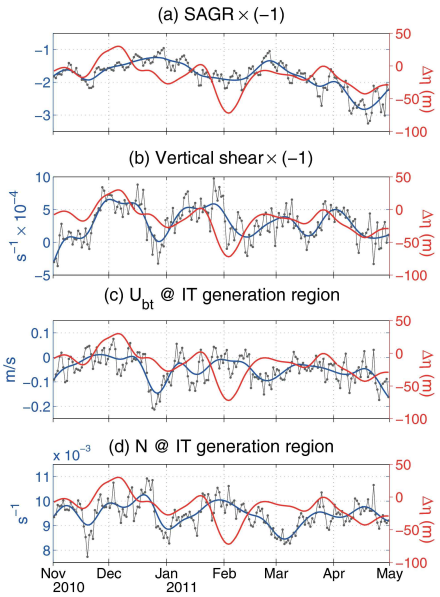

Figure 8. Time series of (a) Soliton Amplitude Growth Ratio (SAGR), and (b) mean vertical shear between 119°E and 121°E with signs changed for comparison with $\Delta\eta$, and time series of (c) east-westward barotropic current (U_{bt}), and (d) buoyancy frequency (N) between 200 and 300 m near the internal tide generation region (20.35°N–20.65°N, 121.9°E–122.1°E). Gray lines and dots indicate daily values calculated using HYCOM outputs, and blue curve indicates their 20 day low-pass filtered values. Red curve represents 20 day low-pass filtered $\Delta\tau$ shown in Figure 6b.

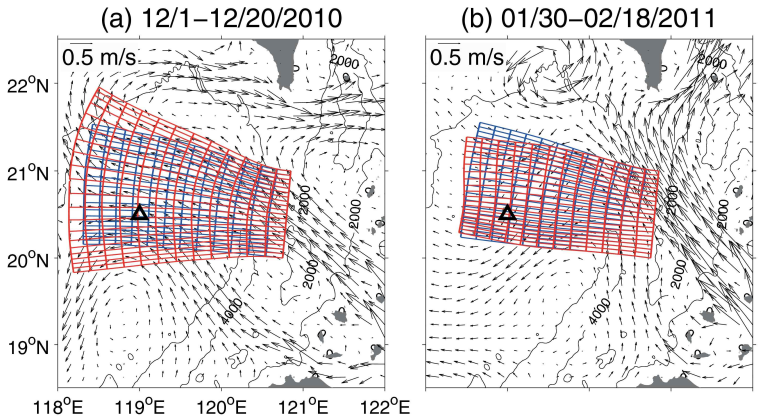

Figure 9. Ray-tracing results superimposed on mean velocity fields at 100 m during (a) 1–20 December 2010, and (b) 30 January 2011to 18 February 2011. Blue and red lines are simulations of wave front propagation, excluding and including currents, in a simple two-dimensional wave propagation model. Wave fronts are drawn every 2 h. Black triangles indicate P05.

density fields will play a role in wave refraction due to the resulting changes in spatial gradient of the phase speed, and modification of the raypath implies bathymetric changes along the path. A simplified approach to this can be taken with a linear two-dimensional ray-tracing method, essentially an application of Snell's law [e.g., *Sherwin et al*., 2002; *Park and Watts*, 2006], where we incorporate derivations of the stratification, velocity profiles and bathymetry from HYCOM in a calculation of wave front propagation, starting from the western ridge in Luzon Strait. In this simple two-dimensional ray-tracing model the ray advances by geometric optics in a direction normal to the wave front by a distance

$$\Delta d = \Delta t \sqrt{C_{u1}^2 + C_{v1}^2} \cos\varphi, \tag{2}$$

where C_{u1} and C_{v1} are the eastward and northward linear phase speeds, respectively, of the first-mode M_2 internal tide propagating through a velocity field $\boldsymbol{U}(z)$, Δt is a time step set to 10 min and φ is the angle between the direction of C_1, (C_{u1}, C_{v1}), and ray propagation direction. The first-mode phase speeds (C_{u1}, C_{v1}) are computed by solving the *Taylor-Goldstein* equation [see *Smyth et al*., 2011], including continuous profiles of stratification $N(z)$ and total velocity $\boldsymbol{U}(z)$ derived from HYCOM outputs as follows [*Phillips*, 1977]:

$$W(z)_{zz} - \frac{U(z)_{zz}}{\boldsymbol{U}(z) - C} W(z) + \frac{N(z)^2}{(\boldsymbol{U}(z) - C)^2} W(z) = 0, \tag{3}$$

where $W(z)$ is vertical velocity and C is the phase speed of eigenmodes. Equation (3) is solved for zonal and meridional directions separately at each grid point. Note that the *Taylor-Goldstein* equation considers a long internal wave without rotation. *Alford et al*. [2010] showed that the M_2 semidiurnal internal tide propagates in the South China Sea at a phase speed 1.07 times greater than that of a long internal wave, and this phase speed modification is used for the ray-tracing computations. Thus, the wave front propagation is simulated using

$$\Delta d = 1.07 \Delta t \sqrt{C_{u1}^2 + C_{v1}^2} \cos\varphi, \tag{4}$$

[23] The advancing wave front in the ray-tracing simulation is spline smoothed at each step so as to reduce numerically induced noise. The initial wave front was assumed to be a straight line of length 110 km located west of the Heng-Chun Ridge, and its angle set to ~5° clockwise from the north in consideration of the wave front locations and their main propagation direction observed in satellite images (see Figure 1).

[24] Ray tracing is shown for two segments of our observed time series in Figure 9. For this purpose, we use HYCOM-simulated stratification and current vector profiles for 11−20 December 2010, and 30 January to 18 February 2011 (red curves in Figure 9). These contrasting examples illustrate first a strong dispersion of the raypaths during the December inflow followed by only a slight distortion of the paths during the period without inflow in early February. The Kuroshio intrusion in December also raises the phase speed of internal waves leading to a more rapid advance of the wave fronts. The impact of currents on ray tracing was examined with HYCOM simulations of stratification, but without including current profiles. These are shown as blue curves in Figure 9. The dispersion of the raypaths during the December inflow decreases significantly when currents are not included (Figure 9a) in the ray tracing, while the contribution of currents to raypath deviations is relatively weak in February (Figure 9b). When current profiles are

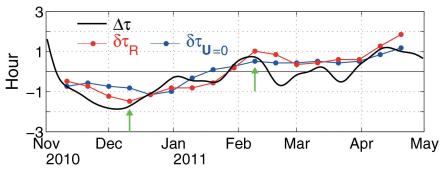

Figure 10. Time series of 20 day low-pass filtered $\Delta\tau$ (black curve) and wave arrival time anomalies ($\delta\tau_R$) computed using a simple wave propagation ray-tracing model (red lines) and $\delta\tau_{U=0}$ (blue lines) is the corresponding wave arrival time with the background velocity field set to zero. The ray-tracing simulations are conducted using the first-mode internal wave phase speeds calculated from 20 day mean velocity and stratification fields of HYCOM outputs with a 10 day overlap. Green arrows indicate the times for Figures 9a and 9b.

excluded from the calculation the advance of the wave fronts is also delayed about 1 h at P05 in December, but very little in February.

[25] Since the ray-tracing model assumes that the energy and frequency of the waves are conserved, spreading out or focusing of rays will be associated with a decrease or increase of internal wave energy. We carried out ray-tracing simulation for the full period of our observations (November 2010 to April 2011) to evaluate the simulated discrepancy in wave amplitude $\Delta\eta(t)$ due to this effect. Time series of the separation between neighboring rays at P05, representing changes of internal wave energy E, vary about 10% relative to their initial separation just west of the western ridge. This implies that divergence of the waves only accounts for about 5% of the internal wave amplitude change $\left(i.e., \cong \left[1-\sqrt{0.9E}\right]\times 100\right)$, suggesting that the impact of advective refraction on the observed internal wave amplitude modulation is modest.

[26] Ray tracing for the full period of our observations was also used to evaluate the simulated discrepancy in wave arrival times. For this purpose, we generate a time series of wave front arrival times at P05 from raypath calculations of equation (4) using C_1 obtained from successive 20 day mean HYCOM stratification and velocity fields with a 10 day overlap. For comparison, an additional time series of wave front arrival times at P05 is also calculated. The raypath calculations reveal that the wave front takes 17.31 h on average with the velocity field *included* and 17.98 h with the velocity field *excluded*, for the waves to travel to P05 from the selected origin near the western ridge. This delay is subtracted from the ray-trace travel time to generate a raypath time series $\delta\tau_R(t)$ and $\delta\tau_{U=0}(t)$, for comparison with the time series of travel time difference between the observed and the *Hibiya-Helfrich* modeled arrival times $\Delta\tau(t)$. We then compare $\delta\tau_R(t)$, $\delta\tau_{U=0}(t)$, and $\Delta\tau(t)$ in Figure 10. The raypath calculations of $\delta\tau_R(t)$ simulate early arrivals from mid November to mid January switching to late arrivals thereafter, consistent both in magnitude and overall shape with the $\Delta\tau(t)$ time series. Cross correlation of $\delta\tau_R(t)$ with $\Delta\tau(t)$ after 10 day subsampling yields a correlation coefficient of 0.86 with a 95% confidence limit of 0.66. Notwithstanding the simplicity of the ray-tracing approach and limitations of the HYCOM outputs, variability in arrival time delay relative to the two-layer *Hibiya-Helfrich* model simulation with straight line propagation, fixed uniform stratification, and absence of background current field, is quite well explained. The raypath calculations of $\delta\tau_{U=0}(t)$ also simulate early-to-late arrival changes during the 6 month period, but their magnitudes decrease compared to those of $\delta\tau_R(t)$ with a root-mean-squared difference of 0.39 h. Cross correlation of $\delta\tau_{U=0}(t)$ with $\Delta\tau(t)$ after 10 day subsampling yields a correlation coefficient of 0.82 with a 95% confidence limit of 0.55. It is shown that the vector current profiles and stratification simulated by HYCOM when averaged over 20 days provide an adequate representation of conditions for this purpose and our results demonstrate that mesoscale circulation in the northeastern South China Sea can be a substantial factor influencing the internal wave field. While nonlinear models have proven effective at describing nonlinear evolution of the internal tide, for the 20 day resolution used in our analysis, linear ray tracing succeeds in predicting the travel time variability and demonstrates the dominant influence mesoscale structures can have on propagation across the deep basin of the South China Sea.

[27] Finally, in Figure 11 we evaluate the wave front refraction for the period December 2005 to Feburary 2006, during which *Ramp et al*. [2010] found what appeared to be almost complete suppression of internal waves. We used HYCOM outputs for the corresponding period and found it characterized by an almost continuous strong Kuroshio inflow. Ray tracing for the 3 month average conditions (Figure 11) shows that internal waves are strongly refracted. Although there exists a variability in the lateral boundary of the nonlinear internal waves in Figure 1a, we approximate their northern boundary by the dashed green line in Figure 1a ($-0.24 \times$ longitude $+ 49.87°$) based on

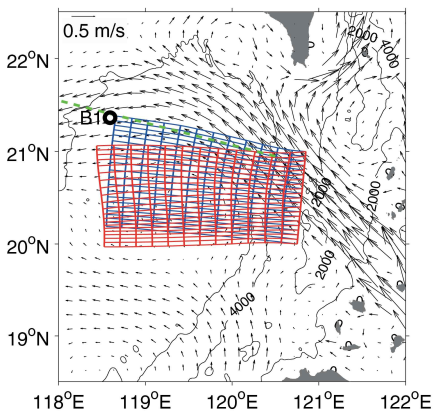

Figure 11. Same as Figure 9 for the period December 2005 to February 2006, corresponding to measurements at station B1 in *Ramp et al*. [2010]. The dashed green line is the same to that in Figure 1a.

the remotely sensed wave structures. Figure 11 implies that the northern observable boundary of ray-traced internal wave fronts would be displaced southward by ~35 km due to current and stratification conditions simulated by HYCOM. Only the northern part of the wave front encounters the intruding Kuroshio, but this is sufficient to move the waves away from station B1. These results suggest site B1 is particularly sensitive to such mesoscale effects due to its proximity to the northern boundary of nonlinear internal waves radiated westward from Luzon Strait (Figure 1a).

6. Conclusions

[28] Observations of internal waves in the South China Sea during the winter of 2010–2011 show that internal tides with strongly nonlinear features are radiated westward into the South China Sea throughout the winter, including periods of Kuroshio inflow. The winter persistence of nonlinear internal waves lends support to the view that wind conditions tend to obscure the remotely sensed signature of the waves at this time and may be the primary cause of reduced detection frequency by remote sensing in that season. We used seasonally averaged density structure and global inverse tidal current simulations with an internal tide generation and nonlinear wave propagation model as a reference against which to explore effects of the intruding Kuroshio. Deviations between modeled and observed wave amplitudes and wave arrival times form the essential time series. The time-dependent three-dimensional properties of the Kuroshio during our observations were derived from data-assimilated HYCOM simulations. The validity of HYCOM simulations in this area was evaluated by comparing derived sea surface slope fluctuations in Luzon Strait with our observations. The resulting comparison demonstrated consistency of HYCOM simulations with our Luzon Strait observations for periods of 20 days and longer.

[29] Penetration of the Kuroshio is accompanied by a deepening of the thermocline and strongly sheared currents. For a thermocline, that is, shallow relative to total water depth, thermocline deepening tends to inhibit development of nonlinear internal waves. On the other hand a shoaling of the thermocline can lead to wave amplification [*Zheng et al*., 2007]. A nonlinear wave propagating in a vertically sheared flow with negative vorticity (i.e., stronger surface flow relative to deeper water, in the positive x direction of wave propagation) is also subject to reduced nonlinearity and amplitude [*Choi*, 2006]. The time series of the deviation between modeled and observed wave amplitude were compared with *Zheng et al*.'s [2007] dimensionless Soliton Amplitude Growth Ratio (SAGR) and also with the vertical shear. The SAGR and vertical shear were derived from HYCOM simulations and scaled to our observations. The SAGR provides weak support for this predictor with our data. Other effects, especially variability in the efficiency of barotropic to baroclinic conversion in Luzon Strait and the consequences of oblique flow across the strait could mask any straightforward effect of the thermocline slope. The vertical shear simulations from HYCOM are shown to be somewhat less closely related to the amplitude discrepancy time series. A robust prediction of nonlinear internal wave amplitudes in winter may therefore require a more comprehensive, possibly three-dimensional model that accommodates the velocity and density fields imposed by Kuroshio intrusion.

[30] The wave arrival time is also influenced by the evolving velocity and density field. Variability of this time series was calculated through ray tracing of wave fronts, from Heng-Chun Ridge to the measurement site, using known topography and vertical profiles of the HYCOM-simulated current vector and density. The direction and advance of the wave front at each step along a given ray were sequentially evaluated as local solutions of the *Taylor-Goldstein* equation. The results lead to quite good agreement with deviations in the observed arrival times. The waves arrived early during the strong westward inflow in December and later during March when there was virtually no inflow; the total variation in arrival time spanned about 3 h consistent with deviations from our Hibiya-Helfrich model results with horizontally homogeneous stratification and no imposed inflows. Refraction of the waves by the inflow is independent of their generation process, which explains this apparent predictive success of the wave arrival time. This in turn implies that the time of internal wave generation is affected very little by the process modulating the wave amplitudes, which would allow us to model the wave arrival time reasonably well despite being unable to provide a robust prediction of their amplitudes.

[31] We emphasize that variability of internal wave propagation due to refraction by mesoscale structures dominated the arrival time and allowed a simple linear ray-tracing calculation with HYCOM input to reproduce the quite large changes we measured. During our PIES measurements, temporal changes in advection account for ~5% of the overall raypath dispersion; temporal changes in stratification also have a comparable effect of ~5%; the corresponding effect due to bathymetric changes necessarily implies modification of density and velocity profiles to adjust for the changing depth in some way that cannot be unambiguously defined. However, actual bathymetric changes for the examples shown here are relatively small, the most extreme effect of bathymetric changes being the most northerly paths in Figure 9a, where the depth reduction from blue to red ray-trace paths is ~500 m at the western end of the paths; this reduction in depth spans less than 50% of the total path length. Normal mode calculation using historical hydrocast data implies an approximately 3% decrease in first-mode internal wave phase speed for a 500 m decrease in depth. The effect of bathymetric change in arrival time for this extreme case would then be about 1.5%. We conclude that for these examples, bathymetric effects on the changes in ray-trace paths are significantly less than those caused by velocity and stratification changes.

[32] Refraction of the waves by the mesoscale structures not only changes their arrival time at a specific measurement location, but also results in a deviation from the characteristic westward propagation path seen in the cumulative remote sensing images documented by *Jackson* [2009]. Given the finite width of this horizontal beam of internal waves, measurements acquired near its northern or southern boundaries will be sensitive to the extent of refraction. This mechanism can provide a potential explanation of the disappearance of internal waves described by

Ramp et al. [2010] during the winter of 2005–2006 when there was a strong and persistent Kuroshio inflow. Tracing internal wave propagation for the velocity and density field simulated by HYCOM for the same period implies that the northern boundary of the internal wave path would have been shifted approximately ∼35 km south of its unperturbed path. While the precise location of the boundary is unknown and may not be sharply defined, such a shift could have moved the observable waves south of station B1 (see Figure 11), leading to the apparent suppression of waves at that location.

[33] While our results demonstrate the important role of advective refraction by mesoscale structures, more refined modeling and further measurements are required to explain the observed modulation of internal wave amplitude. First-mode internal wave properties are quite easily detected using instruments deployed on the sea floor, with the potential for providing a sensitive indicator of mesoscale variability in the South China Sea.

Appendix A: Estimation of ΔSSH From PIES Measurements

[34] The sea surface height is composed of steric (baroclinic) and mass-loading (barotropic) components, and PIES measures both components simultaneously from acoustic travel time and bottom pressure [see *Park et al*., 2012]. For the estimation of steric component from our data, a linear relationship between the dynamic height referred to 1200 dbar (ϕ_{1200}) and acoustic travel time between 1200 dbar and the surface is estimated using 387 historical hydrocasts in 19°N−22°N, 118°E−124°E, obtained from the database of Met Office Hadley Center (http://www.metoffice.gov.uk/hadobs/en3/) [*Ingleby and Huddleston*, 2007]. The reference depth of 1200 dbar is determined to include as many data as possible to reduce errors, without missing the main vertical structure. Then, the difference of mean-removed acoustic travel time between P03 and P01 is converted to the difference of ϕ_{1200} ($\Delta\phi_{1200}$) using the estimated linear relationship. Finally, PIES-estimated ΔSSH including both steric and mass-loading components is obtained by $\Delta\phi_{1200}/g + \Delta P'/\rho_d g$, where g is gravity (9.8 m s^{-2}), ρ_d typical deep density (1036 kg m^{-3}), and $\Delta P'$ difference of mean-removed 48 h low-pass filtered bottom pressure between P03 and P01. For the comparison, the 6 month mean ΔSSH calculated from HYCOM outputs are added to PIES-estimated ΔSSH.

[35] **Acknowledgments.** We would like to acknowledge the support and assistance, in deployment and recovery of instruments, by Matthew Alford and his group, Yiing Jang Yang, and the captain and crews aboard R/V OR-3. Erran Sousa, Daniel Holloway, Maureen Kennelly, and D. Randolph Watts provided invaluable assistance with PIES preparation, deployment, recovery, and PIES data processing. Qiang Li kindly shared Hibiya-Helfrich's model outputs. We gratefully acknowledge the several thoughtful comments of our referees. This work was supported by the ONR IWISE program contract N000140910220. J.-H. Park is also supported by KIOST in-house grants (PE98973, PE99162) and by "Development of Technology for CO_2 Marine Geological Storage" project funded by Ministry of Oceans and Fisheries, Republic of Korea.

References

Alford, M. H., R. C. Lien, H. L. Simmons, J. Klymak, S. Ramp, Y. J. Yang, D. Tang, and M. H. Chang (2010), Speed and evolution of nonlinear internal waves transiting the South China Sea, *J. Phys. Oceanogr.*, *40*, 1338–1355.

Baines, P. G. (1982), On internal tide generation models, *Deep Sea Res., Part A*, *29*, 307–338.

Buijsman, M. C., Y. Kanarska, and J. C. McWilliams (2010a), On the generation and evolution of nonlinear internal waves in the South China Sea, *J. Geophys. Res.*, *115*, C02012, doi:10.1029/2009JC005275.

Buijsman, M. C., J. Klymak, S. Legg, M. H. Alford, D. Farmer, J. A. MacKinnon, J. Nash, J.-H. Park, A. Pickering, and H. Simmons (2013), Three dimensional double ridge internal tide resonance in Luzon Strait, *J. Phys. Oceanogr.*, in press.

Buijsman, M. C., J. C. McWilliams, and C. R. Jackson (2010b), East-west asymmetry in nonlinear internal waves from Luzon Strait, *J. Geophys. Res.*, *115*, C10057, doi:10.1029/2009JC006004.

Cai, S., J. Xie, and J. He (2012), An overview of internal solitary waves in the South China Sea, *Surv. Geophys.*, *33*, 927–943, doi:10.1007/s10712-012-9176-0.

Chao, S.-Y., D.-S. Ko, R.-C. Lien, and P.-T. Shaw (2007), Assessing the west ridge of Luzon Strait as an internal wave mediator, *J. Oceanogr.*, *63*, 897–911.

Chassignet, E. P., H. E. Hurlburt, O. Martin Smedstad, G. R. Halliwell, P. J. Hogan, A. J. Wallcraft, R. Baraille, and R. Bleck (2007), The HYCOM (HYbrid Coordinate Ocean Model) data assimilative system, *J. Mar. Syst.*, *65*, 60–83.

Choi, W. (2006), The effect of a background shear current on large amplitude internal solitary waves, *Phys. Fluids*, *18*, 036601, doi:10.1063/1.2180291.

Egbert, G. D., and S. Y. Erofeeva (2002), Efficient inverse modeling of barotropic ocean tides, *J. Atmos. Oceanic Technol.*, *19*, 183–204.

Farmer, D., Q. Li, and J.-H. Park (2009), Internal wave observations in the South China Sea: The role of rotation and non-linearity, *Atmos. Ocean*, *47*, 267–280.

Farmer, D. M., M. H. Alford, R.-C. Lien, Y. J. Yang, M.-H. Chang, and Q. Li (2011), From Luzon Strait to Dongsha Plateau: Stages in the life of an internal wave, *Oceanography*, *24*, 64–77, doi:10.5670/oceanog.2011.95.

Farris, A., and M. Wimbush (1996), Wind-induced Kuroshio intrusion into the South China Sea, *J. Oceanogr.*, *52*, 771–784.

Gerkema, T. (2001), Internal and interfacial tides: Beam scattering and local generation of solitary waves, *J. Mar. Res.*, *59*, 227–255, doi:10.1357/002224001762882646.

Helfrich, K. R. (2007), Decay and return of internal solitary waves with rotation, *Phys. Fluids*, *19*, 026601, doi:10.1063/1.2472509.

Hibiya, T. (1986), Generation mechanism of internal waves by tidal flow over a sill, *J. Geophys. Res.*, *91*, 7697–7708.

Ingleby, B., and M. Huddleston (2007), Quality control of ocean temperature and salinity profiles—historical and real-time data, *J. Mar. Syst.*, *65*, 158–175, doi:10.1016/j.jmarsys.2005.11.019.

Jackson, C. R. (2009), An empirical model for estimating the geographic location of nonlinear internal solitary waves, *J. Atmos. Oceanic Technol.*, *26*, 2243–2255, doi:10.1175/2009JTECHO638.1.

Jan, S., R.-C. Lien, and C.-H. Ting (2008), Numerical study of baroclinic tides in Luzon Strait, *J. Oceanogr.*, *64*, 789–802, doi:10.1007/s10872-008-0066-5.

Jan, S., C.-S. Chern, J. Wang, and M.-D. Chiou (2012), Generation and propagation of baroclinic tides modified by them Kuroshio in the Luzon Strait, *J. Geophys. Res.*, *117*, C02019, doi:10.1029/2011JC007229.

Li, Q., and D. M. Farmer (2011), The generation and evolution of nonlinear internal waves in the deep basin of the South China Sea, *J. Phys. Oceanogr.*, *41*, 1345–1363.

Li, Q., D. M. Farmer, T. F. Duda, and S. Ramp (2009), Acoustical measurement of nonlinear internal waves using the inverted echo sounder, *J. Atmos. Oceanic Technol.*, *26*, 2228–2242.

Nan, F., H. Xue, F. Chai, L. Shi, M. Shi, and P. Guo (2011), Identification of different types of Kuroshio intrusion into the South China Sea, *Ocean Dyn.*, *61*, 1291–1304, doi:10.1007/s10236-011-0426-3.

Park, J.-H., and D. R. Watts (2006), Internal tides in the southwestern Japan/East Sea, *J. Phys. Oceanogr.*, *36*, 22–34.

Park, J.-H., D. R. Watts, K. L. Tracey, and D. A. Mitchell (2005), A multi-index GEM technique and its application to the southwestern Japan/East Sea, *J. Atmos. Oceanic Technol.*, *22*, 1282–1293.

Park, J.-H., D. R. Watts, K. A. Donohue, and K. L. Tracey (2012), Sea surface height variability observed by pressure-recording inverted echo sounders and satellite altimetry in the Kuroshio Extension, *J. Oceanogr.*, *68*, 401–416, doi:10.1007/s10872-012-0108-x.

Phillips, O. M. (1977), *The Dynamics of the Upper Ocean*, 2nd ed., 336 pp., Cambridge Univ. Press, London.

Ramp, S. R., T.-Y. Tang, T. F. Duda, J. F. Lynch, A. K. Liu, C.-S. Chiu, F. L. Bahr, H.-R. Kim, and Y. J. Yang (2004), Internal solitons in the northeastern South China Sea. Part I: Sources and deep water propagation, *IEEE J. Oceanic Eng.*, *29*, 1157–1181.

Ramp, S. R., Y. J. Yang, and F. L. Bahr (2010), Characterizing the nonlinear internal wave climate in the northeastern South China Sea, *Nonlinear Processes Geophys.*, *17*, 481–498, doi:10.5194/npg-17–481-2010.

Shaw, P. T., and S. Y. Chao (1994), Surface circulation in the South China Sea, *Deep Sea Res., Part I*, *40*, 1663–1683.

Shaw, P.-T., D. S. Ko, and S.-Y. Chao (2009), Internal solitary waves induced by flow over a ridge: With applications to the northern South China Sea, *J. Geophys. Res.*, *114*, C02019, doi:10.1029/2008JC005007.

Sherwin, T. J., V. I. Vlasenko, N. Stashchuk, D. R. Gus Jeans, and B. Jones (2002), Along-slope generation as an explanation for some unusually large internal tides, *Deep Sea Res., Part I*, *49*, 1787–1799.

Simmons, H., M.-H. Chang, Y.-T. Chang, S.-Y. Chao, O. Fringer, C. R. Jackson, and D. S. Ko (2011), Modeling and prediction of internal waves in the South China Sea, *Oceanography*, *24*, 88–99, doi:10.5670/oceanog.2011.97.

Smyth, W. D., J. N. Moum, and J. D. Nash, (2011), Narrowband, high-frequency oscillations at the equator. Part II: Properties of shear instabilities, *J. Phys. Oceanogr.*, *41*, 397–411, doi:10.1175/2010JPO4450.1.

Vlasenko, V., C. Guo, and N. Stashchuk (2012), On the mechanism of A-type and B-type internal solitary wave generation in the northern South China Sea, *Deep Sea Res., Part I*, *69*, 100–112, doi:10.1016/j.dsr.2012.07.004.

Wang, D.-P. (2012), Diurnal modulation of semidiurnal internal tides in Luzon Strait, *Ocean Modell.*, *59–60*, 1–10, doi:10.1016/j.ocemod.2012.09.005.

Watts, D. R., and H. T. Rossby (1977), Measuring dynamic heights with inverted echo sounders: Results from MODE, *J. Phys. Oceanogr.*, *7*, 345–358.

Watts, D. R., C. Sun, and S. Rintoul (2001), A two-dimensional gravest empirical mode determined from hydrographic observations in the Subantarctic Front, *J. Phys. Oceanogr.*, *31*, 2186–2209.

Zhang, Z., O. B. Fringer, and S. R. Ramp (2011), Three-dimensional, nonhydrostatic numerical simulation of nonlinear internal wave generation and propagation in the South China Sea, *J. Geophys. Res.*, *116*, C05022, doi:10.1029/2010JC006424.

Zheng, Q., R. D. Susanto, C.-R. Ho, Y. T. Song, and Q. Xu (2007), Statistical and dynamical analyses of generation mechanisms of solitary internal waves in the northern South China Sea, *J. Geophys. Res.*, *112*, C03021, doi:10.1029/2006JC003551.